Analysis of molecular diffusion and photochemistry by quantitative fluorescence correlation spectroscopy

Inaugural dissertation

for the attainment of the title of doctor
in the Faculty of Mathematics and Natural Sciences
at the Heinrich Heine University Düsseldorf

presented by

Deborah Sandrin

from Pordenone, Italy

Düsseldorf, April 2017

from the institute for Physical Chemistry II
at the Heinrich Heine University Düsseldorf

Published by permission of the
Faculty of Mathematics and Natural Sciences at
Heinrich Heine University Düsseldorf

Supervisor: Prof. Dr. Claus A. M. Seidel
Co-supervisor: Prof. Dr. Peter Gilch

Date of the oral examination: 24.03.2017

To my parents and my brother

Scientific Meetings

18th International Workshop on “Single Molecule Spectroscopy and Ultrasensitive Analysis in the Life Science” September 5-7, 2012 in Berlin, Germany *(Poster)*.

13th Conference on Methods and Applications of Fluorescence (MAF 2013) September 8-11, 2013 in Genoa, Italy *(Poster)*.

1st Workshop on "Fluorescence correlation spectroscopy in polymer science” October 10-11, 2013 in Munich, Germany *(Oral Contribution)*.

Symposium “Host-Guest Interplay in Porous Systems” October 29, 2014 in Düsseldorf, Germany *(Poster)*.

14th Conference on Methods and Applications of Fluorescence (MAF 2015) September 13-16, 2015 in Würzburg, Germany *(Poster)*.

2nd Workshop on "Fluorescence correlation spectroscopy in polymer science” September 24-25, 2015 in Aachen, Germany *(Oral Contribution, winning the best presentation award)*.

Zusammenfassung

Molekulare Diffusion im Hydrogel

Als Ergebnis einer interdiziplinären Studie berichten wir über fundamentale und tiefgreifende Einsichten über die Diffusion von Makromolekülen (Dextran, „*guest*“) innerhalb und in das Hydrogel hinein (Polyacrylamid, „*host*“), sowie über die strukturellen Eigenschaften des dynamischen Polymernetzwerks.

Erstmalig zeigen wir eine maximale zeitliche Auflösung unter mikroskopischen bis makroskopischen Bedingungen in unserer Studie, die Brownsche Dynamik (BD) Simulation und drei weitere Methoden kombiniert: Multi-Parameter Fluoreszenz Image Spektroskopie (MFIS), Makroskopisches Transmissions Imaging (MTI) und Nukleare Magnetische Resonanz Spektroskopie (NMR). Die experimentellen Methoden zeigen das systemische Verhalten über einem Zeitraum von Nanosekunden (MFIS), Millisekunden/Sekunden (NMR) bis hin zu Tagen (MTI). Die Ergebnisse zur Diffusion sind unabhängig von den Methoden in sich stimmig.

Ein wichtiger Befund stellt der attraktive Einfluss der „*guest-host*“ Wechselwirkung auf die Diffusion des Makromoleküls dar, wohingegen gängige, in der Literatur beschriebene Modelle sich ausschließlich mit der hemmenden Wirkung des Hydogels (Ogston Model) beschäftigen. Die quantitative Charakterisierung gibt neue Einsichten über die Veränderung der „*guest“* Diffusion in Abhängigkeit vom pH und der Ionenstärke.

Zum ersten Mal, konnte MFIS, zusätzlich zu diffundierenden Molekülen, auch zeitlich gefangene („*trapped*“) Moleküle mit Diffusionszeiten über 10 ms detektieren. Dies wurde durch Ansiotropie-Analysen bestätigt und durch MTI unterstützt. Die experimentellen Übereinstimmungen werden weiterhin durch BD-Simulationen bestätigt, die die Bedeutung der attraktiven Wechselwirkungen zwischen „*guest*“ und „*host*“ darlegen. Angesichts der signifikaten Unterschiede der für die Porengröße von Hydrogelen ermittelten Literaturwerte (nm bis µm), gibt die BD-Simulation eine wertvolle Abschätzung der Porengröße im nm-Bereich unter verschiedenen Bedingen ab. Außerdem können wir erstmals durch MFIS, MTI und NMR zeigen, dass die Diffusionskoeffizienten von Dextran-Molekülen in Lösungen und im Polyacrylamid-Hydrogel über große Zeiträume in sich konsistent sind und damit als Richtgrößen für zukünftige Studien dienen können. Um Einblicke in die Prinzipien zu bekommen, die der Diffusion von Makromolekülen durch das Hydrogel zu Grunde liegen, liefern BD-Simulationen wichtige physikalische Einblicke auf Wechselwirkungen auf

Makromoleküle durch das Polymernetzwerk, seine Porengröße und Interaktion mit Makromolekülen.

Photochemie eines Fluorophors

Fluoreszenzkorrelationsspektroskopie (FCS, Teil von MFIS) ermöglicht die Studie der Photochemie von Fluorophoren. Diese Methode ermöglicht Aussagen über den besten Weg zur Stabilisierung von Farbstoffen und um konsequenterweise ihr Fluoreszenzsignal zu verbessern. Um Cy5 zu stabilisieren, wurden 4-(phenylazo)-bezoin Säure (AZB-C) und Trolox als Quencher verwendet.

Diese Arbeit beiinhaltet zwei unterschiedliche Vorgehen:

(i) Die Verwendung von Quenchern als Zusätze (Additive) in Lösung;

(ii) Die Verwendung von Quenchern kovalent an Cy5 gebunden: Cy5-AZB-C und Cy5-Trolox.

FCS - kombiniert mit der *Saturation-Plot* Analyse - wird verwendet um den Fluoreszenz-Output von Cy5 und den Cy5-Konjugaten unter verschiedenen Bedingungen zu beschreiben.

Im Fall der Additive zeigen die Experimente, dass AZB-C ein guter Triplett-Quencher ist und dass AZB-C in oxidierenden Umgebungen, wenn die Produktion von $R^{\bullet+}$ durch Wasser stabilisiert wird, diese Zustände teilweise reduziert. Im Gegensatz dazu hat Trolox keinen Einfluss auf den Radikal-Term und beeinflusst ausschließlich den Triplett-Zustand, wenn auch weniger effektiv als AZB-C.

Die zweite Methode wurde erst vor kurzem eingeführt und hat den Vorteil, alle Probleme, die durch die biologische Toxizität der Additive entstehen, zu umgehen. Die FCS Experimente zeigen für die Cy5-Konjugate, dass Cy5-AZB-C den besten Weg darstellt, um den Radikal-Zustand bei Hochdosis-Bestrahlung im luftgesättigten Puffer zu unterdrücken und den Triplett-Zustand in Argon-haltigen Experimenten zu vermindern. Diese Befunde können mit einer lokal sehr hohen Konzentration des Quenchers am konjugierten Farbstoff erklärt werden. Unglücklicherweise zeigen Cy5-Konjugate unter Pufferbedingungen eine geringere Quantenausbeute als Cy5 alleine. Daher ist das Fluorszenzsignal von zugesetzten Additiven höher. In Ethanol dagegen ist das Verhalten der Additive und der Cy5-Konjugate vergleichbar auf Grund der Verminderung der Singulett-Löschung auf das neue Konjugat.

Die Kombination aus FCS und Photo-Bleichexperimenten erklären die wichtigsten Photoschädigungswege „*photo damage pathways*“ der Fluorophore, sowie den Einfluss von Sauerstoff und des Lösungsmittels. Die Anwesenheit von Sauerstoff im Puffer fördert die schnellste Degradation des freien Farbstoffes; der Gebrauch von Cy5-AZB-C ist daher der

beste Weg um Photoschädigung zu verlangsamen. Im Ethanol-Puffer versetzt mit Argon und luftgesättigt, nimmt die Photostabilität des freien Farbstoffes enorm zu. In sauerstofffreiem Ethanol ist die Cy5-Photostabilität maximal im Vergleich zu den anderen Bedingungen. Unter luftgesättigten Bedingungen ist der Singulett-Zustand der prominenteste Weg des Photobleichens, unter Argon-haltigen Bedigungen eher der Triplett-Zustand. Daher ist der Entzug von Sauerstoff in Kombination mit einem Triplett-Quencher die beste Strategie um das Fluoreszenzsignal von Fluorophoren zu verbessern.

Fazit

Zusammenfassend zeigt diese Arbeit die einzigartigen Vorteile der MFIS und FCS quantitativen Analyse. Die in dieser Studie verwendete Methode erlaubt (i) die Charakterisierung eines Polymers, eines der zur Zeit wichtigsten Materialen, und (ii) die Untersuchung der Photochemie von Fluorophoren um ihre Stabilität zu verbessern und ideale Chromophore zu generieren.

Summary

Molecular diffusion in a hydrogel

Quantitative description of pore size distributions and the influence of probe/matrix interactions in literature are widely unknown. Therefore, characterization of the hydrogels is needed.

As an outcome of the interdisciplinary study, fundamental and comprehensive insights are reported on the diffusion of macromolecules (dextrans, guest) into and inside hydrogels (polyacrylamide, host) and on structural information about these dynamic polymer matrices. It is provided for the first time a full time and length scale study combining Brownian dynamics (BD) simulations and three experimental methods: multi-parameter fluorescence image spectroscopy (MFIS), macroscopic transmission imaging (MTI) and nuclear magnetic resonance spectroscopy (NMR). The experimental methods probe the system's behavior from the nanosecond range (MFIS), through the millisecond/second range (NMR) up to days (MTI). The results on diffusion are consistent over this very wide time range, which also implies consistency on a correspondingly large length scale range.

A crucial novel finding is the influence of attractive guest-host interactions on the guest diffusion, whereas common models in the literature focus only on the hindrance by the hydrogel network (Ogston model). The quantitative characterization provides new insights and explains the change in guest diffusion upon changing pH and ionic strength.

In addition to the diffusing molecules, MFIS could for the first time detect temporarily trapped molecules with diffusion times above 10 ms. This was also confirmed by anisotropy analysis and could be further supported by MTI.

The experimental agreement is further corroborated by BD simulations supporting the importance of the attractive interactions between guest and host.

In view of the significant discrepancy between values for pore size of the hydrogels reported in literature (ranging from nm to μm), the BD simulations provide also valuable estimates for the pore size under the different conditions (nm range).

It has been shown for the first time that the diffusion coefficients of dextran molecules moving in solution and in a polyacrylamide hydrogel determined by MFIS, MTI and NMR, which imply different length and time scales, are mutually consistent and may serve as a benchmark for future studies. To shed light on the principles governing the diffusion of macromolecules through hydrogels, BD simulations provide significant physical insights on

the hindrance by the polymer network, its pore size and its interactions with the macromolecules.

Photochemistry of a fluorophore

Fluorescence correlation spectroscopy (FCS that is part of MFIS) permits the study of the photochemistry of fluorophores. Such a method gives suggestions regarding the best way to stabilize dyes and consequently how to improve the fluorescence signal. To stabilize the dye Cy5, 4-(phenylazo)-benzoic acid (AZB-C) and Trolox are used as quenchers. This work involves two different approaches:

(i) the usage of quenchers as additives dissolved in solution;

(ii) the usage of quenchers covalently linked to Cy5: Cy5-AZB-C and Cy5-Trolox.

FCS, in combination with saturation plot analysis, is used to describe the fluorescence output of Cy5 and Cy5-conjugates in different experimental conditions.

For additives, the experiments show that AZB-C is a moderate triplet quencher and in oxidizing conditions, where the production of $R^{\bullet+}$ is stabilized by H_2O, AZB-C is able to reduce such state partially. Differently, Trolox has no influence on the radical term and affects only the triplet state but with less effectiveness compared to AZB-C.

The second method has been introduced recently and has the advantage of overcoming problems due to the biological toxicity of the additives. For Cy5-conjugates, the FCS experiments show that Cy5-AZB-C is the best way to suppress the production of radical state at high power irradiance in air saturated buffer and it decreases the triplet state dramatically in argon experiments. Such findings could be explained with the high formal local concentration of the quencher in the conjugated compound. Unfortunately, in buffer conditions Cy5-conjugates show a lower fluorescence quantum yield in comparison to Cy5, demonstrating therefore that the additives still give higher fluorescence signal. In ethanol, the behavior of the additives and the Cy5-conjugates is similar due to the decrease a singlet quenching in these new compounds.

The combination of FCS and photobleaching experiments provided information on the most relevant photodamage pathways of fluorophore, the influence of oxygen and the solvent on those processes. Since, the presence of O_2, in buffer promotes the fastest degradation of the free dye; the usage of Cy5-AZB-C is the best way to reduce the photodestruction. In buffer under argon and in air saturated EtOH, the photostability of the free dye greatly increases. In deoxygenated EtOH the Cy5 photostability is the highest in comparison to other conditions.

The prevalent photobleaching pathway under air saturated conditions comes mostly from the singlet state and in argon solution from triplet state. Therefore, a good strategy to improve the fluorescence signal is the removal of O_2 in combination with triplet quencher.

In conclusion, this work demonstrates the unique advantages of the MFIS and FCS quantitative analysis. The methodology used in this study permits: (i) to characterize a polymer that is one of the most important materials at the present day and (ii) to study the photochemistry of fluorophores in order to improve their stability and getting an ideal chromophore.

Paper and Manuscript

Chapter 2 Diffusion of macromolecules in a polymer hydrogel: from microscopic to macroscopic scales

Current status: published in ***Phys. Chem. Chem. Phys.***, 2016,**18**, 12860-12876

Deborah Sandrin, Dana Wagner, Christoph E. Sitta, Roland Thoma, Suren Felekyan, Helen E. Hermes, Christoph Janiak, Narder de Sousa Amadeu, Ralf Kühnemuth, Hartmut Löwen, Stefan U. Egelhaaf, Claus A. M. Seidel

- D.S., D.W. and R.T. prepared the samples;
- D.S. and R.K. performed confocal fluorescence image spectroscopy (MFIS), D.W. macroscopic transmission imaging, R.T. NMR spectroscopy;
- D.S., D.W., R.T., S.F., N.A. and R.K. analyzed the data;
- C.E.S. performed the Brownian dynamics simulations;
- S.F. developed the software for MFIS analysis;
- H.E.H., N.A., R.K., H.L., S.U.E. and C.A.M.S. designed the research and supervised the project;
- D.S., D.W., C.E.S., R.T., S.F., H.E.H., C.J., N.A., R.K., H.L., S.U.E. and C.A.M.S. interpreted the data and wrote the manuscript.

Seidel group in total: 39%			
D.S.	S.F.	R.K.	C.A.M.S.
20%	4%	10%	5%

Chapter 3 Strategies to improve the fluorescence signal and photostability of the cyanine dye Cy5

Current status: manuscript in preparation

Deborah Sandrin, Denis Dörr, Ralf Kühnemuth, Bernhard Mayer, Thomas J. J. Müller, Claus A. M. Seidel

- D.S. performed the organic synthesis;
- R.K. developed the FCS and bleaching set-up;
- D.S. performed the experiments;
- D.D. developed the mathematical model for analysis;
- D.S., D.D. analyzed the data;
- R.K., B.M., T.J.J.M. and C.A.M.S. designed the research and supervised the project;
- D.S., D.D., R.K. and C.A.M.S. interpreted the data and wrote the manuscript.

Seidel group in total: 90%			
D.S.	D.D.	R.K.	C.A.M.S.
55%	27%	4%	4%

Contents

Chapter 1 General Introduction

1.1 The advantages of single molecule fluorescence spectroscopy

In the 1990s, the single-molecule fluorescence techniques using biological samples began to appear in the scientific world.[1-5] The exponential growth of such techniques is due to its ability to quantify directly heterogeneous molecular populations. In this way, it becomes possible to understand time-dependent fluctuations in the structure and dynamics of molecular systems. Such information is difficult to obtain from ensemble measurements; deconvolution methods of the time response function are needed. Therefore, fluorescence microscopy and in particular fluorescence imaging is an essential tool for understanding biological systems.

The challenge in the last years is to improve the imaging resolution, in order to obtain more precise results in terms of the molecular structure. Recently, a new technique called expansion macroscopy[6] permits the production of higher resolution images in cells and tissues taking advantage of the swelling of a polymer gel. In general, polymers are one of the most important materials[7] at the present day. They are widely used in analytical and preparatory techniques (chromatography,[8] genomics,[9] biofilms[10]) as well as in biomedical (imbibition,[11] controlled drug delivery,[12-15] flow control,[16] implantable devices,[15] contact lenses,[17] cellular and tissue engineering[18, 19]) and technical applications (enhanced oil recovery[20, 21]). Since, the basic mechanisms between matrix and tracer are not yet completely understood, the characterization of the structural properties of the polymer is crucial.

Another problem that could compromise the fluorescence imaging resolution is the instability of fluorophores. Indeed, fluorescence microscopy requires the indispensable usage of dyes directly linked to biomolecules. Unfortunately, the fluorophores are not ideal and in addition to their regular photon emission, they may give rise to instability. The processes involved are mainly blinking[22] between bright and dark states and permanent photodamage.[23-25] Therefore, the stability of the fluorophore is important to maximize the fluorescence signal crucial for successful experiments. Until now, the usage of additives seems the only possible way to increase the fluorescence signal.[26, 27] Recently, in a new approach, a dye is covalently linked to a quencher to stabilize the fluorophores. This is often the only option tolerated by the biological systems.[28-32]

Multiparameter fluorescence image spectroscopy (MFIS)[33, 34] is an important tool in fluorescence imaging that records multiple fluorescence parameters simultaneously with

picoseconds accuracy over time periods of hours. The eleven parameters taken into account are three spatial dimensions (x, y, z) and eight fluorescence parameters, namely fluorescence anisotropy, lifetime, intensity, detection time, excitation spectrum, emission spectrum, fluorescence quantum yield and distance between two fluorophores. In this way, for each pixel not only is the signal intensity known but also all other fluorescence parameters.

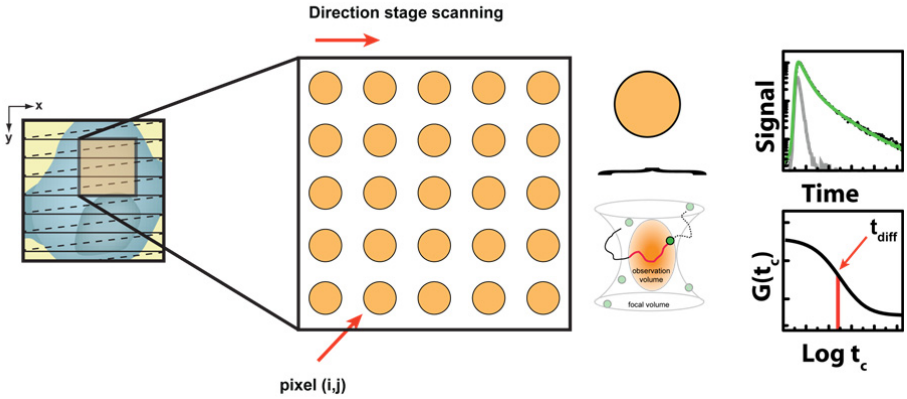

Figure 1.1. Schematic representation of image with different pixels. For each pixel, multiple fluorescence parameters are recorded.

It is possible to identify and select a species population in the fluorescence parameter histogram and afterwards locate this population in the image.

Additionally, as fluctuations are recorded, furthers analyses such as fluorescence correlation spectroscopy (FCS),[35] fluorescence cross-correlation spectroscopy (FCCS),[36] or fluorescence intensity distribution analysis (FIDA)[37] are possible.[5]

The origin of FCS dates back to 1972[38], but it took several developments to reach the capacity that it has in the present day. Indeed, now it is a very versatile tool that permits the investigation of very different systems, ranging from biological systems, photo-photdynamical properties of fluorescent dyes to polymeric materials.[7, 39, 40] The wide applicability of FCS is due to at least four advantages: (i) minimally invasive technique, (ii) high sensitivity, (iii) low sample amount and (iv) high spatial and temporal resolution. The application of an appropriate mathematical model to the FCS curves gives quantitative information about the processes that are involved in the system.

Therefore, MFIS and consequently FCS are suitable tools to characterize polymer matrices using fluorescence tracers to probe the structure.[41] Moreover, FCS permits the investigation of the photophysical properties of fluorescent dyes, in terms of the dark states involved and the fluorescence signal.

1.2 Structure of the thesis

In a polymer hydrogel, the significance of sieving, entanglements, (chemical) interactions, partitioning, oscillation of pores is still controversially discussed.[41-47] In addition, the average size of the pores is also under debate.[43, 48-52 53, 54]

The goal is to give a quantitative description of pore size distributions and the influence of probe/matrix interactions in the hydrogel.

In Chapter 2 the characterization of polyacrylamide hydrogel is presented by using three complementary experimental methods combined with Brownian dynamics simulations, to study the transport principles that are governing the system.

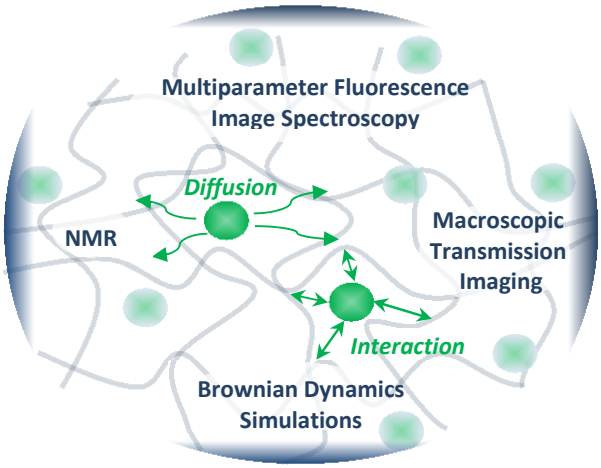

Figure 1.2. Schematic representation of the polyacrylamide hydrogel (blue lines) characterized with dextran molecules (green spots) using four complementary methods: MFIS, MTI, NMR and BD simulations. The two processes involving between the guest-host are diffusion trough the pores and interactions.

Dextrans molecules labelled with fluorescent dyes (fluorescein sodium salt (FLU), Alexa Fluor 488 (A488), tetramethylrhodamine (TMR)) are used like tracers. The molecular weight of the dextrans is varied between MW=3 kDa to 2000 kDa. For comparison the diffusion of free dyes, FLU, A488 and TMR is also studied in the hydrogel.

The long time diffusion coefficients of dextran molecules moving in solution and in a polyacrylamide gel matrix are determined on different length scales by using MFIS, MTI and NMR. Combining experiments and simulations enables to achieve a better understanding of the effects influencing the diffusion of molecules in the gel network. Moreover, MFIS detects tracer-matrix interactions and pixelwise analysis permits to see significant heterogeneity of the gel on the microscopic scale.

In Chapter 3, the photochemistry of Cy5 is studied, using quenchers to achieve the most ideal fluorophore. The model used involves the application of the electronic energy diagram of rhodamine fluorophore [55, 56] combined with the isomerization state typically present in cyanine dye.[35]

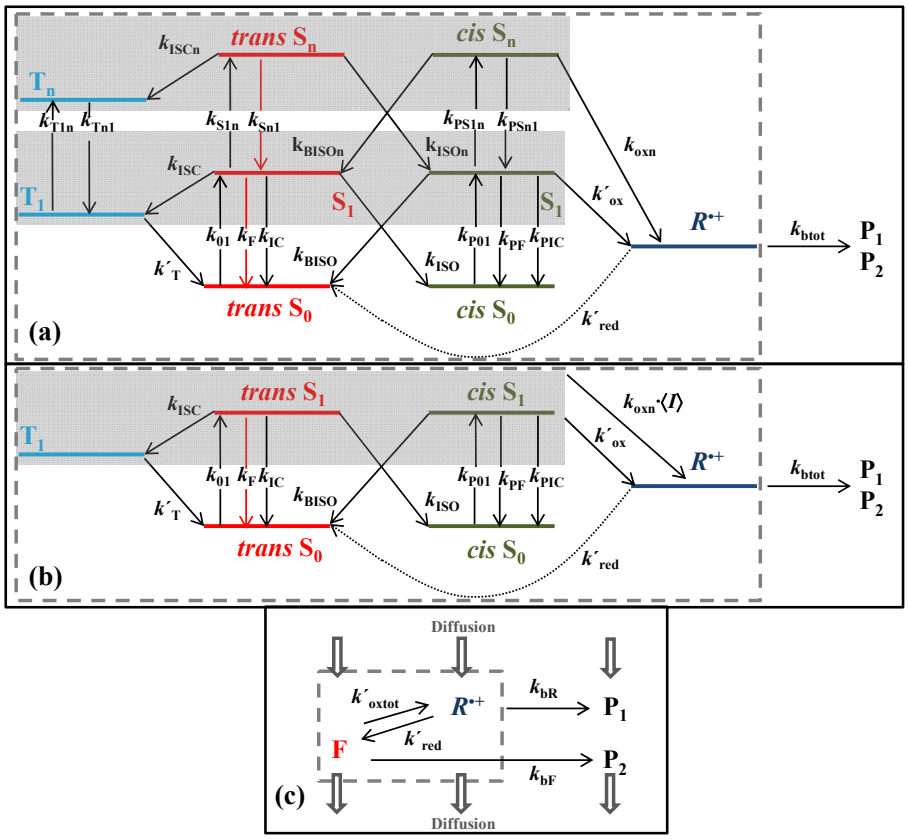

Figure 1.3. (a) Electronic energy diagram for cyanine dye where the contributions of higher excited electronic states (S_n and T_n) are directly considered. (b) Simplified scheme for Cy5 where the higher excited states are considered using irradiance dependent rate k_{oxn}. After the excitation process from *trans* S_0 to *trans* S_1 (k_{01}) the S_1 depopulation can occur via the typically fluorescence emission (k_F), internal conversion (k_{IC}), intersystem crossing (k_{ISC}) or photoinduced *trans-cis* isomerization (k_{ISO}). Once the dye is in *cis* S_0 state, it can be excited in *cis* S_1 and going back (k_{BISO}) to the *trans* state. The fluorescence quantum yield of the *cis* isomer is considered negligible (k_{PF}).[35] The photo-oxidation (k'_{ox}) can happen from all 3 excited states: singlet *trans* (S_1), singlet *cis* (S_1) and triplet (T_1) originating the radical cation ($R^{\bullet+}$). The consequent photobleaching (dashed grey line) can occur from all the states (k_{btot}). (c) Further simplification of the scheme with the photo-oxidation (k'_{oxtot}) and reduction (k'_{red}) of Cy5 and consequent photodamage from $R^{\bullet+}$ state (k_{bR}) and from F state (k_{bF}) generating products ($P=P_1+P_2$) is shown.

The Figure 1.3(a) shows the contributions of all the states involved, considering also the higher excited states (S_n and T_n). Figure 1.3(b) shows the model applied in the analysis, where the contribution of S_n and T_n states is given by k_{oxn} depending from on the excitation power. For Cy5, in addition to the regular photon emission (k_F) from a *trans* singlet excited state (*trans* S_1), the deactivation can occur via internal conversion (k_{IC}), intersystem crossing (k_{ISC}) or photoinduced *trans-cis* isomerization (k_{ISO}). When the dye is in *cis* S_0 state, it can be excited to *cis* S_1 and goes back (k_{BISO}) to the *trans* state. The fluorescence capacity of the *cis* isomer is considered negligible (k_{PF}).[35] The possible photo-oxidation (k'_{oxtot}) and reduction (k'_{red}) can happen from all 3 excited states (grey square): *trans* S_1, *cis* S_1 and T_1 originating the radical cation ($R^{\bullet+}$). Consequently, photobleaching (k_{btot}) can occur from all the states (dashed grey line). In Figure 1.3 (c), a further simplified electronic scheme used in the data analysis is shown.

The goal is to apply different strategies in order to overcome problems due to the generation of dark states and instability of the dye.

The use of additives seemed to be the only available option to improve the photostability of the fluorophores until a new approach was introduced, where the quenchers are covalently linked to the dye.[29, 31] A comparison between the use of additives and the new compounds obtained with chemical synthesis is presented in Chapter 3. The characterization involves ensemble spectroscopy measurements, steady-state bleaching experiments and quantitative FCS in different solvents and environments. The investigation shows the best way to stabilize Cy5 and the highest fluorescence signal obtainable.

Chapter 2 Diffusion of macromolecules in a polymer hydrogel: from microscopic to macroscopic scales

D. Sandrin, [1,*] D. Wagner, [2,*] C. E. Sitta, [3,*] R. Thoma, [4] S. Felekyan, [1] H. E. Hermes, [2] C. Janiak, [4] N. de Sousa Amadeu, [4] R. Kühnemuth, [1,†] H. Löwen, [3,‡] S. U. Egelhaaf, [2,§] C. A. M. Seidel [1,¶]

[1] *Institut für Physikalische Chemie II, Molekulare Physikalische Chemie,*

Heinrich-Heine-Universität, Universitätsstr. 1, 40225 Düsseldorf, Germany

[2] *Institut für Experimentelle Physik der kondensierten Materie,*

Heinrich-Heine-Universität, Universitätsstr. 1, 40225 Düsseldorf, Germany

[3] *Institut für Theoretische Physik II: Weiche Materie,*

Heinrich-Heine-Universität, Universitätsstr. 1, 40225 Düsseldorf, Germany

[4] *Institut für Anorganische Chemie und Strukturchemie,*

Heinrich-Heine-Universität, Universitätsstr. 1, 40225 Düsseldorf, Germany

*these authors have contributed equally to this work

† ralf.kuehnemuth@hhu.de; corresponding author

‡ hlowen@hhu.de; corresponding author

§ stefan.egelhaaf@hhu.de; corresponding author

¶ cseidel@hhu.de; corresponding author

Abstract

To gain insight into the fundamental processes determining the motion of macromolecules in polymeric matrices, the dynamical hindrance of polymeric dextran molecules diffusing as probe through a polyacrylamide hydrogel is systematically explored. Three complementary experimental methods combined with Brownian dynamics simulations are used to study a broad range of dextran molecular weights and salt concentrations. While multi-parameter fluorescence image spectroscopy (MFIS) is applied to investigate the local diffusion of single

molecules on a microscopic length scale inside the hydrogel, a macroscopic transmission imaging (MTI) fluorescence technique and nuclear magnetic resonance (NMR) are used to study the collective motion of dextrans on the macroscopic scale. These fundamentally different experimental methods, probing different length scales of the system, yield long-time diffusion coefficients for the dextran molecules which agree quantitatively. The measured diffusion coefficients decay markedly with increasing molecular weight of the dextran and fall onto a master curve. The observed trends of the hindrance factors are consistent with Brownian dynamics simulations. The simulations also allow us to estimate the mean pore size for the herein investigated experimental conditions. In addition to the diffusing molecules, MFIS detects temporarily trapped molecules inside the matrix with diffusion times above 10 ms, which is also confirmed by anisotropy analysis. The fraction of bound molecules depends on the ionic strength of the solution and the charge of the dye. Using fluorescence intensity analysis, also MTI confirms the observation of the interaction of dextrans with the hydrogel. Moreover, pixelwise analysis permits to show significant heterogeneity of the gel on the microscopic scale.

2.1 Introduction

The motion of macromolecules through disordered matrices is of great importance in analytical and preparatory techniques (chromatography,[8] expansion microscopy,[6] genomics,[9] biofilms[10]) as well as in biomedical (imbibition,[11] controlled drug delivery,[12-15] flow control,[16] implantable devices,[15] contact lenses,[17] cellular and tissue engineering[18, 19]) and technical applications (enhanced oil recovery[20, 21]). From a fundamental point of view, precise measurements for model systems are needed to reveal the underlying transport principles.[57-60] It is known that the presence of obstacles slows down the transport and that this is more pronounced for larger molecules. However, the basic underlying mechanisms and their effects are not yet completely understood. In particular, the motion of particles through a gel matrix represents an intricate problem as the gel matrix can respond to the particle motion. A nontrivial dependence of the diffusion behavior on both the host and the guest, i.e. the gel and the diffusing particles, is expected. The behavior of the host is mainly characterized by a typical pore size. However, topological constraints resulting from the nontrivial and dynamically changing connectivity of the pores[61] also have an impact on the diffusion of the guest molecules. This connectivity is expected to result in a wide spread in the translocation rate of the individual particles. The translational rate is also influenced by

the structural properties of the guest molecules such as hydrodynamic radius, shape, molecular weight or charge distribution. The significance of sieving, entanglements, (chemical) interactions, partitioning, oscillation of pores etc. is still controversially discussed.[41-47] In addition, the average size of the pores is also under debate.[43, 48-54]

It is accepted that the mesh sizes in polymer hydrogels depend on the specific gel preparation such as (I) the mass concentration of polymeric material in the reaction solution, [T], and (II) the weight fraction of cross-linker, C_R, but the absolute average size of the pores is subject to debate.[43, 48-54] Considering hydrogels (0.035 g/ml $\leq$ [T] $\leq$ 0.065 g/ml, 0.02 $\leq C_R \leq$ 0.05) with similar compositions to the one studied here ([T] = 0.04 g/ml, C_R = 0.035), different methods give very different results for the pore sizes (please note that the numbers given for [T] and C_R, multiplied by 100, correspond to the parameters %T and %C, respectively, which were used in the above publications). The reported pore sizes range from 2.00 – 2.25 nm (chromatography[49]) through 5 – 9 nm (electrophoresis studies in the 1960s and 1980s[50, 51]) and 60 – 156 nm (electrophoresis studies in 1991[43, 48]) up to values of 2 – 20 µm (for the largest pores found by scanning electron microscopy[52-54]). This also complicates any systematic study of particle diffusion in a well-characterized model system, which however is important to understand the principles of translocation and to test theoretical approaches.

Here we study polymeric dextran molecules diffusing through a polyacrylamide hydrogel without interfering with the sample during the measurements. We use dextrans as tracer particles, because they have a good water solubility, low toxicity, relative inertness and are flexible polymers. Moreover, they are commercially available over a broad range of molecular weights and hence sizes. Most dextrans can be also obtained as derivatives labelled with fluorescent dyes (fluorescein sodium salt (FLU), Alexa Fluor 488 (A488), tetramethylrhodamine (TMR)). The molecular weight of the dextrans is varied between M_W=3 kDa to 2000 kDa. For comparison the diffusion of free dyes, FLU, A488 and TMR is studied in our hydrogel, too. To investigate the interactions of the particles with the hydrogel in more detail, we study the influence of solution conditions like pH-value, salt and tracer particle concentrations. Using three complementary methods, multiparameter fluorescence image spectroscopy (MFIS), macroscopic transmission imaging (MTI) with fluorescence detection and nuclear magnetic resonance (NMR), we measure the long-time diffusion coefficient of the fluorescently labelled and unlabelled probe particles, respectively. MFIS also allows us to detect the heterogeneity of the gel. The data are compared to a model by Ogston[62] which predicts the dynamical hindrance in a network of randomly distributed fibers

due to geometric confinement. The Ogston model provides a simple analytical formula for the particle dynamics via an effective excluded volume. Another theoretical approach is to perform computer simulations. As modeling a hydrogel on an atomic basis over huge length- and timescales is computational unaffordable, various different model assumptions including different degrees of molecular details have been used in the past.[63-75] The most detailed model for the gel matrix was used by Linse and coworkers[63-66] and Holm and coworkers[67-69] who resolved the monomers of the polymer chains connecting the nodes explicitly within a bead-spring model. Within their approach the swelling behavior of the gels was explored but the diffusion of tracer particles within the gel network was not addressed. In a more coarse-grained approach, the matrix was described by either a static network of points,[70] rods,[70, 71] or chains[72] or as fluctuating network of spheres[73, 74] which indeed allows for the computation of tracer diffusion. Following the latter coarse grained approach of Zhou and Chen,[74] we perform Brownian dynamics (BD) simulations representing three different levels of complexity to resolve the different physical effects that are operating in the hydrogel. Our simulation study provides a simple and systematic framework, taking into account the flexibility of the matrix particles, the effective dextran-matrix excluded volume and finding strong indications for effective attractive interactions. Our combined results provide consistent picture of polymers diffusing through a hydrogel matrix and may serve to test more quantitative theories and other experimental approaches.

2.2 Materials and Methods

2.2.1 Samples

2.2.1.1 Hydrogel: a polymer matrix in an aqueous environment

The polyacrylamide (PAAm) hydrogels were formed by copolymerization of acrylamide (AAm, monomer) with the tetrafunctional cross-linking agent N,N'-methylenebis (acrylamide) (BIS), using ammonium peroxodisulphate (APDS) and tetramethylethylenediamine (TEMED) as redox initiators. The monomer and cross-linker were both purchased from Sigma-Aldrich, APDS from Roth and TEMED from Merck. All components were used without further purification. AAm, BIS and APDS were separately dissolved in deionized and filtered water and cooled to 4 °C. The individual solutions were then mixed at a low temperature. The reaction mixture contained 75 mg of AAm, 2.71 mg of BIS, 6 mg of APDS and 10 µl of TEMED in a total volume of 2 ml which corresponds to a molar ratio of cross-linker to monomer of 1:60. The total monomer concentration, defined as

the mass concentration of AAm and BIS in the total reaction volume, is [T] = 0.04 g/ml and the weight fraction of cross-linker with respect to the total mass of the polymeric material (AAm and BIS) is C_R = 0.035.

After mixing, the solution was transferred to Teflon molds and allowed to warm up and react at room temperature. After one to two hours, polymerization was complete and the hydrogel was transferred into a larger container filled with deionized water. The gel was left for five days to ensure that the hydrogel swells to equilibrium. The excess water was exchanged daily to wash out residual chemicals that had not reacted in the gelation process.[76]

Discs with a radius $R_d \approx 0.3$ cm were cut from the hydrogels using a simple stamp. In corresponding MTI and MFIS experiments, samples cut from one gel block were used. For the NMR measurements, the gelation process was carried out in cylindrical Teflon molds ($R_d \approx 0.5$ cm, height 5 cm). The hydrogels were then transferred into a container filled with deuterium oxide.

The hydrogel was characterized by determining the polymer volume fraction in the fully swollen state, φ, the average molecular weight between cross-linking points, M_c, and the mesh size, ξ. The polymer volume fraction of the hydrogel in the swollen state φ was calculated directly from eq. (2.1):[77, 78]

$$\varphi = \frac{V_p}{V_{gel}} = \frac{m_p \rho_{H_2O}}{m_p \rho_{H_2O} + (m_{H_2O} \rho_p)} \tag{2.1}$$

where V_p is the volume of the dry polymer (PAAm), V_{gel} is the volume of the hydrogel after equilibrium swelling, m_p is the mass of the polymer, m_{H2O} is the mass of water in the swollen gel and ρ_p and ρ_{H2O} are the densities of polymer and water, respectively.

The mass of the fully swollen hydrogel was measured after removing the liquid on the surface of the hydrogel with a pipette. It was then dried at 40 °C under vacuum for at least 6 h until constant weight was reached to determine m_p. The experiment was repeated for different pieces of hydrogel, and the mass fraction was converted into volume fraction using the known polymer density (ρ_p=1.3 g/cm^3).[79]

The theoretical molecular weight of the polymer between cross-links M_c is related to the degree of cross-linking in the hydrogel, X (i.e., the molar ratio of cross-linker to monomer) and the molecular weight of the repeating units ($M_{r,PAA}$=71.1 g/mol):[78, 80]

$$M_c = \frac{M_r}{2X} \tag{2.2}$$

The mesh size, ξ, which characterizes the space between macromolecular chains can be calculated using:[77, 81, 82]

$$\xi = \varphi^{-1/3}\zeta\left(\frac{C_n 2M_c}{M_r}\right)^{1/2} \tag{2.3}$$

where C_n is Flory's characteristic ratio ($C_{n,\,PAA}$=2.72) and ζ is the carbon-carbon bond length (ζ=0.154 nm).[83] This calculation assumes ideal solvent quality, homogeneous cross-linking densities and Gaussian distribution of chain lengths.

We characterized the polyacrylamide hydrogels as used in these experiments, i.e. in water and in a 20 mM potassium carbonate buffer at pH 10. The results are shown in Table 2.1.

	PAAm in water	**PAAm pH 10**
φ	0.0390 ± 0.0004	0.0150 ± 0.0001
M_c **[g/mol]**	2141	2141
ξ **[nm]**	5.7 ± 0.1	7.8 ± 0.1

Table 2.1. Polymer volume fraction in the swollen state (φ), molecular weight of the polymer between cross-links (M_c) and mesh size (ξ) for the PAAm hydrogel in water and in potassium carbonate buffer 20 mM at pH 10. The errors are the standard errors of repeated measurements of the polymer volume fraction.

2.2.1.2 Diffusing polymeric guest molecules

The dextrans (Table 2.2) and free dyes were purchased from Invitrogen. For the NMR experiments, unlabelled dextrans were dissolved in deuterium oxide with a purity of 99.9 % from Deutero GmbH. For the remaining experiments, dextrans conjugated with Alexa Fluor 488 (A488) or tetramethylrhodamine (TMR) were dissolved in deionized water. To exclude fluorescence blinking due to protonation-deprotonation dynamics, dextrans labelled with fluorescein (FLU) were prepared in potassium carbonate buffer at pH=10, (20 mM) and the fluorescence measurements were conducted after addition of 100 µM Trolox (Sigma-Aldrich) to avoid photobleaching of the dye.

To investigate the local environment and possible probe-polymer interactions inside the gel matrix, we measured the most polar dye attached to one of the smaller dextrans, A488-D10 under five different conditions: (i) H_2O, (ii) aqueous $KClO_4$ solution (10 mM, 20 mM, 40 mM, and 60 mM), (iii) aqueous KCl solution (20 mM), (iv) aqueous potassium carbonate buffer (20 mM) at pH=7, and (v) at pH=10.

M_w [kDa]	Unlabelled	Alexa fluor 488	Tetramethyl rhodamine	Fluorescein
0.33				FLU
0.39			TMR	
0.53		A488		
3	D3	A488-D3	TMR-D3	FLU-D3
10	D10	A488-D10	TMR-D10	FLU-D10
40	D40		TMR-D40	FLU-D40
70			TMR-D70	
500				FLU-D500
2000			TMR-D2000	

Table 2.2. Overview of dyes and dextrans of different molecular weights, M_w, as obtained from manufacturer (for labelled dextrans already including the dye) and their naming convention. The dextrans were either unlabelled or conjugated with one of three different dyes: Alexa Fluor 488, tetramethylrhodamine and fluorescein. For more detailed information see S1.1 and S1.2.

2.2.1.3 Addition of polymeric guest molecules to the hydrogel

For MFIS experiments, each hydrogel disc was placed in a chambered cover glass (Lab-Tek™, Thermo Fisher Scientific, USA), incubated with guest molecule solution (400 µl in total) and allowed to reach equilibrium before the measurement was started (2 to 7 days depending on dextran size). When electrolyte solutions were used, the solution was exchanged approximately every 12 h during the incubation period to ensure defined concentrations.

In the MTI experiments, the initial particle concentration in the hydrogel was 0 and the concentration in the surrounding solution was varied between 0.1 and 10 µM. The hydrogel matrix was contacted with the particle (dye or dextran) solution at the beginning of the experiments and the diffusion of guest molecules from the solution into the hydrogel was studied.

For NMR measurements, the hydrogel cylinders were incubated with concentrated amino dextran solution in deuterium oxide for at least 48 h. The samples were then carefully transferred into NMR tubes ensuring that the gel texture was not destroyed. Concentrations below 1 mM were used in order to avoid aggregation. Bubbles were successfully avoided.

2.2.2 Measurement Methods

2.2.2.1 Multiparameter Fluorescence Image Spectroscopy (MFIS)

All measurements were conducted on a confocal fluorescence microscope (FV1000 Olympus, Hamburg, Germany), which had been modified to allow time-resolved experiments.[34, 84] A488 and FLU were excited using a polarized pulsed diode-laser (LDH-D-C-485, PicoQuant, Berlin, Germany) at 485 nm, while for TMR a supercontinuum laser (SuperK Extreme, NKT Photonics, Birkerød, Denmark) at 555 nm was employed. Laser light was directed into a 60x water immersion objective (NA=1.2) by a dichroic beam splitter and focused into the sample close to the diffraction limit. The light emitted was collected by the same objective and separated into two polarizations (parallel and perpendicular) relative to the excitation beam. The fluorescence signal was further divided into two spectral ranges (BS 560, AHF, Tübingen, Germany). Bandpass filters for A488/FLU and TMR fluorescence (HC 520/35 and HC 607/70, AHF), were placed in front of the detectors. The signal from single photon sensitive detectors (PDM50-CTC, Micro Photon Devices, Bolzano, Italy and HPMC-100-40, Becker&Hickl, Berlin, Germany, respectively) was recorded photon-by-photon with picosecond accuracy (HydraHarp400, PicoQuant) and analyzed using custom software (LabVIEW based). The temperature during all measurements was 22.5 ± 0.5 °C and the concentration of the dextrans was adjusted between 0.05 and 3 nM, depending on their different degree of labelling.

The sample was mounted on a piezo-controlled x-y scanner (P-733.2CL, Physik Instrumente, Karlsruhe, Germany) and moved perpendicular to the optical axis. It was moved in a stepwise manner to permit multiparameter fluorescence detection at defined locations. The pixel size is defined by the step size of the scan (in our experiments 10.00 µm) while photons are collected from the confocal detection volume only (V_{det}=0.55 fl). The integration time per pixel was 30 min and the complete image contains 18 pixels (probed spots).

2.2.2.2 Macroscopic Transmission Imaging (MTI)

The macroscopic transmission imaging experiments were performed using a custom-built imaging apparatus similar to that described previously.[85] The sample was illuminated by a parallel beam of light from an LED lamp (CoolLED, center wavelength of 490 nm) whose wavelength was chosen to excite the fluorescent particles in the sample. Using a dichroic mirror that transmits wavelengths above and reflects wavelengths below 502 nm, the transmitted light was split into excitation light (bright-field transmission image) and emitted

light from the fluorophores (fluorescence image). The images were then focused onto separate CCD cameras. Additional fluorescence filters (excitation filter: 480/25, emission filter: longpass LP 520) were applied. The hydrogel discs were placed between two horizontally held glass plates with a fixed distance between the plates of 1.5 mm using aluminum spacers. This distance was chosen to ensure that the gels were compressed as little as possible but still in contact with both glass plates. The particle solution was added around the gel discs and allowed to diffuse into the gel matrix. The image collection time was varied between 5 s at the beginning and up to 300 s at the end of a measurement. Images were collected for 3 to 72 h. The sample cells were sealed to ensure that the solvent did not evaporate and measurements were performed at room temperature (23 °C).

2.2.2.3 Nuclear Magnetic Resonance (NMR)

A Bruker AVANCE DRX-500 NMR spectrometer operating at 500 MHz for ^{1}H was used. The spectrometer was equipped with a Bruker Great 1/10 gradient amplifier and a Bruker selective inverse (SEI) probe with z-gradient coils. The gradient amplitudes were calibrated using dodecane, 1-pentanol and water as standard samples.[86] The temperature sensor was calibrated using methanol as described by van Geet.[87] All diffusion measurements were acquired by using stimulated echo with bipolar gradient pulses (pulse program name STEBPGP).[88, 89] This sequence was also followed by a WATERGATE sequence to suppress the water signal.[90, 91]

In each experiment, the magnetic field gradient strength of the bipolar pulses was linearly arrayed along 16 values from 10 to 60 G/cm while all other parameters were kept constant. The gradient pulse length, δ, and the diffusion delay, Δ_N, were chosen such that the echo signal was suppressed considerably.

The diffusion coefficients of unlabelled aminodextrans in hydrogels and in deuterium oxide were measured at 23 °C in NMR sample tubes of 5 mm diameter. Dextran concentrations depended on the dextran's molecular weight and varied from 3.0 M for the 3 kDa dextran to 0.3 M for the 40 kDa dextran to avoid agglomeration in solution. We performed several diffusion measurements with each sample, varying the key parameters δ and Δ_N. Our experience showed that this is a good practice which helps identifying artifacts affecting the experiments or errors in the processing routines. The diffusion delays, Δ_N, were chosen between 0.1 and 2.0 s and the gradient pulse widths, δ, were between 600 and 1400 μs.

Several combinations of Δ_N and δ were applied within those ranges. Later examination revealed high agreement among all those measurements, indicating good reproducibility.

2.2.3 Analysis Methods

2.2.3.1 Multiparameter Fluorescence Image Spectroscopy (MFIS)

The recorded MFIS data can be correlated to yield correlation curves (Fluorescence Correlation Spectroscopy, FCS, is part of the MFIS). Those fluorescence correlation curves that were measured inside the hydrogel usually exhibited multiple overlapping bunching terms in the time regime of the diffusion process. To establish the number of independent species, *M*, needed in the model function to reproduce the data, we fitted a distribution of diffusion coefficients applying the maximum entropy method (MEMFCS).[92] Having determined *M* we then fitted a model function containing *M* diffusion terms (eq. (2.4)):

$$G(t_c) = 1 + \frac{1}{N}\sum_{i=1}^{M} x_i \left(\left(1 + \frac{t_c}{t_{d,i}} \right) \sqrt{1 + \frac{t_c}{(z_0/\omega_0)^2 \cdot t_{d,i}}} \right)^{-1} \left(1 - A_T + A_T \cdot e^{-\frac{t_c}{t_T}} \right) \quad \text{with} \quad \sum_{i=1}^{M} x_i = 1 \qquad (2.4)$$

For species with identical brightness, x_i represents their true molecular fractions. In this case, *N* is the number of molecules in the singlet state in the detection volume element and t_c is the correlation time. The model assumes a three-dimensional Gaussian-shaped volume element with spatial distribution of the detection probabilities $w(x,y,z) = \exp(-2(x^2+y^2)/\omega_0^2)\exp(-2z^2/z_0^2)$. The $1/e^2$ radii in *x* and *y* or in *z* direction are denoted by ω_0 or z_0, respectively. The characteristic diffusion time is $t_d = \omega_0^2/4D$, with the translational diffusion coefficient *D*. The confocal detection volume, V_{det} is calculated as follows: $V_{det} = \pi^{3/2} z_0 \omega_0^2$.

Basic photophysical processes such as triplet transitions which result in temporary dark states are accounted for by an additional bunching term. Here A_T and t_T represent the triplet population and the triplet relaxation time.

The correlation curves for A488- and TMR-dextrans in water and most FLU-dextrans in carbonate buffer were fitted pixel by pixel, the remaining samples image-integrated. At mean irradiances in the focus of 1.2 kW/cm^2, A488- and TMR-samples did not exhibit noticeable triplet populations (A_T < 0.01), only fluorescein showed fluorescence bunching in the µs regime at even lower irradiances of 0.4 kW/cm^2. For pixelwise analysis, error bars for t_d (and

equivalently for D) were calculated as standard error of the mean while for single point (i.e. solution) or image integrated measurements a bootstrapping procedure was applied.

Diffusion coefficients can be derived from the extracted diffusion times (t_d) provided that the size and shape of the confocal detection volume element are characterized. In practice, a photostable reference dye with known diffusion properties is used to calibrate the system. In the present case, we chose Rhodamine 110 (Rh110). Thus all presented diffusion coefficients derived from FCS are based on the reported value of $D_{Rh110}=(4.3\pm0.3)\times10^{-6}$ cm^2s^{-1} at 295.65 K in dilute aqueous solutions.[93] The characteristic diffusion time of Rh110 in deionized water was t_d=30 µs with day-to-day variations of less than 5 %. Due to increased aberrations with changes in the refractive index upon addition of salt, a systematic increase of t_d was observed (e.g. t_d=33 µs for Rh110 in 20 mM potassium carbonate buffer at pH 7 and pH 10, respectively). The longer wavelength required for the TMR experiments caused an increase in focus area $\pi\omega_0^2 = t_d 4\pi D$ and thus of t_d of about 30 %, as expected from the changed diffraction limit.

A variety of possible artifacts have been reported that could cause uncertainties in translational diffusion measurements by FCS.[94] In particular optical saturation effects are known to distort the detection volume element and thus alter the observed average dwell times of the fluorophores. These effects have been minimized by keeping the excitation power low and by performing reference measurements under identical conditions. Low excitation power also diminishes the probability of photobleaching. Successful minimization of this effect is confirmed by the observation of extremely slow diffusing molecules with dwell times of up to 1 s.

A further possible artifact, focal distortions due to a refractive index mismatch (below 0.01, see S1.6) is estimated to result in a small corresponding error in D (below 1 %[95]).This is supported by the good agreement of the FCS data with the independent MTI and NMR results (see below). Additionally, the possible refractive index mismatch between solution and hydrogel was checked using FCS and found to be negligible. No readjustment of the correction collar setting on the objective was required after switching the sample from pure water to hydrogel (see S1.6).

The steady state anisotropy, r, which is another parameter detected by MFIS is defined via the intensities of the fluorescence signal polarized parallel ($F_{\parallel}$) and perpendicular ($F_{\perp}$) with respect to the excitation polarization. As described by Koshioka et al.,[96] the fluorescence signal recorded with a confocal microscope is slightly depolarized by the objective due to its

high numerical aperture. To account for this experimental artifact, correction factors l_1 and l_2 have been introduced:[96]

$$r = \frac{GF_{//} - F_{\perp}}{(1-3l_2)GF_{//} + (2-3l_1)2F_{\perp}} \tag{2.5}$$

The correction factors l_1 and l_2 as well as the factor G, that compensates for the slightly different detection efficiencies of the two detection channels, were determined experimentally using the reference dyes Rhodamine 110 and TMR (l_1=0.0308, l_2=0.0368, G=0.99). In detail, the G-factor is defined as the ratio of the detection efficiencies between perpendicular and parallel polarized fluorescence light. The fluorescence signal F is obtained from the detected signal by subtracting the appropriate background (scattering) measured in clean water or an unloaded gel.

2.2.3.2 Macroscopic Transmission Imaging (MTI)

We found a linear relation between fluorescence intensity and concentration in the concentration range of 0.1 to 10 µM for all samples. Thus, we can directly determine the relative change in concentration from the image intensity. Especially for the larger dextran molecules, equilibration between the hydrogel and the surrounding solution takes several days. However, for most samples, it was found that measurement times of about 24 h were sufficient to allow diffusion coefficients to be extracted from the data. Some additional longer measurements were performed to capture the long time behavior. Even though the dyes used were relatively photostable and the incident intensity was reduced as much as possible, some photobleaching could be seen for these long measurement times. Thus, a photobleaching correction as described in[97, 98] was applied: The change in the normalized intensity F of an area in the solvent far outside the hydrogel, where no significant change in the concentration is expected, could be fitted with a double exponential function:

$$\frac{F(t)}{F(t=0)} = Pe^{-pt} + Qe^{-qt} \tag{2.6}$$

The intensity of the region of interest in the gel of every image was then corrected by dividing the original value by the one extracted from the bleach curve.

The hydrogel discs had a quasi-two-dimensional geometry and homogeneous radial diffusion was observed. Thus, by azimuthally averaging all pixels that are a certain distance away from the gel-reservoir interface, a concentration profile for every time step could be determined.

Comparison of the concentration profiles with diffusion equations, including appropriate boundary conditions, yields diffusion coefficients (see Sec. 2.3.2.1).

The hydrogels were fully swollen and in equilibrium before the measurements and no change in the hydrogel size was expected. However, for some samples we observed a decreasing gel radius of up to 6 % within the first hours of the experiments in the bright-field transmission images and the change in radius was taken into account in the analysis. The reason for this is not clear. A change in temperature or an expansion of the sample cell and with that a slight increase in sample thickness might play a role.[99]

2.2.3.3 Nuclear Magnetic Resonance (NMR)

As is usual practice, the diffusion coefficients D were obtained by fitting the echo amplitudes (integral of the signals between 2.8 and 4.4 ppm) to the following equation:[100, 101]

$$\frac{E_i}{E_0} = \exp\left[-D(\gamma g_i \delta)^2 (\Delta_N - \frac{\delta}{3} - \frac{\tau_N}{2})\right] \tag{2.7}$$

where E_i and E_0 are the echo intensities at increment i and with zero gradient applied, γ is the gyromagnetic ratio, g_i is the gradient amplitude at increment i, δ is the gradient pulse width, Δ_N is the diffusion delay and τ_N is the delay between the two magnetic field gradient pulses laying at one side of the echo pulse sequence. For the purpose of comparison, the diffusion coefficients measured in D_2O were recalculated for H_2O using the known viscosities of both solvents.[102]

2.2.4 Models for Brownian Dynamics Simulations

Brownian dynamics simulations were used to calculate the diffusion coefficients of dextran particles within the polymer network. Inspired by previous investigations,[73, 74] we considered simple models of effective spheres for the matrix particles and the dextrans. For this, we used a microscopic model resolving the matrix explicitly and coarse-graining the diffusing polymer coil as an effective soft sphere. There are further underlying model assumptions: i) the polymer matrix is not resolved on the monomer level, ii) the matrix structure is derived from a periodic structure, and iii) explicit hydrodynamic interactions caused by the solvent are ignored.

In order to obtain a systematic insight, the flexibility of the polymer matrix and the softness of the dextran-matrix interaction were modeled on three different levels. A schematic illustration of the models is shown in the results section (see Section 2.3.2.2, Figure 2.9). On the first level (also referred to as model 1 in the following), the matrix particles were fixed on

a periodic simple-cubic lattice with lattice constant *a* providing static steric obstacles for the diffusing dextran molecules. For simplicity, the latter were modeled as effective spheres. On this crude level any fluctuations in the pore sizes were neglected. The repulsive steric interaction between an obstacle *i* at position $\vec{s}_i$ and another particle *j* (either tracer or obstacle) at position $\vec{s}_j$, separated by the distance s_{ij}, was modeled as in ref.[74] with a truncated and shifted repulsive Lennard Jones potential (also known as WCA-potential):

$$U_s(s_{ij}) = 4\varepsilon_s\left[\left(\frac{\sigma_{ij}}{s_{ij}}\right)^{12} - \left(\frac{\sigma_{ij}}{s_{ij}}\right)^{6} + \frac{1}{4}\right] \tag{2.8}$$

where $\varepsilon_S = 1\ k_BT$ (~4.05×10^{-21} J at 20 °C) and the additive diameter $\sigma_{ij} = 2\ R_{obst}$ for the obstacle-obstacle-interaction and $\sigma_{ij} = R_{obst} + R_h$ for the interaction between a matrix obstacle and a tracer of radius R_h. The cutoff was set at the potential's minimum at $l_{ij} = 2^{1/6}\ \sigma_{ij}$.

For the second level (model 2), we introduced fluctuating matrix particles. The network connectivity was ensured by coupling neighboring matrix particles by harmonic springs. For the harmonic spring potentials, we used Hooke's law:

$$U_{sp}(s_{ij}) = 0.5k\left(s_{ij} - s_{0,ij}\right)^2 \tag{2.9}$$

for two matrix particles *i* and *j* with their distance at rest $s_{0,ij}$. Setting $k = 2\ k_BT/(2\ R_{h,D3})^2$ (~0.6 mJ/m^2) allowed the dextran D3 to push a gap of its own diameter 2 $R_{h,D3}$ through two neighboring matrix particles in rest positions when overcoming an energy of 1 k_BT. This parameter is kept fixed in all simulations. Moreover the matrix particles were exposed to thermal fluctuations and repelled each other and the dextran particles via steric interactions as in model 1 (eq. (2.8)). To broaden the pore size distribution, the matrix particles were randomly shifted up to half the lattice constant *a* in each direction with respect to their initial positions before attaching undistorted springs between neighboring matrix particles.

In a third level of modeling, two different extensions were tested by changing the dextran-matrix interactions. In model 3a, we replaced the WCA potential for the steric interactions with a softer effective Gaussian potential which is a good model for penetrating polymer coils of different architecture:[103-105]

$$U_G(s_{ij}) = \varepsilon_G \exp\left(-\frac{s^2_{ij}}{2b^2}\right) \tag{2.10}$$

with $b^2 = (R_i+R_j)^2/(2\ln(\varepsilon_G/(k_BT))$. This relation keeps the potential at $s_{ij} = R_i + R_j$ for $1\ k_BT$. We used $\varepsilon_G = 12\ k_BT$ (for more details see S11).

In model 3b, an attractive shell with the size of a typical fluorescent dye's radius (R_{D0}=0.55 nm) was added to the steric repulsion to account for a possible weak sticking of the dextrans to the matrix using a cosine function for a smooth transition:

$$U_{sp}(s_{ij}) = \begin{cases} 4\varepsilon_s\left[\left(\frac{\sigma_{ij}}{s_{ij}}\right)^{12} - \left(\frac{\sigma_{ij}}{s_{ij}}\right)^{6} + \frac{1}{4}\right] - \varepsilon_a & s_{ij} \le l_{ij} \\ -\frac{\varepsilon_a}{2}\left[\cos\left(\frac{\pi(s_{ij} - l_{ij})}{R_{D0}}\right) + 1\right] & l_{ij} < s_{ij} \le l_{ij} + R_{D0} \\ 0 & l_{ij} + R_{D0} \le s_{ij} \end{cases} \quad (2.11)$$

We obtained ε_a = 3.0 ± 0.3 $k_B T$ as fitted value in both investigated systems. This value seems reasonable as it should cause a significant slowdown of the dextrans' motion while still allowing a thermal escape out of the shells.

By tracking the tracer's trajectories, the mean square displacements can be calculated as:

$$\Delta s^2(t) = \left\langle \left(\vec{s}(t_0 + t) - \vec{s}(t_0)\right)^2 \right\rangle \quad (2.12)$$

For a given sufficiently large elapsed time t, the long-time diffusion coefficients could then be extracted as:[106, 107]

$$D = \lim_{t\to\infty} \frac{1}{6}\frac{\mathrm{d}}{\mathrm{dt}} \Delta s^2(t) \quad (2.13)$$

such that the hindrance factors are D/D_0.

For a given value of a, which sets the mean pore size, the hindrance factors for all tracer particles were calculated and this set of simulation data was compared to the experimental data. An optimal value for a was found by the best fit, using a as the single fitting parameter. Only in model 3b, ε_a was used as a second fitting parameter. For more technical details, see S11.

2.3 Results and Discussion

The different experimental techniques used here allowed us to estimate the precision of the measurements in different ways. In MTI and NMR, the experiments are conducted by averaging over one gel, calculating therefore the dispersion of the data between different gels. In MFIS we are able to detect two kinds of dispersion of the data: (i) we measured different spots within the same gel (pixelwise analysis) and (ii) we executed measurements between different gels (different data points in Figure 2.12 b).

It is known that the hydrogels in practice always exhibit an inhomogeneous cross-link density distribution, called spatial heterogeneity.[108, 109] The scattering of experimental data from various independent measurements, beyond the shot noise limits of the single measurements, indicates the heterogeneity in the gel structure. Spatial heterogeneity on the macroscopic scale is detected by pixelwise analysis. Different locations within the same gel display slightly different results. These feature were visible in all MFIS studies reported below.

2.3.1 Several populations of guest molecules detected by MFIS

FCS

In contrast to the single diffusion times observed in solution, for most of the gel samples we have observed that up to three independent diffusion times are needed to fit the FCS curves. Differently diffusing species, extending from free molecules just hindered by the limiting pore size (t_d ~410 µs) up to temporarily trapped particles (t_d > 10 ms) were found (SI 2-SI 4). Figure 2.1a displays a set of image-integrated correlation curves for A488-D10 at different electrolyte conditions which reveal the decreasing fraction of slowly diffusing temporarily trapped particles for increasing salt concentration. Temporary sticking and accumulation of the probe molecules in the hydrogel are indicated by time trace analysis (Figure 2.4a). Such tracer-hydrogel interactions already have been studied in the past, showing different effects depending on the chemical structure of the gel, the solvent and the nature of the tracer. [41, 45, 47] Interestingly, Vagias and coworkers[41] also found interactions between the hydrogel and different tracers when employing FCS. Although they used another hydrogel than in our study, the different fluorescence intensity between gel and solution is clearly shown by them.

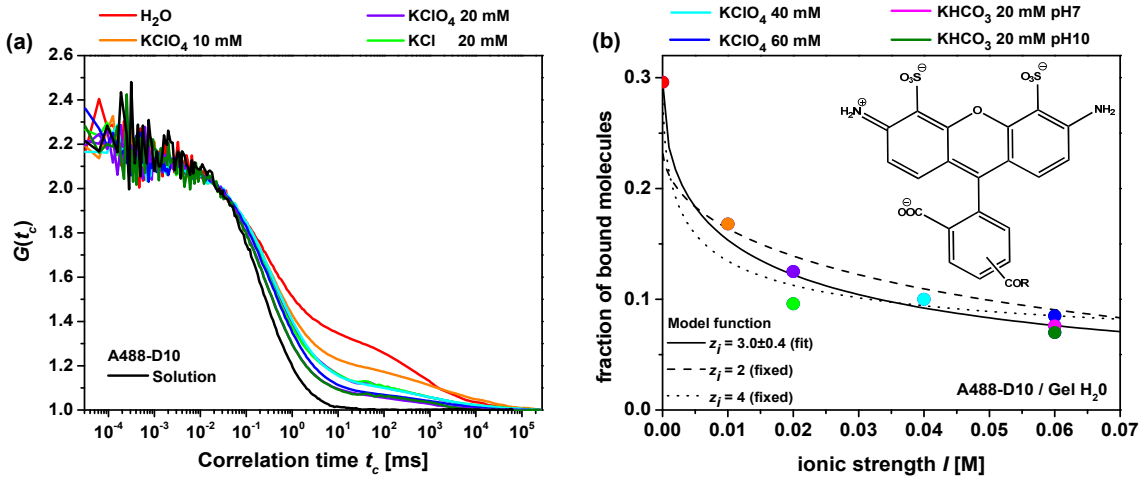

Figure 2.1. (a) Image-integrated normalized correlation curves for A488-D10 in hydrogels at different salt conditions, (b) decreasing fraction of slow, temporarily bound molecules for

A488-D10 in the hydrogel with increasing ionic strength I (right panel). A fit of eq. (2.14) yields Z_i=3.0±0.4; K_d'=0.42±0.03; R_i=(0.7±0.5) nm. The inset shows one possible mesomeric structure and charge distribution of Alexa488.

A simple binding model was applied to describe the observed equilibrium fractions of mobile and trapped probe molecules (x_{bound}), where f_{free} is the activity coefficient for free molecules and K'_d the effective binding constant (see S1.7):

$$x_{bound} = \frac{f_{free} K'_d}{1 + f_{free} K'_d} \tag{2.14a}$$

It was assumed that the activity of the freely diffusing (mobile) species is most affected by the ionic strength of the solvent. The Debye-Hückel equation[110] describes the dependency of the activity coefficient, f_{free} , on the charge, Z_i, the effective radius of the ion, R_i, and the ionic strength, I, in the limit of low salt concentrations:

$$f_{free} = 10^{-\frac{AZ_i^2\sqrt{I}}{1+BR_i\sqrt{I}}} \tag{2.14b}$$

with tabulated values[110] for the constants A=0.507 $mol^{-1/2}dm^{3/2}$ and B=3.28 $nm^{-1}mol^{-1/2}dm^{3/2}$ for aqueous solution at 22.5 °C. A combination of eqs. (14a) and (14b) can be fit to the equilibrium fraction of trapped molecules as a function of the ionic strength. The fit shown in Figure 2.1b yields Z_i≈3, which is in good agreement with the estimated mean number of charges per labelled dextran, estimated as follows. D10 samples have ~5 labelling sites per molecule. The specified mean degree of labelling (DoL_{av}) of the investigated A488-D10 samples is 1, if the unlabelled dextran molecules are also considered. However, considering only labelled dextrans in a first approximation of random labelling, we can expect around 1.5 dyes per labelled and thus detected dextran (for more details of this calculation, see S1.3), which corresponds to a mean charge Z_i(A488-D10) ≈ 3. For the higher salt concentrations, the Debye length κ^{-1} is of the order of the macromolecule's dimension (κ^{-1}≈1.4 nm for I=0.05 M), producing conditions beyond some of the approximations made to derive eq. (2.14b). Nevertheless, the fit shown in Figure 2.1b describes the experimental data sufficiently well.

The analysis reveals that mainly the presence or screening of charges determine the sticking behavior of the probe molecules and not the kind of anion as suggested by the Hofmeister series.[111, 112] In particular, perchlorate, chloride or hydrogen carbonate ions at the same ionic strength had a comparable influence on the diffusion properties of the studied samples (see Figure 2.1b).

Fluorescence anisotropy

To compare the restricted motion of A488-D10, TMR-D10 and FLU-D10 in the hydrogel to its behavior in solution, we performed measurements of steady state anisotropy r and time resolved anisotropy $r(t)$ for each pixel. For this, a possible distribution of r due to the heterogeneous environment needed to be separated from shot-noise broadening. Thus, a plot of r vs. number of detected photons, N_F, was analyzed (Figure 2.2a), and the mean anisotropy, $\langle r \rangle$ was calculated:[113]

$$r = \langle r \rangle \pm \frac{1}{3} \frac{(2 + \langle r \rangle)\sqrt{(1 - \langle r \rangle)(1 + 2\langle r \rangle)}}{\sqrt{N_F}} \tag{2.15}$$

It is clear that, on average, A488-D10 exhibits a higher anisotropy in the gel than in aqueous solution. This can be attributed to a temporary trapping of the solute in the matrix network. The plotted values for r in the gel are pixel-averages where about 30 % of molecules were trapped for this sample (Figure 2.1b). During the measurement time of 1800 s, many probe transits are averaged, so that the anisotropy reports on the average trapping probability. In our samples different pixels display different anisotropies, so that the width of the distribution significantly exceeds the shot-noise broadening as found in the solution measurement. This can only be explained by the spatial heterogeneity of the hydrogel.

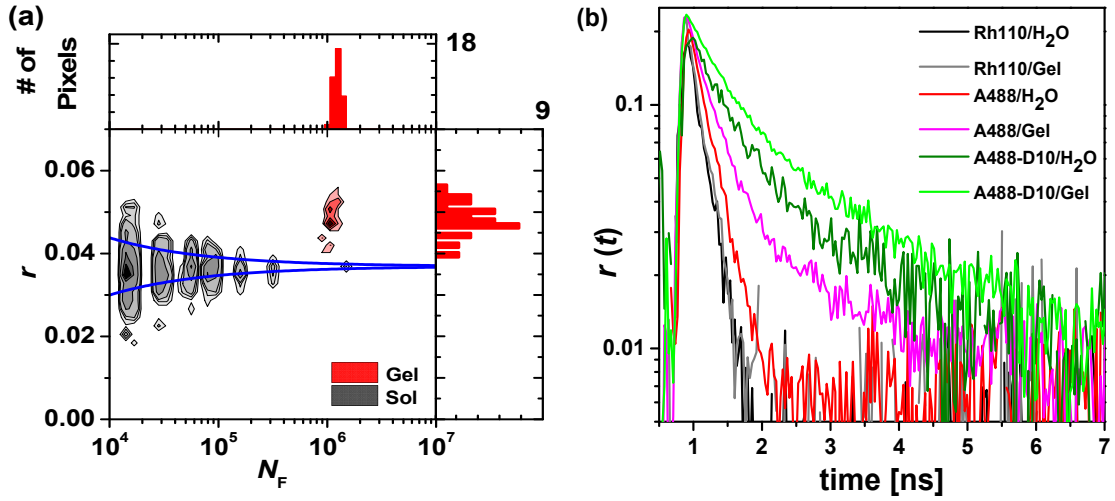

Figure 2.2. (a) Anisotropy r vs. photon number N_F in different time windows for A488-D10 in water (gray contour lines) and in hydrogel (red contour lines) with one-dimensional projections for the gel data. The time window for the gel data was 1800 s. The theoretical shot-noise limits of r is calculated with eq. (2.15) with $\langle r \rangle$=0.037 (blue lines). (b) Anisotropy decays, $r(t)$ for Rh110, A488 and A488-D10 in H_2O and Gel/H_2O.

To study probe-polymer interactions inside the gel matrix, r measurements where performed for A488-D10 under different conditions ($KClO_4$ 10 mM, 20 mM, 40 mM, 60 mM; KCl 20 mM; potassium carbonate buffer pH 7, 20 mM and pH 10, 20 mM, for TMR-D10 and FLU-D10 in H_2O, in potassium carbonate buffer 20 mM pH 10 and in TRIS buffer 50 mM pH 7.5). The 2D r-N_F plots for all conditions are shown in S7. Figure 2.3 shows the relation of the ratio of r in the hydrogel to r in different aqueous electrolyte solution and the fraction of trapped particles, x, which is directly calculated from FCS curves by applying eq. (2.4) (for values see Table S8).

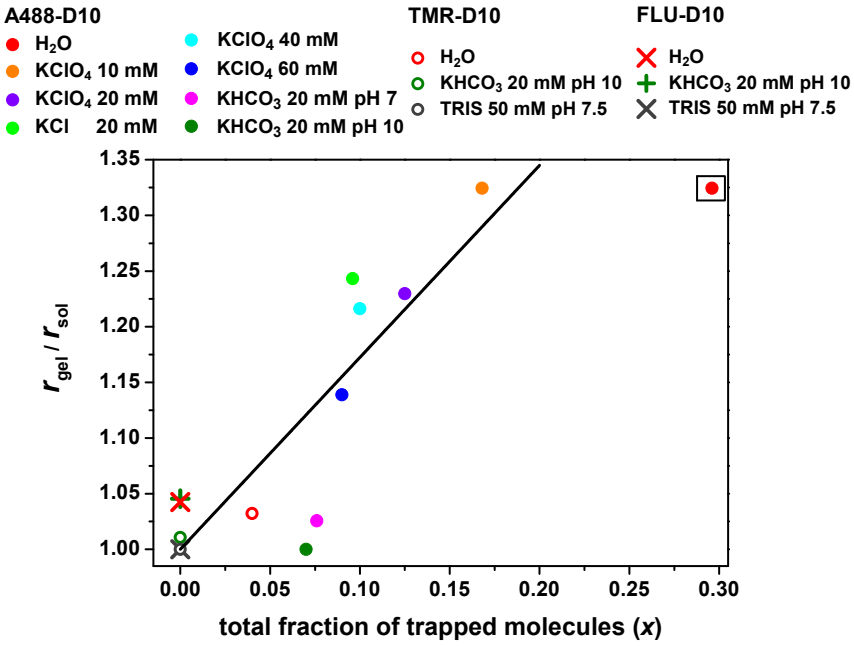

Figure 2.3. Average anisotropy ratio, r_{gel}/r_{sol} as a function of the fraction of trapped particles derived from FCS measurements for A488-D10 (see Figure 2.1), TMR-D10 and FLU-D10. Linear extrapolation (without H_2O value) yields r_{gel}/r_{sol}=2.7 ±0.3 for x=1.

In a two-component system the additive behavior of anisotropies predicts a linear dependence of r_{gel} on the fraction of the trapped species x: $r_{gel} = xr_{trapped} + (1\text{-}x)r_{sol}$. To take into account different initial solution anisotropies of the differently labeled probe molecules relative anisotropies r_{gel}/r_{sol} are plotted in Figure 2.3. By fitting a line to the data and using r_{sol}=0.037 (Figure 2.2) we estimate mean $r_{trapped}$ =0.10±0.01 for A488-D10. This is much less than the fundamental anisotropy of A488 (r_0=0.37) which would be expected for the completely immobilized dye. The low density of labels renders energy transfer between identical

chromophores an unlikely cause for the reduced anisotropy, leaving partial mobility of the dye even in the trapped environment as most probable explanation.

Fluorescence time traces

Time-traces of A488-D10 at low concentration in the hydrogel were investigated to further analyze the sticking behavior (Figure 2.4a). Temporary sticking and accumulation of the probe molecules in the hydrogel are indicated by relatively long dwell times (up to seconds) and count rates which are significantly above average, both of which are not observed for molecules freely diffusing in solution (Figure 2.4a). A strong correlation between the fraction of the trapped molecules is revealed by the slow decay between 10 ms and several seconds and the mean count rate for this time range in the corresponding fluorescence correlation curves (Figure 2.4b).

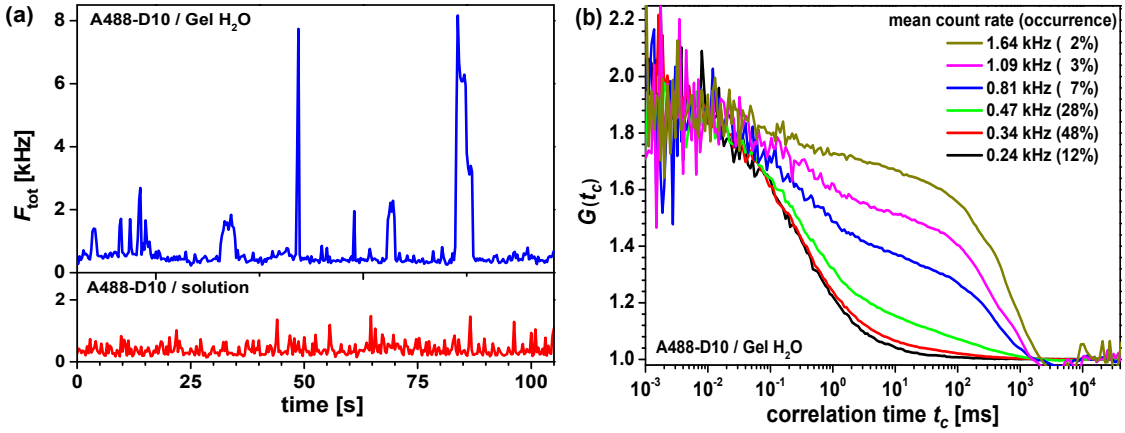

Figure 2.4. (a) Fluorescence time traces (sum of perpendicular and parallel channel) for a single pixel in the image of A488-D10 in solution and in the gel in water conditions, (b) correlation curves of count rate selected subsets of the trace (for details see S5).

The interaction of A488-D10 with the matrix is revealed by several different observations: first, a reduction of the fluorescence lifetime ($\tau_{gel}/\tau_{sol}\approx0.95$), mainly attributed to quenching since a change in radiative lifetime due to refractive index differences between gel and solvent is expected to only account for 1/3 of the effect ($\tau_{r(gel)}/\tau_{r(sol)}\approx0.987$, see S1.6)[114, 115], and, second, an increased anisotropy (r_{sol}=0.037, r_{gel}=0.049) with broadened distribution inside the gel (see Figures 2.2 and 2.3). Third, the apparent brightness B_{app} of A488-D10 in the hydrogel, obtained as the ratio of detected count rate to the apparent number of particles N (taken from the FCS amplitude, eq. (2.4)), is significantly lower than B measured in

solution ($B_{app}/B \approx 0.37$) which is not consistent with the weak dynamic quenching indicated by the small change in fluorescence lifetime. One possible explanation could be that the fluorescence of the molecules trapped on a longer time scale (>1 min) is statically quenched which results in a virtually uncorrelated background reducing the correlation amplitude. Taking static quenching into account for the highly interacting A488-D10, an effective concentration of trapping sites in the range from 10 to 50 nM can be deduced for low salt conditions (detailed discussion in the S1.4 and S1.5). The observation of systematically higher fluorescence intensities inside the loaded gel than in the surrounding solution supports the idea of the enrichment of probe molecules in the gel (for details see S1.1 and S6).

2.3.2 Mobile guest molecules

2.3.2.1 Experimental Results

MFIS

As already discussed, the analysis of FCS correlation curves as displayed in Figure 2.2.1a revealed different populations of guest molecules with differing diffusion times. In this section, we only consider the freely diffusing species with the smallest diffusion time. With MFIS, the hydrogel was studied in deionized water as well as in 20 mM potassium carbonate buffer at pH 10. Significantly different results were found for the two experimental conditions. These differences can be explained by a solvent dependent degree of swelling of the hydrogel (see sample details, Sec. 2.2.1.1). The diffusion coefficients from FCS experiments are shown in Table 2.3.

sample	dye [a]	M_w [b] [kDa]	R_h [c] [nm]	$D_{sol.}$ [10^{-6}cm^{2}s^{-1}]	D_{gel} [10^{-6}cm^{2}s^{-1}]
free dye	A488	0.53	0.56	3.69±0.05	2.7±0.1
	TMR	0.39	0.56	3.45±0.07	2.6±0.1
	FLU	0.33	0.54	4.33±0.09	3.9±0.1
D3	A488	3	1.7±0.1	1.05±0.02	0.59±0.02
	TMR			1.13±0.02	0.62±0.02
	FLU			1.45±0.03	1.24±0.04
D10	A488	10	3.1±0.2	0.64±0.01	0.32±0.02
	TMR			0.99±0.02	0.47±0.02
	FLU			0.60±0.02	0.54±0.02
D40	TMR	40	6.0±0.3	0.38±0.01	0.10±0.01

	FLU			0.32±0.01	0.18±0.03
D70	TMR	70	7.9±0.4	0.33±0.01	0.083±0.004
D500	FLU	500	20±2	0.107±0.002	0.04±0.02
D2000	TMR	2000	40±4	0.068±0.002	-
	FLU			0.060±0.001	-

Table 2.3. Diffusion coefficients of free dye and dextran conjugates in solution, D_{sol}, and in the hydrogel, D_{gel}, at 22.5 °C. [a] A488 and TMR samples measured in deionized water, FLU in 20 mM potassium carbonate buffer at pH10; [b] molecular mass M_w as obtained from manufacturer; [c] hydrodynamic radii R_h for free dyes are calculated from reported diffusion coefficients via Stokes-Einstein equation.[116-119] R_h of dextran conjugates are obtained from a fitted Flory scaling law to our MFIS and NMR data (see Figure 2.8). Errors for D_{sol} and D_{gel} are standard errors of the averages from multiple measurements, errors for R_h are 68% confidence intervals (±1σ) from the fit.

MTI

Figure 2.5a shows an example set of fluorescence images at the beginning and the end of an MTI experiment of A488-D10 diffusing into a hydrogel disc. Due to the influx of fluorescent particles into the polymer hydrogel, the fluorescent intensity inside the hydrogel increases with time. A higher intensity inside the hydrogel is clearly visible at the end of the measurement. This indicates enhanced fluorescence of the dyes inside the gel and/or an attraction of the dye to the hydrogel. As expected, a variation of the particle concentration between 0.1 μM and 10 μM did not change the diffusion coefficient.

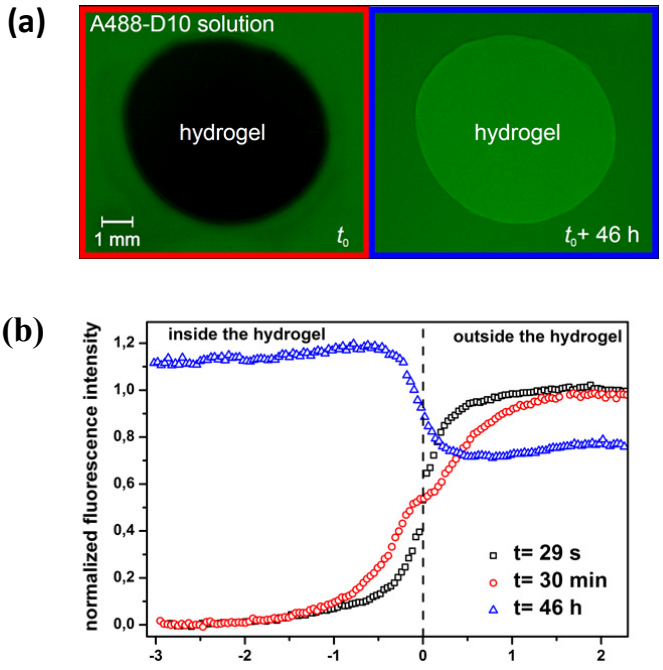

Figure 2.5. (a) Example fluorescence images at the beginning (t_0) and the end of an experiment, (b) intensity-distance profiles for 29 s, 30 min and 46 h after contacting a cylindrical polymer hydrogel with A488-D10 solution.

In these experiments the two faces of the hydrogel discs were not accessible to the solvent. Thus, the samples can be described as infinitely long cylinders in a reservoir of dye or dextran in solution, i.e. a quasi two-dimensional geometry with radial diffusion. Assuming azimuthally homogeneous diffusion, for every fluorescence image, the azimuthally averaged intensity profiles were determined. Typical intensity-distance profiles for three times are displayed in Figure 2.5b. The 46h data illustrate that the fluorescence intensity in the gel is higher than in solution.

Diffusion equations for radial diffusion in an infinite cylinder with radius R_d suspended in an infinite reservoir with a diffusion coefficient D_{gel} yield a radial concentration profile $c(s,t)$ of the diffusing substance with the radial position s inside the infinite cylinder:[120]

$$c(s,t) = c_\infty + \left(\frac{c_i - c_\infty}{2D_{gel}t}\right) e^{-\frac{s^2}{4D_{gel}t}} \int_0^{R_d} e^{-\frac{s'^2}{4D_{gel}t}} I_0\left(\frac{ss'}{2D_{gel}t}\right) s'ds' \qquad (2.16)$$

with the modified Bessel function of the first kind of order zero, I_0, and the initial and final concentrations c_i and c_∞, respectively

Analysis of the complete concentration profiles is nontrivial because if the hydrogel edge is not perfectly perpendicular, this can lead to scattering and edge effects which will influence the shape of the measured concentration profiles. We thus first considered a more robust approach and analyzed the temporal increase in concentration in the center of the hydrogel. To enhance statistics, we averaged over an area of 0.2 mm by 0.2 mm in the center of the hydrogel. This area is small compared to the overall size of the gel ($R_d \approx 3.5$ mm). One typical dataset for the increase of A488-D10 in the center of a cylindrical hydrogel is shown in Figure 2.6.

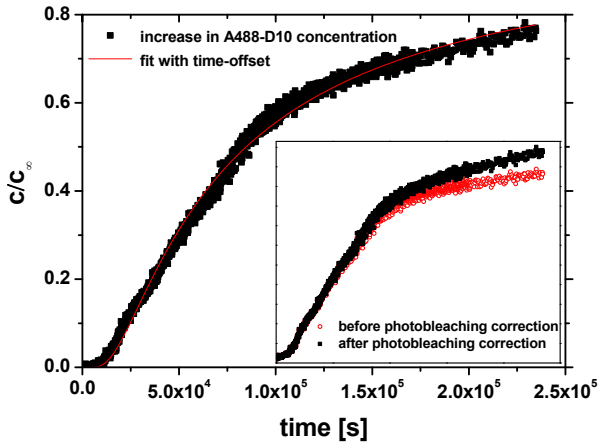

Figure 2.6. Increase in A488-D10 concentration in the center of a hydrogel disc with time. The inset shows the original data (open circles) and the data after a photobleaching correction has been applied (closed squares).

From eq. (2.16) an expression for $s = 0$ was derived:[120]

$$c(t) = c_i + (c_\infty - c_i)e^{-\frac{R_d^2}{4D_{gel}(t+t_0)}} \tag{2.17}$$

An imperfectly perpendicular hydrogel edge and potential scattering from the gel edge will lead to a broadened start profile (Figure 2.5). This was accounted for by adding a time-offset t_0 in eq. (2.17). This equation was fitted to the time evolution of the intensity in the center of the hydrogel. This resulted in very good agreement with the data (see Figure 2.6).As the gel radius plays an important role in the determination of D_{gel}, we fitted all datasets with both the initial and the final radius (given in section 2.2.3.2) and estimated D_{gel} to be between the values we get from these fits (Table 2.4).

sample	dye	D_{gel} [$10^{-6}cm^2s^{-1}$]
free dye	A488	3.2±0.1
D3	A488	0.73±0.02
D10	A488	0.42±0.01

Table 2.4. Diffusion coefficients of A488 free dye and dextran conjugates in the hydrogel at 23°C measured by MTI. Errors for D_{gel} are standard errors of the averages from multiple measurements.

Since the reservoir in the experiments was finite, the above model does not perfectly describe the experimental conditions. In the experiments, the volume of the solution surrounding the gel was about 11 times the cylinder volume. This should result in a homogeneous final dye concentration $c_\infty \approx 0.92\ c_i$ in both the gel and reservoir. This has not been observed (Figure 2.5). Thus we considered a second model; diffusion into a cylinder from a stirred solution of limited volume.[120] The fitting results from this model were compared to those from the above model (eq. (2.16)). The second model was found to describe the data for short and intermediate measurement times, but failed to describe the long time behavior. The model suggests that saturation between cylinder and reservoir should be achieved much faster than seen in the experiments. This discrepancy could be due to an attractive interaction between the hydrogel and the diffusing molecules as indicated by the MFIS experiments. In line with this idea is the observation that for all measurements with Alexa-labelled particles, the fluorescence intensity of the hydrogel was higher than that of the surrounding solution at the end of the measurement (Figure 2.5). If the particles are attracted to the hydrogel, they will preferentially diffuse into the gel even after the concentration difference between gel and reservoir is balanced. This corresponds to a larger effective reservoir as described by eq. (2.16), which is based on an infinite reservoir.

NMR

Diffusion coefficients of unlabelled dextrans in D_2O and inside the hydrogel were extracted from the NMR measurements using eq. (2.7) to fit the echo amplitudes. For D40 in the hydrogel, one typical decay curve and the corresponding fit using eq. (2.7) is shown in Figure 2.7 (for more details See S10) .

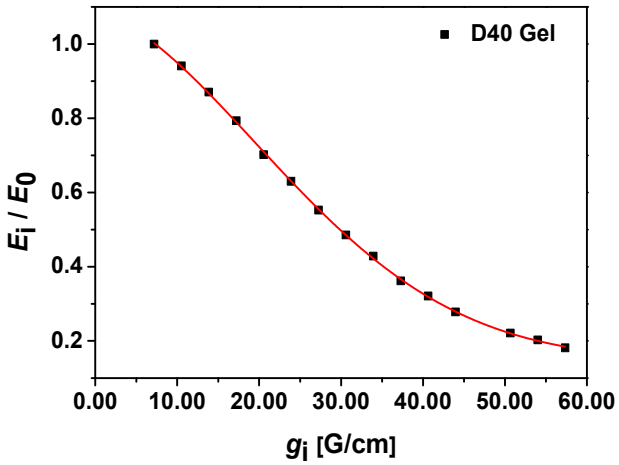

Figure 2.7. NMR data and fit using eq. (2.7) for unlabelled dextrans (40 kDa) in the hydrogel. The data was normalized.

Very good agreement between experimental data and the fit can be observed. The resulting diffusion coefficients (average of three measurements with varying gradient length) are shown in Table 2.5.

sample	dye	R_h [a] [nm]	D_{sol} [10^{-6}cm^{2}s^{-1}]	D_{gel} [10^{-6}cm^{2}s^{-1}]
D3	unl.	1.7±0.1	1.37±0.01	0.80±0.01
D10	unl.	3.1±0.2	1.158±0.003	0.38±0.01
D40	unl.	6.0±0.3	0.451±0.003	0.110±0.003

Table 2.5. Diffusion coefficients of unlabelled dextran in solution, D_{sol}, and in the hydrogel, D_{gel}, at 23 °C measured by NMR. [a] hydrodynamic radii R_h from D_{sol} (free dye) or fitted power law (dextran conjugates, from experimental data, see Table 2.3). Errors for D_{sol} and D_{gel} are standard errors of the averages from multiple measurements, errors for R_h are 68 % confidence intervals (±1σ) from the fit.

Summary

Although all applied techniques probe different length scales of the sample, for the same conditions they yield remarkably consistent diffusion coefficients, which are displayed in Figure 2.8. Fits to the Flory scaling law were used to determine the hydrodynamic radii R_h (also see S9) of the dextrans in solution. As expected, the diffusion coefficients of all our guest molecules decay markedly with increasing molecular weight and the results for all methods agree quantitatively. The heterogeneity in the gel structure is indicated by the scatter

of the gel data around the fit curve from various independent measurements beyond the shot noise limit.

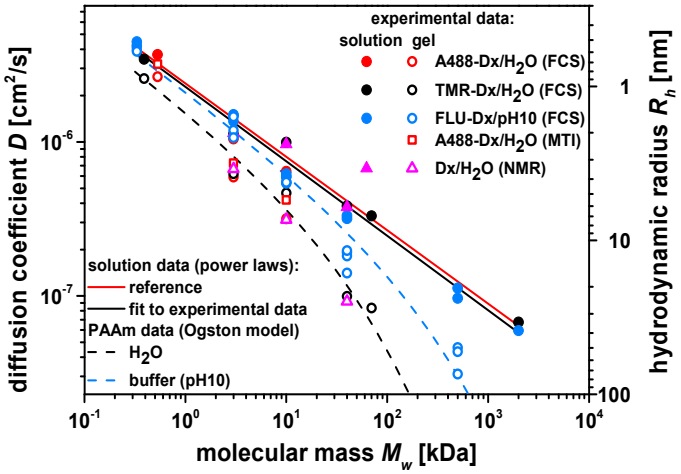

Figure 2.8. Experimental diffusion coefficients D at 22.5 °C and (for solution data) hydrodynamic radii R_h for equivalent spheres as estimated by the Stokes-Einstein equation. Solution data (filled symbols) were approximated by the Flory scaling law (red line, R_h[nm]=(1.01±0.07) × (M_w[kDa])$^{0.48±0.02}$, and compared to reference data (black line, R_h[nm]=(0.96±0.13) × (M_w[kDa])$^{0.48±0.04}$, see SI 9).[116, 121, 122] Dashed lines represent fits of the Ogston model (black: H_2O, blue: buffered solution at pH 10; for parameters see Table 2.6) to the gel data (open symbols).

2.3.2.2 Comparison with Ogston theory

Besides adsorption or temporary binding phenomena, the hindrance of diffusion, i.e. a reduction of the macroscopic diffusion coefficient inside the matrix with respect to the bulk diffusion coefficient is a fundamental property characterizing the transport behavior of particles within the matrix. Diffusion of solutes inside the pores has been approximated by many models.[123-125] Here we applied a simple fiber network theory. This model goes back to Ogston et al.[62] and describes a hydrogel as a network of randomly distributed fibers. Based on this model, the hindrance factor is

$$H = \exp\left(-\sqrt{\varphi\left(1+\frac{R_h}{R_f}\right)^2}\right) \tag{2.18}$$

where R_f is the radius and φ the volume fraction of the fibers in the gel and R_h the hydrodynamic radius of the diffusing species.

The important assumptions behind this model are known: i) the solute/fiber interaction is purely hard-sphere in nature, ii) the fibers are infinitely long and were placed randomly in the matrix, and iii) the solute concentration is very low, so that solute-solute interactions are negligible in both phases. It is clear that such approach can only be a crude approximation of the real physical effects that are governing the translocation in the matrix in our system. Nevertheless, Ogston's model yields a convenient and simple analytic expression to analyze fundamental trends. Moreover, such approach implies the use of effective parameters, permitting in terms of the volume fraction (φ), to obtain reasonable results in comparison to the experimental values as estimated from analysis of the swelling behavior (See Sec 2.1.1).
As expected and shown in Figure 2.8, the diffusion coefficient D decreases with dextran size, with the decrease being more pronounced in the gel. Thus, the hindrance factor, $H=D_{gel}/D_{sol}$, will also decrease with increasing hydrodynamic radius R_h of the dextrans (see Figure 2.12).
Dashed lines in Figure 2.8 represent the curves calculated with the Ogston model (eq. (2.18)) using the fit parameters listed in Table 2.6. The agreement with our data is already very good. Using newer, comparable models (such as the Amsden-model[123]) did not noticeably improve agreement with our data (thus not shown in Figure 2.8).

		TMR-Dx / H_2O	FLU-Dx / pH 10
	φ (exp.)	0.0390±0.0004	0.0150±0.0001
fiber network model (eq. (2.18))	φ	0.06 ± 0.03	0.005 ± 0.007
	R_f [nm]	1.4 ± 0.5	1.3 ± 1.1

Table 2.6. Results from fitted model function with standard errors and the experimentally determined polymer volume fraction (φ) in the swollen hydrogel

2.3.2.3 Comparison with Brownian Dynamics simulations

While the Ogston model provides a simple analytical formula to describe the trends for the dextran dynamics with an effective excluded volume, we now apply our Brownian dynamics simulations (see Sec. 2.2.4) for a more detailed modeling approach. Different approaches to model a hydrogel have been used in previous works. When investigating the swelling behavior of a gel, Linse and coworkers[63-66] and Holm and coworkers[67-69] resolved the individual monomers of the gel network. However the dynamics of tracer particles through the network was not performed within this level of modelling. Addressing tracer motion within monomer-resolved modelling requires much more computational resources in particular for long-time diffusion. Also the fitting procedure would require several sets of runs. Therefore we leave monomer resolved studies to future work. Instead we decided to

follow the more coarse-grained approach by Zhou and Chen.[74] This type of modeling provides a simple and systematic framework in which to include different physical effects, namely the mobility of the matrix particles (i.e. fluctuations in the matrix structure), the effective dextran-matrix excluded volume, and sticky attractions. The matrix-dextran interactions are expected to play a key role in spreading the delay times of the diffusive process of the dextran molecules through the matrix. Figure 2.9 shows schematic two-dimensional representations of the three-dimensional simulations on the three different levels that were used to explain the experimental data.

In qualitative terms, one would expect increasing agreement between the simulation and experimental data as we increase the level of complexity. This is indeed what is observed and displayed in Figure 2.10, where the different simulation results are compared to FCS data. In model 1, hard matrix particles are fixed on simple cubic lattice sites, providing a uniform matrix with just one pore size. This results in a very sharp drop in the hindrance factor when the dextran's size is increased to this pore size. Introducing elastically connected matrix particles (model 2) broadens the pore size distribution and leads to a slower decrease of the hindrance factors with dextran size, as expected. However, this decrease is still too sharp compared to the experimental data. Softening the interactions by changing the interaction potentials from WCA to a Gaussian potential (model 3a) shows an even lower, yet still too distinct decrease, of the hindrance factor with increasing dextran size. The agreement is still unsatisfactory. Especially the hindrance of the smaller dextrans is too weak in the previous approaches. When these small dextrans collide with matrix particles, they can easily find another way to pass due to their small size.

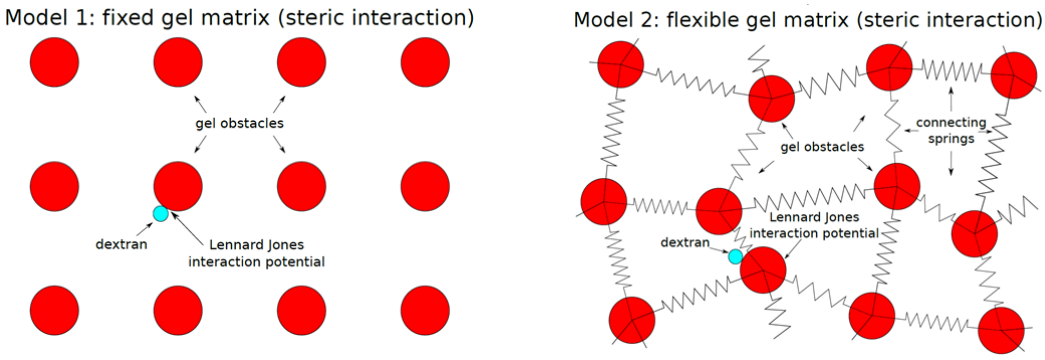

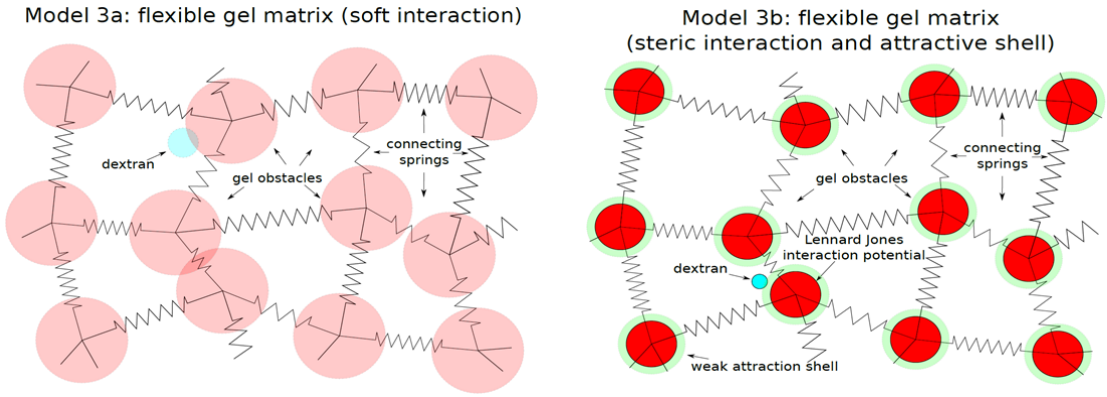

Figure 2.9. Four models for the dextran-matrix. model 1: fixed gel matrix (steric interaction, eq. (2.8)), model 2: flexible gel matrix (steric interaction, eq. (2.8)), model 3a: flexible gel matrix (soft interaction, eq. (2.10)) and model 3b: flexible gel matrix (steric interaction and attractive shell, eq. (2.11)). The sketches illustrate two-dimensional representations of the three-dimensional models used for the simulations.

The introduction of an attractive contribution in the matrix-guest interaction (model 3b) is found to be crucial to describe the observed slow decay with increasing dextran sizes. If the smaller dextrans collide with a matrix particles in this model, they can still find another path to pass. However, they are more likely to first become stuck resulting in a slowdown even for small dextrans.

Model 3b is the only one which includes a repulsive interaction and an attractive shell and it is the best representation of our experimental data. Additional simulations performed within model 3b using a Gaussian softened core showed a similar fit quality as that with a WCA-core. The results show that, within the framework of the model classes considered here, an effective attraction is needed to describe the spreading of the dynamics correctly given the statistical uncertainties of the experimental data. The origin of this attraction still needs to be resolved. For specific simulation parameters see the Table S11.

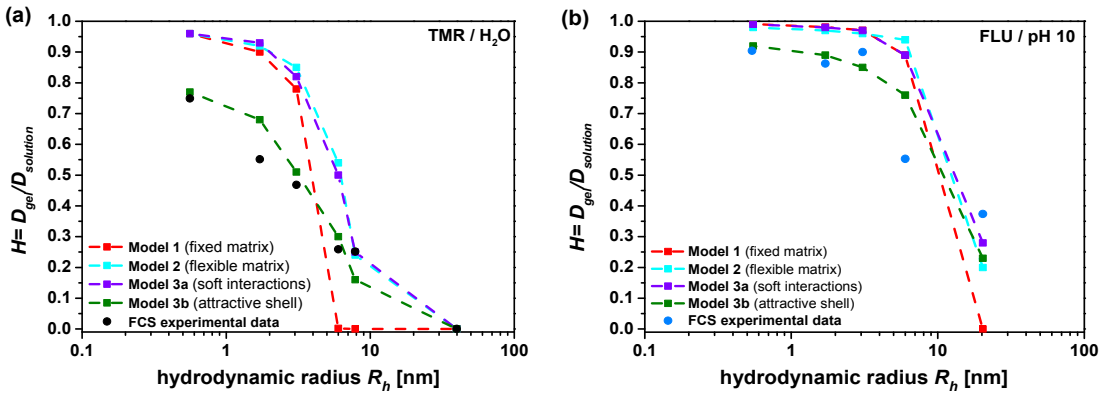

Figure 2.10. Comparison between FCS experimental data and Brownian dynamic simulations with 4 different models for TMR-Dextran in water conditions (a) and FLU-Dextran in 20 mM potassium carbonate buffer at pH 10 (b).

2.3.3 Estimation of the average pore size

The theoretical study permits an estimation of the average pore size of the investigated hydrogel in the two experimental environments. We optimized for the a priori unknown average pore size by fitting the simulated hindrance factors to the experimental data. Since the positions of all matrix particles in the BD-simulation are known, one can estimate the size of a specific pore in the gel as the center-to-center distance of two neighboring matrix-particles minus the matrix-particle-diameter. The decision which matrix particle pairs have to be counted as 'neighbors', is subject to a certain degree of arbitrariness. We chose to consider all particle pairs that are connected with springs, therefore possibly overestimating the correct value by neglecting close, but unconnected, matrix particle-pairs. Figure 2.11 shows this distribution for both investigated conditions calculated using model 3b.

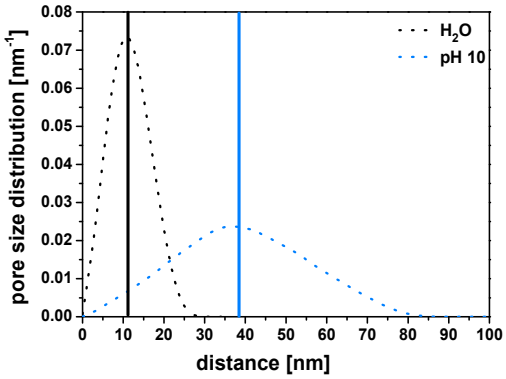

Figure 2.11. The distribution of the free space between connected matrix particles (dots) in the BD simulation and the average pore size (bars) of the polymer matrix in both experimental conditions. It is based on the final set of parameters after the fit within the applied model 3b. Black dots correspond to H_2O, blue dots to 20 mM potassium carbonate buffer at pH 10(for details see text).

We obtained an average value of 11±1 nm for gels in water and 38±3 nm for gels in buffer at pH 10 for the final set of parameters after the fit. While this average pore size is an output from fitting the simulated hindrance factors to the experimental data, the shape of the distribution is rather an input as the width of this distribution (standard deviation σ = 5 nm for water, σ = 16 nm for pH 10 in Figure 2.11) scales with the average value as defined in the models. The average values are in the same order of magnitude as calculated from swelling experiments, where we estimated 5.7 nm and 7.8 nm, respectively, assuming ideal solvent

quality, homogeneous cross-linking densities and Gaussian distribution of chain lengths (see Sec. 2.2.1.1). In H_2O both results differ by less than a factor of 2.

We now compare the results of our gel ([*T*]=0.04 g/ml, C_R=0.035), obtained in water conditions, with literature values for gels with similar composition. Significant discrepancy between pore size values resulting from scanning electron microscopy SEM (10-20 μm)[52-54] and swelling analysis (2.0 nm) was reported.[53] When using SEM, the structure of the gel may become damaged during the freeze-drying processes, resulting in systematically too large pore sizes. In our study, we measured under native conditions without disturbing the gel matrix structure thus circumventing this problem.

In gel electrophoresis with DNA as a cylindrical tracer molecule,[43, 48, 51] pore sizes between 5.9 and 133 nm are reported for gels with similar composition to ours. The hydrodynamic radius of the DNA was not measured directly but calculated using different models which is known to be an intrinsic problem. Approximating DNA by a sphere becomes more reasonable for shorter DNA molecules. Therefore it is notable, that the electrophoresis study using the shortest DNA[51] matches our result the best.

Very early work of polyacrylamide gels, using electrophoresis of proteins[50] in phosphate buffer, pH 7 ([*T*]=0.06 g/ml, C_R=0.05) and chromatography of proteins[49] in water ([*T*]=0.065 g/ml, C_R=0.02) agree well with our results, yielding 8.5 nm and 2.25 nm, respectively. In addition, recent studies[122] based on dynamic light scattering revealed mesh sizes of the same order of magnitude for polyacrylamide hydrogels of about 15 nm and for poly(N-isopropylacrylamide) of about 19 nm.

2.4 Combined results and conclusions

All data for the hindrance factor *H* obtained from the three different and independent methods we have applied are displayed and compared to Brownian dynamics simulations performed with model 3b in Figure 2.12. For the MTI measurements, the average values of D_{sol} from NMR and MFIS were used to scale the data, as they could not be measured with this technique.

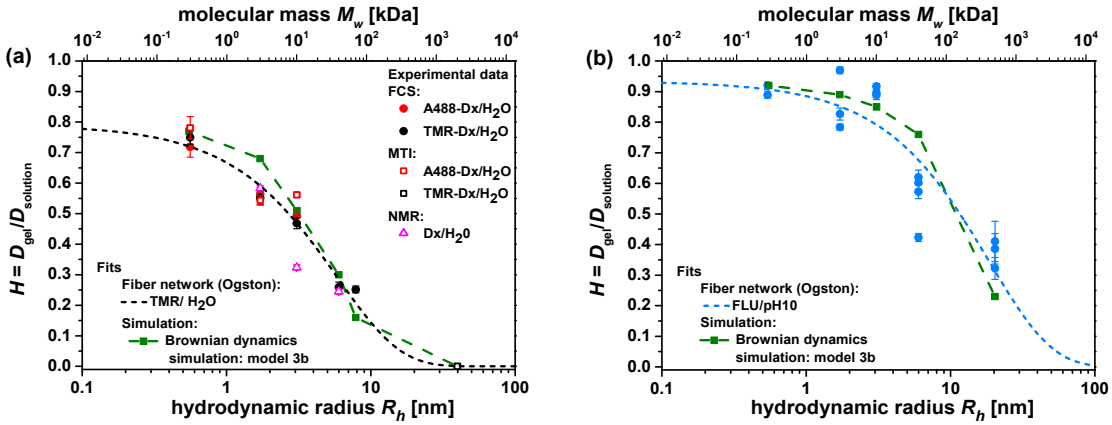

Figure 2.12. Hindrance factors $H=D_{gel}/D_{sol}$ of dextrans in hydrogel. A488 (red), TMR (black) and unlabelled samples (magenta) measured in deionized water (a), FLU labelled samples (blue) measured in 20 mM potassium carbonate buffer at pH 10 (b). Experimental data: FCS (filled circles); MTI (open squares); NMR (open triangles); fitted model function: fiber network (eq. (2.18), dashed black and blue lines, parameters table 2.6) and Brownian dynamics simulation (green points). The errors are the standard errors of repeat measurements.

We have shown that the long time diffusion coefficients of dextran molecules moving in solution and in a polyacrylamide gel matrix determined on different length scales by using multiparameter fluorescence image spectroscopy (MFIS), macroscopic transmission imaging (MTI) and nuclear magnetic resonance (NMR) are consistent. The measured diffusion coefficients decrease with increasing molecular weight and fall on a master curve. This supports the reliability of our data set, which might thus serve as possible calibration data for future experiments and theories.

In addition, although our results could be described by the Ogston model (Figure 2.12), a more realistic flexible model of the gel matrix was applied to describe the experimental data and to estimate the average pore size in the gel. The simulated average pore sizes of 11 nm (water) and 38 nm (pH10) agree reasonably well with estimations from swelling theory of 5.7 nm and 7.8 nm, respectively. Within the experimental error bars and the limitations of the applied models, our results for the gel equilibrated in water are in good agreement with published studies employing comparable globular macromolecular probes (2.25 nm[49] or 8.5 nm[50]) as well as with light scattering investigations (15 nm)[122] in native gels with similar composition.

Combining experiments and simulations enabled us to achieve a better understanding of the effects determining the diffusion of molecules in the gel network. Moreover, using the MFIS

method, a significant interaction between hydrogel and macromolecules was observed, in particular for A488 samples. The MTI results support the idea of the attractive interaction of Alexa-labelled particles and the gel, showing that the fluorescence intensity in the hydrogel was higher than that of the surrounding solution at the end of the measurements. This suggests to use uncharged dyes or, in case of charged dyes, to add a sufficiently high salt concentration for future investigations.

The heterogeneity inside a single hydrogel sample was probed on a length scale of 10μm in anisotropy experiments by comparing different pixels and hence different positions in the hydrogel (Figure 2.2). Furthermore, for the experiments at pH10, the scattering of data from various independent samples in Figure 2.12b was significantly beyond shot noise limits (or other experimental uncertainties), revealing a heterogeneity, which persisted over the complete measurement times.[108, 109]

Despite our application of a wide range of methods and the general consistency of the results we have obtained, open questions remain. For example, while the hindrance factor in the limit of small tracer particle sizes tends to 1 in our FLU/pH 10 system, it seems to approach ~0.8 in our TMR/H_2O system (Figure 2.12). A value close to 1 might still be approached for smaller tracer particles in our H_2O system, but we could not investigate these in our study due to experimental limitations. If one assumes that there really is a difference for smaller tracer molecules, the question whether this is due to different swelling in different environments or caused by different interactions of the matrix with different dyes cannot be answered with certainty yet.

For future studies, the diffusion of the same dextran molecules with the same dyes in differently crosslinked matrices should be explored systematically in order to distinguish between different modes governing the translocation.

2.5 List of abbreviations as appearing in the text

Definition	Symbols
Mass concentration of polymeric material in total volume	$[T]$
Weight fraction of cross-linker with respect to the total mass of the polymeric material	C_R
Diffusion time	t_d
Gel disk radius	R_d
Volume dry polymer	V_p
Volume gel after swelling	V_gel
Mass	m
Water density	ρ_H2O
Polymer density	ρ_p
Polymer volume fraction in the swollen state	φ
Molecular weight of the polymer between cross-links points	M_c
Molecular weight of the repeating units	M_r
Polymer mesh size	ξ
Cross-linking degree in the hydrogel	X
Carbon-Carbon bond length	ζ
Flory characteristic ratio	C_n
Numerical aperture	NA
Detection volume in MFIS	V_det
Temperature	T
Diffusion coefficient	D
Gradient pulse width	δ
Diffusion delay	Δ_N
FCS fit model function	$G(t_\mathrm{c})$
Triplet time	t_T
Triplet amplitude	A_T
Correlation time	t_c
Confocal volume radius in x and y	ω_0
Confocal volume radius in z	z_0
Detection probability	$w(x,y,z)$

Number of molecules	N
Molecular fraction	x_i
Position coordinates	x, y, z
Fluorescence intensity	$F,\ F_{//}\ ,\ F_{\perp}$
Polarization correction factors	l_1, l_2
Fluorescence anisotropy of species *i*	r_i
G-factor	G
Intensity fit parameters in MTI	P, p, Q, q
Echo intensities	E_i, E_0
Gyromagnetic ratio	γ
Gradient amplitude at increment i	g_i
Delay between pulses	τ_N
Boltzmann constant	k_B
Lattice constant	a
Distance in simulations models	$s_{i,j}$
Radius	R
Hydrodynamic radius	R_h
Matrix particle radius	R_{obst}
Position of particles in simulations models	$\vec{s}$
Mean square displacement	Δs^2
Time, reference time	$t,\ t_0$
Potential between *i* and *j* particles	$U_{i,j}$
Energy steric constant	ε_s
Energy Gaussian constant	ε_G
Energy attractive constant	ε_a
Constant in simulations models	b
Additive diameter	$\sigma_{i,j}$
Position of minimum in simulations models	$l_{i,j}$
Hindrance factor	H
Charge	Z_i
Effective binding constant	K_d'

Ionic strength	I
Effective ion radius	R_i
Activity	a_i
Concentration	c_i
Activity Coefficient	f_i
Debye-Hückel constants	A, B
Debye length	κ^{-1}
Photon Number	N_F
Fluorescence lifetime of species *i*	τ_i
Radiative lifetime of species *i*	$\tau_{r,\mathrm{i}}$
Bessel Function	I_0
Radial position inside an infinity cylinder for MTI fit	s, s'
Fiber radius	R_f

Acknowledgments

C.J., H.L., S.U.E., and C.A.M.S. gratefully acknowledge partial financial support from the Strategic Research Fund of the HHU.

Additional funding was given to D.W by BioSoft and to C.E.S. and H.L. by the ERC Advanced Grant INTERCOCOS (grant agreement 267499).

2.6 Supporting information

Materials and Methods

S1. *Dextran samples & hydrogel – fluorescence properties and quantitative FCS*

S1.1. *Manufacturers details of fluorescent samples*

Samples	Degree of labelling	Number of lysines	Number of amines[(a)]	Charge[(b)]	Absorption Max [nm]	Emission Max [nm]	Quantum yield[(c)]
A488-D3	1	0	≥ 1	a	495	517	0.6
A488-D10	1	10	≥ 2.5	a	494	516	0.6
FLU-D3	1	0	≥ 1	a	497	523	0.5
FLU-D10	2	0	≥ 2.5	a	496	521	0.5
FLU-D40	5	0	≥ 5	a	496	521	0.5
FLU-D500	86	58	≥ 50	a	496	521	0.2
TMR-D3	1	0	≥ 1	a	560	584	0.7
TMR-D10	3	0	≥ 2.5	n	559	586	0.5
TMR-D40	8	0	≥ 5	n	560	586	0.6
TMR-D70	10	0	≥ 10	n	560	585	1
TMR-D2000	138	456	not specified	not specified	560	583	0.8

Table S1. The table shows the manufacturers specification of dye-labelled dextran conjugates (data sheets of used sample batches, Invitrogen). [(a)] Specified for unlabelled aminodextrans. [(b)] a: anionic, n: neutral. [(c)] Fluorescence quantum yield Φ_F determined relative to fluorescein at pH 8.0 (FLU and A488; $\Phi_F^{\mathrm{FLU}} = 0.925 \pm 0.015$[126]) or relative to 5-(and-6)-carboxytetramethylrhodamine (TMR).

S1.2. *Investigation of partial quenching (quantum yield and fluorescence lifetime)*:

For the sample A488-D10 the partial quenching of the labels as indicated in table S1 was investigated applying time-correlated single photon counting (TCSPC, table S2).

fl. lifetime (species fraction)	τ_1 [ns] (x_1)	τ_2 [ns] (x_2)	τ_3 [ns] (x_3)	τ_4 [ns] (x_4)	τ_5 [ns] (x_5)	χ^2	τ_x [ns]
A488 / H_2O	4.125 (0.978)	0.459 (0.022)	/	/	/	1.13	4.045
A488-D10 / H_2O	4.125 (0.742)	2.459 (0.104)	0.932 (0.066)	0.260 (0.089)	/	1.30	3.400
A488-D10 / H_2O (corr.)	4.125 (0.548)	2.459 (0.077)	0.932 (0.049)	0.260 (0.065)	0 (0.262)	1.30	2.511

Table S2. Lifetime components of A488 and A488-D10 in H_2O (FT300, PicoQuant, Berlin; excitation: 485 nm, emission: 517-523 nm, magic angle, photons recorded: total 5×10^8, peak channel 10^6 photons, T=20 °C). τ_x: species averaged fluorescence lifetime.

While free A488 decays almost mono-exponentially its D10-conjugate exhibits at least four lifetime components, indicating dynamic quenching of a subset of the labels. Albeit, the obtained species averaged lifetimes, $\tau_x = \sum x_i \tau_i$, of conjugated and free dye are not consistent with the determined corresponding fluorescence quantum yields, Φ_F. According to the ratio of the quantum yields of the labelled dextran ($\Phi_F^{\text{A488-D10(exp)}} = 0.57$, measured versus Rhodamine 110, $\Phi_F^{\text{Rh110}} = 0.85$,[127] consistent with manufacturers information $\Phi_F^{\text{A488-D10(man)}} = 0.6\times0.925 = 0.56$) and the A488 dye free in aqueous solution ($\Phi_F^{\text{A488}} = 0.92$, Invitrogen online) a ratio of the species averaged fluorescence lifetimes of $\tau_x^{\text{A488-D10}} / \tau_x^{\text{A488}} \equiv \Phi_F^{\text{A488-D10}} / \Phi_F^{\text{A488}} = 0.57/0.92 = 0.62$ is expected. Thus a fraction of completely (statically) quenched labels of x_5 = 0.262 can be deduced (last row in table S2; $\tau_x^{\text{A488-D10,corr}} / \tau_x^{\text{A488}} = 2.511/4.045 = 0.62$). The resulting unquenched fraction then is $x_1^{\text{A488-D10}} / x_1^{\text{A488}} = 0.560$ and the remaining fraction of $1-0.560-0.262 = 0.179$ represents the partially (=dynamically) quenched dyes. For sake of simplicity, in the following the partially quenched fraction will be ignored and instead an effective totally quenched portion of x_q = 0.38 and a corresponding fluorescent portion of x_f = 1- x_q = 0.62 will be assumed.

S1.3. *The effective degree of labelling* ($DoL_{\text{eff.}}$):

The fluorescently labelled dextrans (as provided by Invitrogen, their specifications being summarized in table S1) are produced by exposing aminodextrans with an average number n_a of free amino groups to amine-reactive dye conjugates. Except for the A488 conjugates, once the dye has been added, the unreacted amines on the dextran are capped to yield a neutral or anionic dextran. Some of the samples carry additional lysines. Due to the applied labelling procedure, for any average degree of labelling, DoL_{av}, a distribution, $P(n_d)$, of the number of dyes per dextran molecule, n_{d}, is anticipated, i.e. even samples with a $DoL_{\text{av}} = 1$ will contain unlabelled as well as higher $(n_a \geq n_d > 1)$ labelled molecules. In case of random labelling, the distribution of n_{d} can be approximated by the binomial distribution:

$$P(n_d, n_a, DoL_{av}) = \frac{n_a!}{n_d!(n_a - n_d)!}\left(\frac{DoL_{av}}{n_a}\right)^{n_d}\left(1 - \frac{DoL_{av}}{n_a}\right)^{n_a - n_d} \qquad \text{(S1)}$$

For many labelled dextrans the fluorescence quantum yield is significantly reduced as compared to the free dye. Assuming only static quenching of the dyes (on the time scale of the experiment) three different distributions can be defined: (1) the distribution of dextrans $P(n_t)$ containing any number n_t of dyes (fluorescent or quenched) in the range of $n_a \geq n_t \geq 0$, (2) the distribution of dextrans $P(n_f)$ carrying n_f fluorescent (non-quenched) dyes, and (3) the distribution of dextrans containing any dye (fluorescent or quenched) under the condition that at least one fluorescent dye is present, $P(n_{t(f)})$. While $P(n_t) = P(n_d)$, $P(n_f)$ can easily be obtained from eq. S1 by replacing DoL_{av} with $DoL_{\text{av}} \times x_f$. The fluorescent fraction of the dyes x_f is approximated by the relative quantum yield of the labelled dextran as compared to the corresponding free dye, $x_f = \Phi_F^{\text{dextran}} / \Phi_F^{\text{free dye}}$ (see S1.2). The third distribution, $P(n_{t(f)})$, is obtained for $n_a \geq n_{t(f)} > 0$ from $P(n_t)$ by randomly distributing quenched dyes among the labelled dextrans, i.e. multiplying a second binomial distribution with $P(n_t)$ and adding the probabilities for all species with the same n_t that contain at least one fluorescent label. The unlabelled fraction is $P(n_{t(f)} = 0) = P(n_f = 0)$.

By omitting the corresponding unlabelled fractions ($n_t = 0$, $n_f = 0$ or $n_{t(f)} = 0$, respectively), three different effective degrees of labelling, DoL_{eff}^{x}, can be calculated from the obtained distributions using eq. S2:

$$DoL_{eff}^{x} = \sum_{n_x=1}^{n_a} n_x P(n_x) \Big/ \sum_{n_x=1}^{n_a} P(n_x) \qquad \text{(S2)}$$

with $x = t, f$ or $t(f)$, as defined above.

For A488-D10, the sample investigated in greatest detail in the current study, this will be shown in the following (table S3). For this sample DoL_{av} = 1 as determined by the manufacturer and x_f = 0.62 for the fluorescent fraction of the labels (see lifetime analysis S1.2) was assumed. Since the number of initial amino groups (n_a) per dextran could not be obtained from the manufacturer an average number of n_a=5 was estimated (being the mean $<n_a>$ for the currently available 18 batches of unlabelled aminodextrans D10 as specified on the manufacturers homepage). Choosing n_a=4 or n_a=6 does not significantly change the following considerations.

n_x	0	1	2	3	4	5	DoL_{eff}^{x}	x_f
$P(n_t)$	0.328	0.410	0.205	0.051	0.006	3×10^{-4}	1.49	1
$P(n_f)$	0.515	0.365	0.104	0.015	0.001	3×10^{-5}	1.28	0.62
$P(n_{t(f)})$	0.515	0.254	0.175	0.048	0.006	0.003	1.60	0.62

Table S3. Expected distribution of probabilities of labelled dextrans D10 ($P(n_t)$) assuming random labelling and a binomial distribution of the labels number, n_t, as well as corresponding distributions taking the fluorophores partial static quenching into account ($P(n_f)$ and $P(n_{t(f)})$. DoL_{av}=1, available labelling sites n_a=5. x_f is the fluorescent (non-quenched) fraction of the dyes. DoL_{eff}^{x} with $x = t, f, t(f)$ are the effective degrees of labelling considering all labels and labelled dextrans, only fluorescent labels and fluorescently labelled dextrans and all labels but only fluorescent dextrans, respectively.

The estimation of $DoL_{eff}^{(f)}$ assumed only static quenching for the partially quenched sample and thus presents a border case, but can be justified by the fact that, according to fluorescence lifetime analysis, the fraction of completely quenched dyes significantly exceeds the dynamically quenched portion (26% vs. 18%). The distribution of the total number of labels ($P(n_t)$ or $P(n_{t(f)})$) is relevant for the estimation of average ionic charges carried by the label. Here $P(n_{t(f)})$ yields the higher number of the two but might be an overestimation, since partial quenching of the individual fluorophores was excluded. Thus the true value of $DoL_{eff}^{(f)}$ as required to estimate the molecular charge due to labelling is expected to be in between the lower and upper limits as calculated via $P(n_t)$ and $P(n_{t(f)})$, respectively. The distribution of fluorescent labels, $P(n_f)$, has implications on the molecular brightness as observed by FCS as will be shown in S1.4.

S1.4. *Implications of the distribution of molecular brightnesses for quantitative FCS*:

In FCS the molecular brightness B is estimated by dividing the detected fluorescence count rate F by the observed number of fluorescent molecules, N_{tot}, simultaneously present in the confocal detection volume element, $B = F/N_{tot}$. In case of identical brightness of all particles N_{tot} can directly be obtained from the amplitude of the correlation function (eq. 2.4 main document, $N_{tot}=N$ for negligible triplet population). A distribution of brightnesses as discussed above would increase the observed amplitude, i.e. yielding an apparent (or effective) number of molecules N_{eff} (eq. S3).[128]

$$N_{eff} = N_{tot}\left(\sum_{n_f} n_f P(n_f)\right)^2 \Big/ \sum_{n_f} n_f^2 P(n_f) \qquad \text{(S3)}$$

Applying eq. S3 to the numbers in the table S3 yields $N_{eff}=0.856\ N_{tot}$. With $DoL_{eff,\,f.}=1.28$ an effective molecular brightness $B^{A488\text{-}D10}/B^{A488}=1.28/0.856=1.5$ is predicted and fully confirmed by experiment ($B^{A488\text{-}D10}\approx 6.8$ kHz/molecule, $B^{A488}\approx 4.5$ kHz/molecule; → $B^{A488\text{-}D10}/B^{A488}=1.5$). Ignoring the distribution of labels would falsify the determined molecular concentrations by almost 15 % and the corresponding brightnesses by 50 %. To derive the total number of dextran molecules, N_{dex}, in the confocal volume in addition the non-fluorescent labels portion needs to be considered ($P(n_f=0) = 0.515$, table SI 3): $N_{dex}=N_{eff}\cdot(0.856)^{-1}\times(1\text{-}0.515)^{-1}=2.41\cdot N_{eff}$. Comparing the concentrations of a series of A488-D10/H_2O solutions (not shown) as determined by FCS (confocal detection volume element $V_{det}=0.55$ fl) and its extinction (71,000 $cm^{-1}M^{-1}$ at 496 nm, Invitrogen) we find $N_{dex}(exp)=2.9\ N_{eff}$, consistent with the estimated number within the anticipated uncertainties of the confocal volume determination (±15 %), the measured quantum yield (± 10 %), the average degree of labelling (manufacturers specification) and the approximations made by calculating the dye distributions.

The experimental confirmation of the estimated effective brightness justifies the assumption made above of a random distribution of the quenched labels. An alternative scenario, e.g. quenching due to dye-dye interaction, might be indicated by the similarity of the estimated portion of the singly labelled dextrans ($P(n_t=1)=0.41$, corresponding to 61 % of the labelled molecules) and the fraction of unquenched dye as determined by TCSPC (56 %). This would lead to an expected effective molecular brightness of the dextran A488-D10 close to the free dye brightness and is not consistent with our FCS results.

S1.5. *Effect of immobile fluorophores on molecular brightness in FCS*:

In a stationary confocal measurement, i.e. keeping the location of the confocal volume fixed, the number of fluorophores that are immobile on the time scale of the experiment, N_{immob}, will not contribute to fluctuations of the fluorescence, provided temporary dark state population is negligible. In that case their fluorescence, F_{immob}, can be considered like uncorrelated background. This would reduce the correlation amplitude, $1/N_{\mathrm{mob}}$ (the inverse number of diffusing fluorescent particles) corresponding to the fluorescence, F_{mob}, of mobile fluorophores and yield an apparent amplitude, $1/N_{\mathrm{app}}$[128].

$$N_{mob} = N_{app}\left(\frac{F_{mob}}{F_{mob}+F_{immob}}\right)^2 = N_{app}\left(\frac{F_{mob}}{F_{tot}}\right)^2 \tag{S4}$$

$F_{\mathrm{tot}}=F_{\mathrm{mob}}+F_{\mathrm{immob}}$ is the total fluorescence, $N_{\mathrm{tot}}=N_{\mathrm{mob}}+N_{\mathrm{immob}}$ the total number of fluorescent particles. For brightness $B_{\mathrm{mob}}=B$ of mobile and $B_{\mathrm{immob}}=n_{\mathrm{i}}B$ of immobile particles follows (with $n_{\mathrm{i}}>0$):

$$N_{mob} = N_{app}\left(\frac{N_{mob}}{N_F}\right)^2 = N_{app}\left(\frac{N_{mob}}{N_{mob}+n_i N_{immob}}\right)^2 = N_{app}\left(\frac{N_{mob}}{n_i N_{tot}-(n_i-1)N_{mob}}\right)^2.$$

Here N_{F} is the equivalent total number of fluorophores with brightness B. With the apparent brightness $B_{app}=\frac{F_{tot}}{N_{app}}$ we get

$$B = \frac{F_{mob}}{N_{mob}} = \frac{F_{tot}}{n_i N_{tot}-(n_i-1)N_{mob}} = B_{app}\frac{N_{app}}{n_i N_{tot}-(n_i-1)N_{mob}} \quad \text{and}$$

$$\begin{aligned} N_{mob} &= N_{app}\left(\frac{B_{app}}{B}\right)^2 \\ n_i N_{tot}-(n_i-1)N_{mob} &= N_{app}\frac{B_{app}}{B} = \frac{F_{tot}}{B} \\ \Rightarrow \frac{n_i N_{tot}-(n_i-1)N_{mob}}{N_{mob}} &= \frac{B}{B_{app}} = \frac{n_i N_{tot}}{N_{mob}}-(n_i-1) \\ \Rightarrow x_{mob} = \frac{N_{mob}}{N_{tot}} &= n_i\left(\frac{B}{B_{app}}+n_i-1\right)^{-1} = 1-x_{immob} \end{aligned} \tag{S5}$$

Provided translational diffusion is the only process leading to fluorescence fluctuations, e.g. for $n_{\mathrm{i}}=1$ (identical brightness), the mobile fraction can easily be obtained from

$x_{mob}=N_{mob}/N_{tot}=B_{app}/B$. Thus the apparent change in molecular brightness as determined by stationary FCS can give information about the portion of mobile species otherwise invisible to this method.

For the samples studied, in particular the A488-D10, only a minor change in fluorescence lifetime due to quenching upon entering the hydrogel was observed ($\tau_{gel}/\tau_{sol}\approx0.97$, approximately half of the effect being caused by refractive index changes. See main document and S1.6), suggesting that the average molecular brightness in a first approximation can be considered as unaffected by the hydrogel. From FCS investigations of different concentrations of A488-D10/H_2O in the hydrogel between 30 and 100 nM we obtained an apparent molecular brightness of $B_{app}\approx2.5$ kHz/molecule. With $B\approx6.8$ kHz/molecule as measured free in solution a completely immobile fraction of $x_{immob}\approx0.63$ would have to be concluded from eq. S5. Since higher labelled molecules are preferentially trapped (see main document) this must be considered as an upper limit. In case all immobile particles were doubly labelled and the mobile ones would carry one fluorophore ($B_{mob}=B^{A488}=4.5$ kHz/molecule$=0.5B_{immob}$) an estimation according to the above analysis would yield $x_{mob}=2/((B/B_{app})+1)$ and $x_{immob}\approx0.29$. This is higher than the estimated fraction of A488-D10 with $n_f>1$ (12 %, table S3) and could indicate an enrichment of higher labelled dextrans inside the hydrogel, consistent with the observation of a higher binding constant for those probe molecules (main document).

S1.6. *Refractive index mismatch – effect on fluorescence lifetime and diffusion measurements*:

Inside the PAAm hydrogel the refractive index, n, is reported to be slightly higher than in dilute aqueous solutions.[114] For the densities of hydrogels and the wavelength used in our study a linear dependence of $dn/dc'=0.188$ ml/g can be extracted, with c' being the mass of PAAm per ml hydrogel. With $n_0=1.3361$ for water ($\lambda=525$ nm and T=22 °C)[129] and the measured densities of the gels (see main document, converted using a density of $\rho_{(PAA)}=1.3$ g/cm^3) we estimate the refractive indices in table S4.

Based on the refractive index, changes in radiative lifetimes, τ_r, can be calculated according to Toptygin by a modified Strickler-Berg approach.[115] The empty spherical cavity model (ESC, Toptygin, eq. S6) was found to successfully describe radiative lifetimes of small fluorophores in solution (eq. S1.5):

$$\frac{\tau_{r,2}}{\tau_{r,1}} = \left(\frac{n_1}{n_2}\right)^5 \left(\frac{2n_2^2+1}{2n_1^2+1}\right)^2 \tag{S6}$$

$\tau_{r,1}$ and n_1 are radiative lifetime and index of refraction in water, $\tau_{r,2}$ and n_2 the corresponding quantities in the gel (table S.4).

hydrogel	c [ml/ml]	c' [g/ml]	n	$\tau_{r(gel)}/\tau_{r(sol)}$
pH7	0.038	0.049	1.3454	0.987
ph10	0.015	0.020	1.3398	0.995

Table S4. Index of refraction at λ=525 nm and T=22 °C for PAAm hydrogels and its estimated effect on radiative lifetimes.

For A488 and A488-D10 the observed changes in fluorescence lifetimes are bigger than the predicted changes in radiative lifetime, suggesting additional fluorescence quenching due to matrix effects (see main document).

The relative small deviation of n from n_0 (H_2O) is well within the range of the correction collar of current water immersion objectives. This was shown for a Zeiss CApo40x/1.2 W objective,[130] comparable to our Olympus UPlanSApo 60x/1.2 W, and verified by experiment. Furthermore, in a calibration measurement we confirmed that for our conditions (wavelength, depth of the focal point in the sample) no readjustment of the correction collar setting was required after switching the sample from pure water to hydrogel.

S1.7. Binding model

A simple binding model was applied to describe the observed equilibrium fractions of mobile and trapped probe molecules:

$$\begin{aligned} K_d &= \frac{a_{bound}}{a_{free} \cdot a_{sites}} \\ K_d' &\approx K_d \cdot a_{sites} = \frac{a_{bound}}{a_{free}} \approx \frac{c_{bound}}{f_{free} c_{free}} \\ &\Rightarrow \frac{c_{bound}}{c_{free}} = f_{free} K_d' \\ &\Rightarrow \frac{c_{bound}}{c_{free} + c_{bound}} = x_{bound} = \frac{f_{free} K_d'}{1 + f_{free} K_d'} \end{aligned} \tag{S7}$$

Here, K_d is the binding constant, a the activity for free (a_{free}) and bound (a_{bound}) molecules with the respective concentration (c_{bound} and c_{free}). The number of binding sites in the matrix a_{sites} defines the effective binding constant K_d'.

Results

S2. *Image integrated normalized correlations curves measured in hydrogel for A488-Dx and TMR-Dx in water and for FLU-Dx in carbonate buffer 20 mM pH 10*

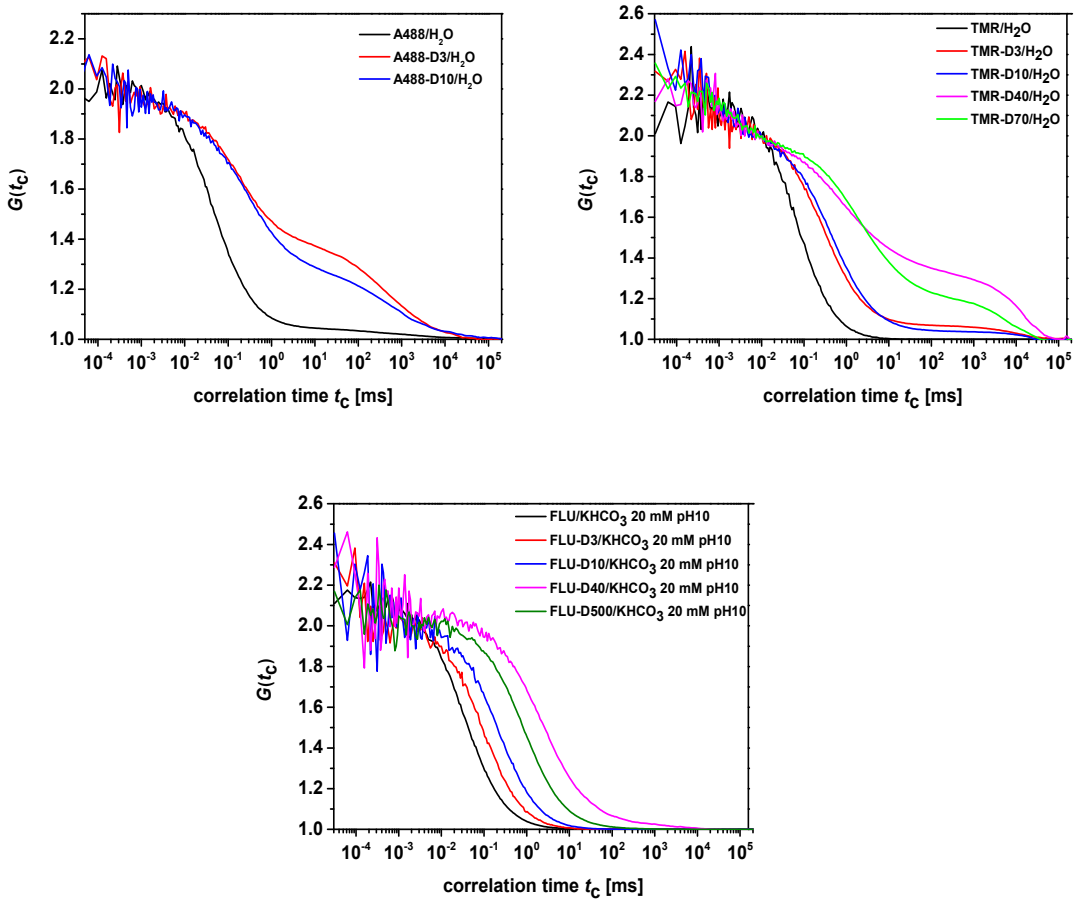

Figure S1. Image integrated normalized correlations curves for A488 and TMR free dye and with dextran in hydrogel in water conditions. In this case, more than one diffusion time is clearly visible, indicating the presence of temporarily trapped molecules in the hydrogel. FLU samples were measured in carbonate buffer 20 mM, pH 10, in this case the bound molecules are much less, only for samples D40 and D500 trapping is visible and amounts to about 1%.

S3. *Diffusion times from FCS experiments in the hydrogel at standard conditions*

Table S5 shows the diffusion times for A488, TMR and FLU for free dye and with dextran at standard conditions: water for A488 and TMR, carbonate buffer pH 10 for FLU in the hydrogel.

Dye	**Sample**	**Solvent**	**fast component**		**slow component**	
			t_d **[ms]**	**fraction x**	t_d **[ms]**	**fraction x**
A488	Free dye	H_2O	0.049 ± 0.002	0.991	200-500	0.009
A488	D3	H_2O	0.220 ± 0.007	0.626	10-2000	0.374
A488	D10	H_2O	0.410 ± 0.017	0.704	10-6000	0.296
TMR	Free dye	H_2O	0.065 ± 0.001	1	-	0
TMR	D3	H_2O	0.272 ± 0.010	0.873	10-8000	0.127
TMR	D10	H_2O	0.363 ± 0.011	0.962	1000-10000	0.038
TMR	D40	H_2O	1.699 ± 0.105	0.688	20-10000	0.312
TMR	D70	H_2O	2.026 ± 0.079	0.719	40-12000	0.281
FLU	Free dye	$KHCO_3$ 20 mM pH 10	0.036 ± 0.001	1	-	0
FLU	D3	$KHCO_3$ 20 mM pH 10	0.116 ± 0.001	1	-	0
FLU	D10	$KHCO_3$ 20 mM pH 10	0.263 ± 0.004	1	-	0
FLU	D40	$KHCO_3$ 20 mM pH 10	0.823 ± 0.032	0.992	10-140	0.008
FLU	D500	$KHCO_3$ 20 mM pH 10	3.664 ± 0.470	0.988	20-3000	0.012

Table S5. Results of FCS fits for A488, TMR and FLU (free dye and labelled dextran) in hydrogel. For some samples fitting the model function to the data required two or more diffusion times. In the latter case the fraction of the slow component (last column) is the sum of two terms that in total represent the fraction of trapped molecules. The diffusion times of fast components are the averages from different pixels. For the slow component, t_d is given as range because it significantly differs from pixel to pixel.

S4. *Diffusion times from FCS experiments for Rh110, A488, TMR and FLU free dye and labelled D10 at different salt conditions in the hydrogel.*

Sample	Solvent	fast component		slow component	
		t_d [ms]	fraction x	t_d [ms]	fraction x
Rh110	H_2O	0.036	1	-	0
A488	H_2O	0.049	0.991	200-500	0.009
A488-D10	H_2O	0.410	0.704	10-6000	0.296
A488-D10	$KClO_4$ 10 mM	0.384	0.832	10-6000	0.168
A488-D10	$KClO_4$ 20 mM	0.383	0.875	10-6000	0.125
A488-D10	KCl 20 mM	0.352	0.904	400-6000	0.096
A488-D10	$KClO_4$ 40 mM	0.401	0.900	10-6000	0.100
A488-D10	$KClO_4$ 60 mM	0.352	0.910	10-6000	0.090
A488-D10	$KHCO_3$ 20 mM pH 7	0.345	0.924	400-6000	0.076
A488-D10	$KHCO_3$ 20 mM pH 10	0.354	0.930	400-6000	0.070
TMR-D10	H_2O	0.363	0.960	500-7000	0.040
TMR-D10	$KHCO_3$ 20 mM pH 10	0.303	1	-	0
TMR-D10	TRIS 50 mM pH 7.5	0.212	1	-	0
FLU-D10	$KHCO_3$ 20 mM pH 10	0.265	1	-	0
FLU-D10	H_2O	0.260	1	-	0
FLU-D10	TRIS 50 mM pH 7.5	0.262	1	-	0

Table S6. Results of FCS fits for the reference Rh110, A488, A488-D10, TMR-D10 and FLU-D10 in solution and in the hydrogel at different salt conditions. For some samples fitting the model function to the data required two or more diffusion times. In the latter case the fraction of the slow component (last column) is the sum of two terms that in total represent the fraction of trapped molecules. The diffusion times of the fast components are the averages obtained from different pixels. For the slow component, t_d is given as range because it significantly differs from pixel to pixel.

S5. *Trace analysis*

The fluorescence time trace was split into small segments and sorted according to their approximated mean count rate employing a special feature of the binary single photon data format *.ht3 (PicoQuant, Berlin, Germany). Depending on the inter-photon time (i.e. the inverse count rate) in addition to the photon information extra entries are generated to store each overflow of the macroscopic time counter. Thus, sections containing the same total number of entries (as were generated upon splitting the recorded file) can be sorted by their content of photons and extra entries and thereby by their mean count rate. The produced subsets of split files were subsequently correlated and analyzed.

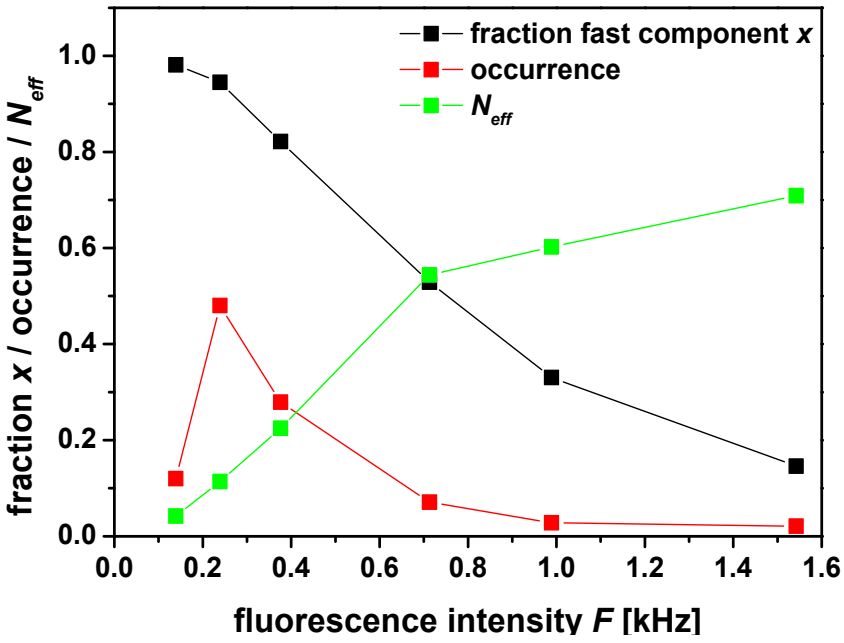

Figure S2. Fraction of fast component x, effective mean fluorophore number N_{eff} and occurrence of different count-rate based sections in time trace (Main document Figure 2.4). N_{eff} is the inverse correlation amplitude at τ_c=0 and corresponds to the total number of diffusing molecules in case of equal brightness for all components. Temporary accumulation of particles due to trapping is clearly visible.

S6. *Fluorescence intensity ratio between gel and the solution surrounding the gel plotted against experimental concentration for A488-D10 in H_2O from FCS measurements*

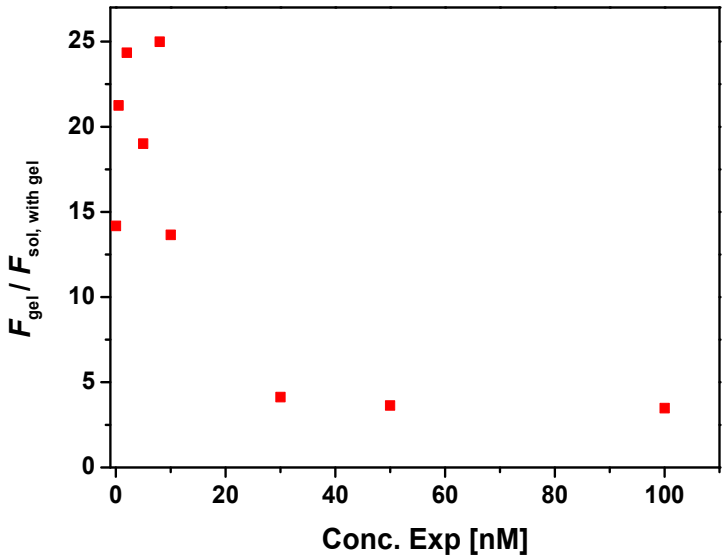

Figure S3. The plot shows that the fluorescence intensity ratio between gel and the solution surrounding the gel, F_{gel} / $F_{sol\ with\ gel}$, is decreasing with increasing experimental concentration. The enrichment of the fluorophores inside the gel, as indicated by the fluorescence intensity ratio is concentration dependent and strongest for small concentrations until high-affinity trap sites are saturated.

S7. *Fluorescence anisotropies of A488-D10, TMR-D10 and FLU-D10 in solution and hydrogel*

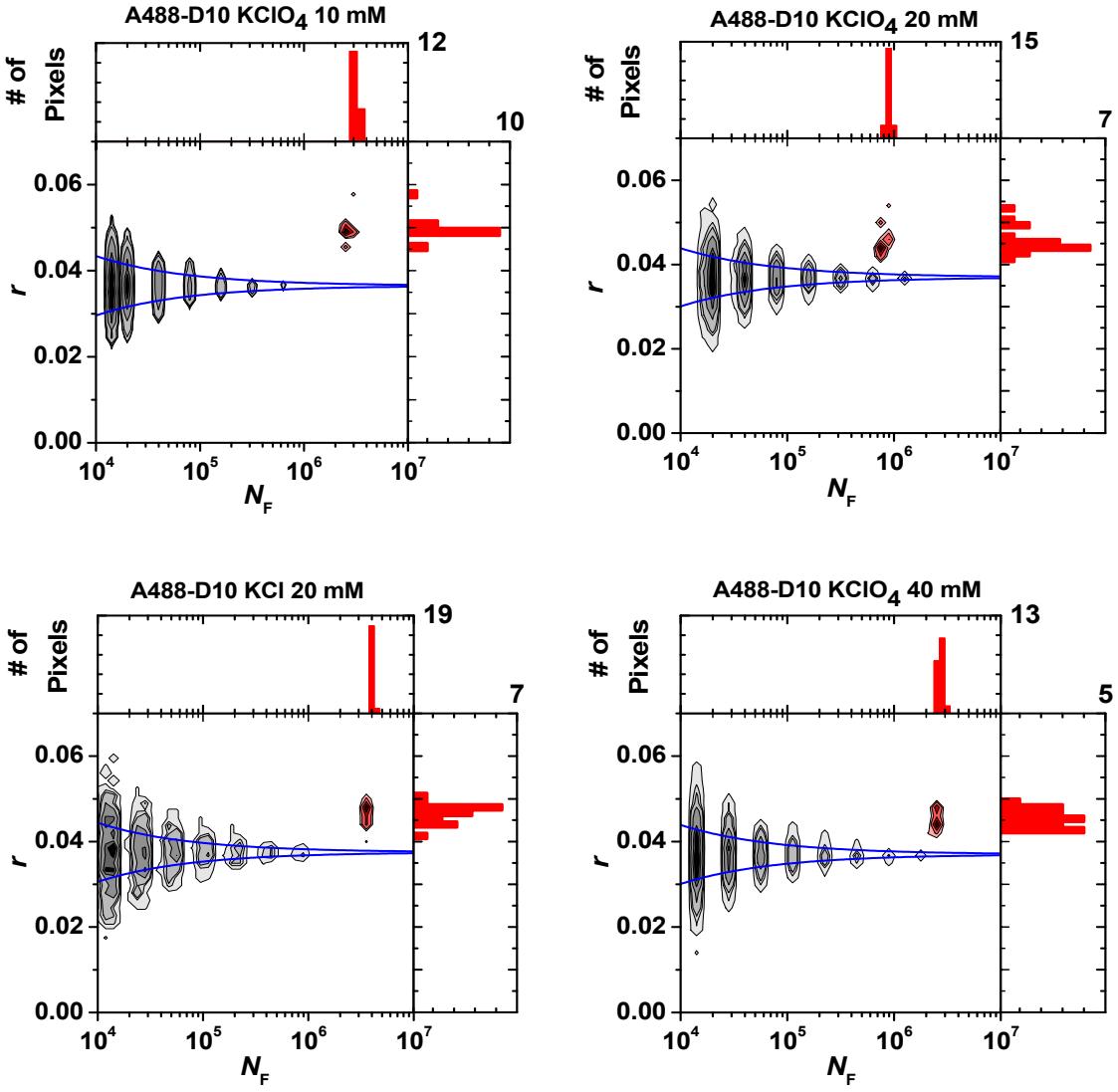

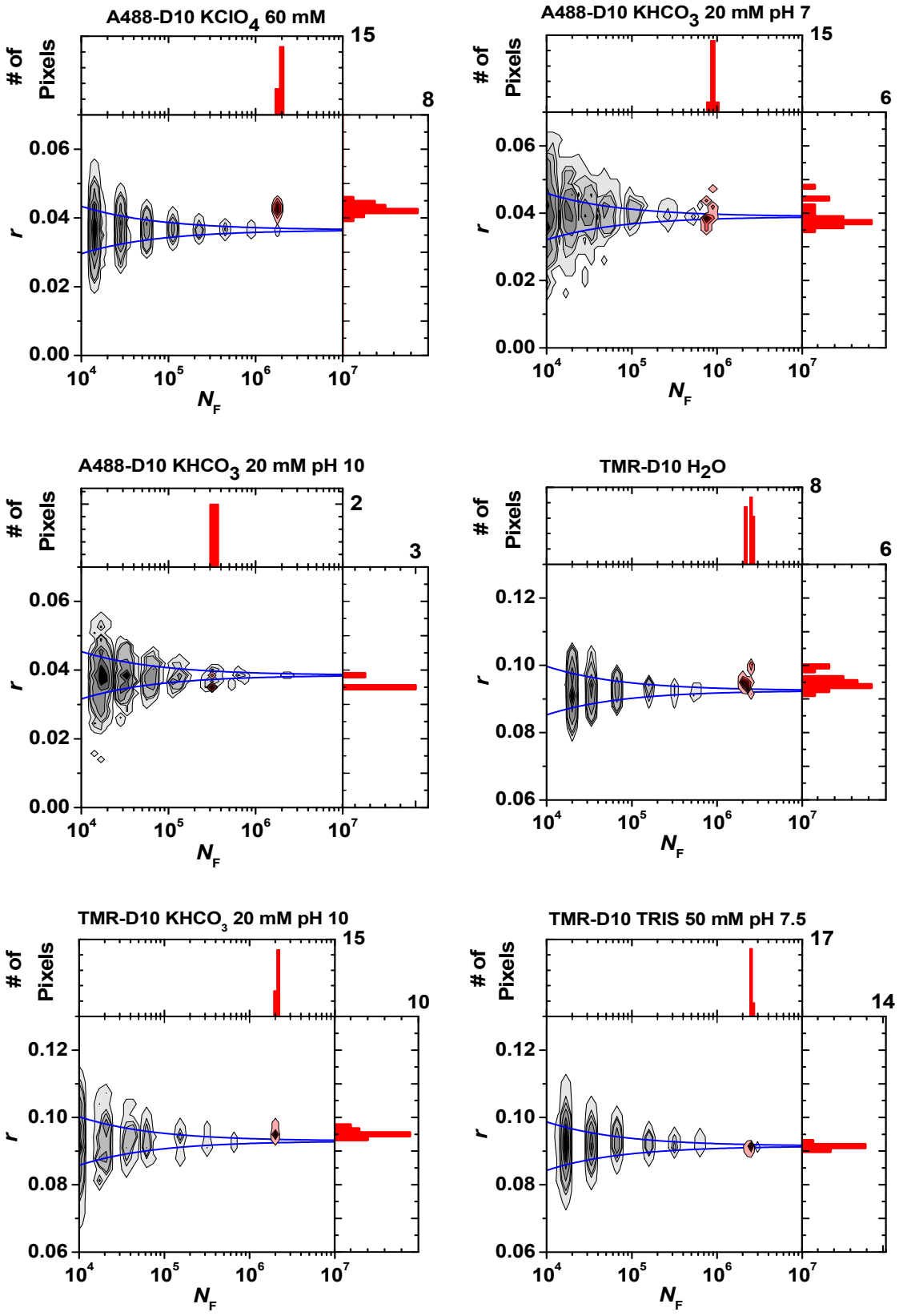
A488-D10 KClO4 60 mM
A488-D10 KHCO3 20 mM pH 7
A488-D10 KHCO3 20 mM pH 10
TMR-D10 H2O
TMR-D10 KHCO3 20 mM pH 10
TMR-D10 TRIS 50 mM pH 7.5
# of Pixels
r
NF

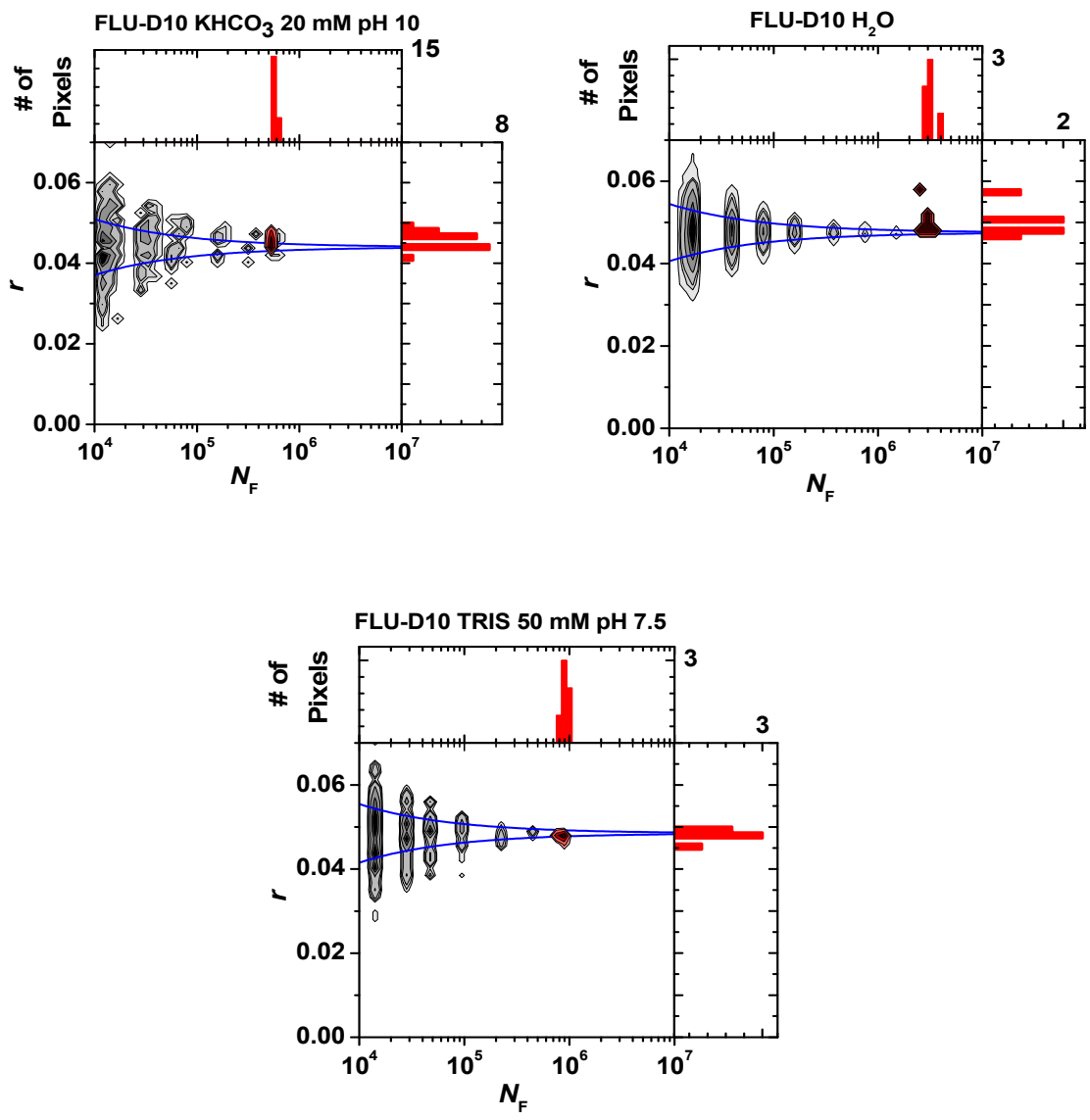

Figure S4. 2D plots of anisotropy r vs. photon number N_F for A488-D10, TMR-D10 and FLU-D10 in solution (gray contour lines) and in hydrogel (red contour lines) with 1D projections for the gel data.

For A488-D10 the plots show markedly different anisotropies inside the hydrogel for different solvent conditions. In case of $KClO_4$ 10 mM, 20 mM, 40 mM and KCl 20 mM the anisotropy in the gel is higher as compared to the solution value, in these cases the trapped fraction is≥10 %. The decrease in anisotropy starts with higher ionic strength: 60 mM $KClO_4$ and 20 mM in carbonate buffer pH 7 and 10, clearly correlated with the trapped fraction of the molecules as determined by FCS. For TMR-D10 and FLU-D10 the anisotropy is slightly higher or equal in comparison to solution measurements in different conditions (trapped fraction≤4%).

S8. *Fluorescence anisotropy A488-D10, TMR-D10 and FLU-D10*

Sample	Solvent	*r*		Trapped fraction
		Solution	Hydrogel	x
Rh110	H_2O	0.010	0.010	0
A488	H_2O	0.014	0.018	0.011
A488-D10	H_2O	0.037	0.049	0.296
A488-D10	$KClO_4$ 10 mM	0.037	0.049	0.168
A488-D10	$KClO_4$ 20 mM	0.037	0.046	0.125
A488-D10	KCl 20 mM	0.037	0.046	0.096
A488-D10	$KClO_4$ 40 mM	0.037	0.045	0.100
A488-D10	$KClO_4$ 60 mM	0.036	0.041	0.090
A488-D10	$KHCO_3$ 20 mM pH	0.039	0.040	0.076
A488-D10	$KHCO_3$ 20 mM pH	0.037	0.037	0.070
TMR-D10	H_2O	0.093	0.096	0.040
TMR-D10	$KHCO_3$ 20 mM pH	0.093	0.094	0
TMR-D10	TRIS 50 mM pH	0.092	0.092	0
FLU-D10	$KHCO_3$ 20 mM pH	0.044	0.046	0
FLU-D10	H_2O	0.047	0.049	0
FLU-D10	TRIS 50 mM pH	0.047	0.047	0

Table S7. Average anisotropy (*r*) for Rh110, A488, A488-D10, TMR-D10 and FLU-D10 in solution and in the hydrogel for different salt conditions.

S9. *Reference data*

Published experimental hydrodynamic radii for dextrans labelled with A488, TMR or fluorescein are compiled in Figure SI 5.

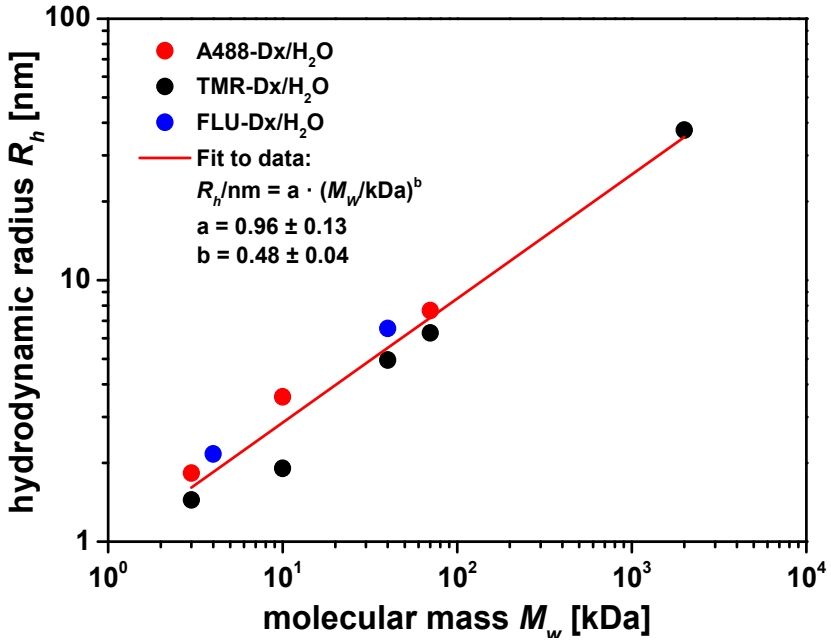

Figure S5. Fit of Flory scaling law to reference data for A488-D3 & A488-D10[121], A488-D70[122], TMR-Dx[116] and FLU-Dx[121]. R_h was taken as published or calculated via Stokes-Einstein equation. The systematic difference between TMR-Dx data (measured at 23 °C) and A488-Dx and Flu-Dx data (measured at 32 °C, except A488-D70 measured at 25 °C) is mainly attributed to calibration uncertainties. Reported temperature effects on R_h of dextrans in the relevant temperature and size range are about one order of magnitude smaller than the deviation of the two data sets and in the opposite direction: $-\Delta R_h/(R_h \Delta T) < 0.003\,\mathrm{K}^{-1}$ (extracted from Figure 1 in ref.[131]).

S10. *NMR Measurements*

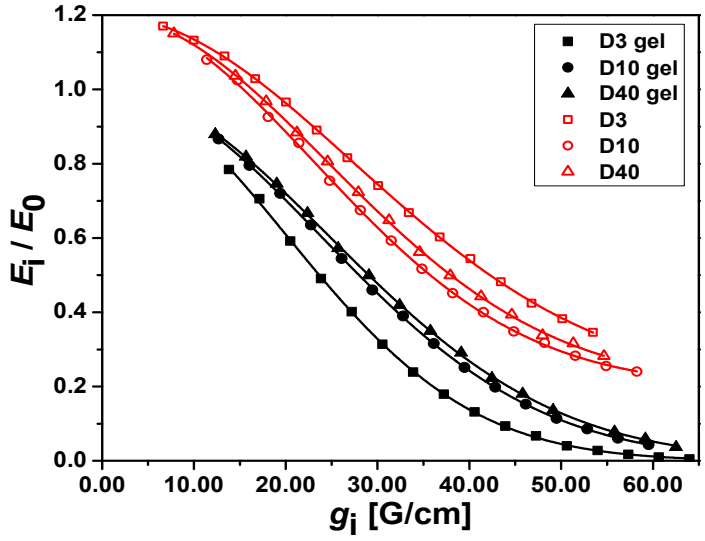

Figure S6. NMR data and fits for unlabelled dextrans (3 kDa, 10 kDa and 40 kDa) in hydrogels and in D_2O. Data was normalized and *xy* offset-corrected. For clarity reasons, the solution data (red) was vertically offset by 0.2.

The diffusion coefficients *D* were obtained by fitting the echo amplitudes (integral of the signals between 2.8 and 4.4 ppm) using Eq.2.7 (See main text). We performed several diffusion measurements with each sample, varying the key parameters δ and Δ_N and keeping constant the values of τ_N = 0.001 s and γ=26752.22005 rad/s Gauss. Several combinations of Δ_N and δ were applied and the specific parameters are listed in the table S8.

	Solution			**Hydrogel**		
	δ [µs]	Δ_N [s]	D_{sol} [10^{-10}m^2/s]	δ [µs]	Δ_N [s]	D_{gel} [10^{-10}m^2/s]
D3	600	0.60	1.12	600	1.80	0.67
	800	0.30	1.15	700	1.40	0.65
	1000	0.10	1.16	800	1.00	0.68
D10	1000	0.30	0.97	750	1.70	0.30
	1200	0.25	0.96	1000	1.30	0.33
	1600	0.10	0.97	1500	0.50	0.31
D40	800	1.00	0.38	1200	1.60	0.096
	1000	0.80	0.38	1300	2.00	0.085
	1200	0.60	0.37	1400	1.80	0.096

Table S8. Parameters used for NMR measurements for unlabelled dextrans D3, D10 and D40. The fit provides the diffusion coefficient for each sample for the different experimental settings. The rows marked in yellow represent the curves shown in figure S6.

S11. *Technical details of the Brownian dynamics simulation*

General

In our Brownian dynamics simulation[106], we use a cubic simulation box with periodic boundary conditions containing 512 matrix particles and 1 tracer particle. About 200 independent simulation runs have been performed to generate typical trajectories for the statistical averages of the tracer's mean square displacements. The Brownian equations of motion were integrated with an Euler-algorithm. The time step Δt for the integration was chosen as $\Delta t < 2 \cdot 10^{-5}\ \tau_B$ (for model 1, 2 and 3a, TMR) and $\Delta t < 1.5 \cdot 10^{-6}\ \tau_B$ (for model 3b, TMR). $\tau_B = a^2 / D_0$ denotes the Brownian time. Here, a is the lattice constant of the matrix and D_0 the diffusion constant of the tracer particle in a pure solvent as obtained from the experiments. For FLU, Δt had to be chosen 10 times smaller. We carefully checked that the results for the statistical averages did not change upon further decreasing the time step such that the magnitude of Δt was small enough.

Simulation protocol

In our simulations we used the following protocol:

- Generation of the underlying gel structure:
  - The gel obstacles were placed on a simple cubic lattice of lattice constant a.
  - The matrix particles were randomly shifted up to half the lattice constant in each direction in model 2, 3a and 3b.
  - Springs were attached between the centers of neighboring matrix particles which were all undistorted, i.e. the rest lengths equaled exactly the corresponding particle separations.
- The tracer particle was placed in a void.
- The BD simulation was started and the system was equilibrated for a typical time of $t_{\mathrm{eq}} >= 1\ \tau_B$.
- Statistics for the dynamical correlations was gathered by storing at least 100000 snapshots of the tracer trajectory $\vec{s}(t)$ at equidistant times within a sufficiently large time window of $t_{\mathrm{max}} >= 40\tau_{\mathrm{B}}$. In this time window, the tracer moved on average a distance of several lattice constants a.

Calculation of the hindrance factors

It was carefully checked that the long-time limit of the tracer's mean square displacement $\Delta s^2(t) = \left\langle \left(\vec{s}(t_0 + t) - \vec{s}(t_0) \right)^2 \right\rangle$ was reached. Here, <…> denotes the average over all $t_0 \in [0, t_{max} - t]$ and all independent simulation runs. The diffusion coefficient was obtained as $D = \lim_{t\to\infty} \frac{1}{6} \frac{\mathrm{d}}{\mathrm{dt}} \Delta s^2(t)$.[106, 107] As for an example, see Figure S7. We then performed a fitting procedure to describe the experimental hindrance factors $H=D/D_0$ as a function of R_h.

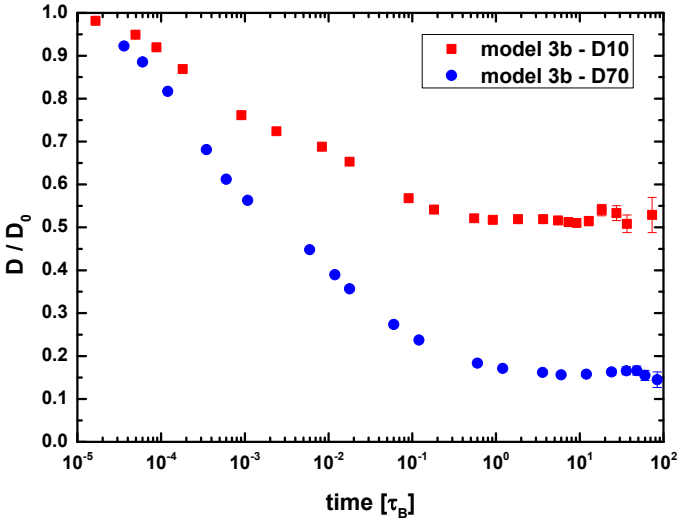

Figure S7. Hindrance factor D/D_0 versus time for two different tracers (D10 and D70) within model 3b. For very short times, the Diffusion coefficient approaches the Diffusion coefficient in solution D_0, as no collisions occur during these times. The long-time-limes is reached before 1 τ_B, as the diffusion coefficient does not decrease any further

Parameters

All model parameters were fixed according to Table S9 except the lattice constant a, which sets the pore size, and the obstacle radius R_{obst}, which was scaled with a factor such that the constraint of the experimentally prescribed volume fraction, φ, (measured by swelling analysis, see main text Sec. 2.2.1.1) was fulfilled: $R_{obst} = \sqrt[3]{\frac{3\varphi}{4\pi}} a$. This leads to a coarse-grained obstacle radius comparable to the tracer size at least of the same order of magnitude. The additive diameters σ_{ij} used in Eq. (2.8), (2.10), (2.11) were therefore also fixed by $\sigma_{ij}=2 R_{obst}$ for the obstacle-obstacle-interaction and $\sigma_{ij}=R_{obst} + R_h$ for the interaction between a

matrix obstacle and a tracer of radius R_h. For the guest particle radii R_h, we used our experimental values (see R_h in Table 3 in the results, 3.2.1). The short-time diffusivity of the obstacles was calculated via the Stokes-Einstein relation $D_{obst} = \frac{k_B T}{6\pi\eta R_{obst}}$. Here, η = 0.00095 Pa s is the viscosity of the solvent at T = 295 K (= 22 °C). We used ε_s=1 k_BT for the WCA-potential used in model 1, 2 and 3b. In model 3a, we used ε_G =12 k_BT since this value is above the value of 2 k_BT, which is found for self-avoiding polymers [104] but we expect our system to be stiffer. We have changed ε_G within the range of 4 k_BT and 20 k_BT and did not obtain an improved fit to the experimental data.

In conclusion, out of the 12 parameters shown in Table S9, 9 are fixed by physical constraints, namely the obstacle radius R_{obst}, and consequently also the obstacle self-diffusion constant D_{obst} and the additive diameters $\sigma_{obst,\ obst}$, $\sigma_{obst,\ D0}$, $\sigma_{obst,\ D3}$, $\sigma_{obst,\ D10}$, $\sigma_{obst,\ D40}$, $\sigma_{obst,\ D70}$, $\sigma_{obst,\ D500}$. Hence only 3 parameters are left: The lattice constant a, the spring constant k and the interaction parameters ε_s, resp. ε_G, (plus possibly the parameter ε_a in model 3b). ε_a and a are real fit parameters. We have checked that a change of k and the interaction parameters ε_s, resp. ε_G give indifferent fit quality.

Fitting and conclusion

For the fixed choice of a, the whole hindrance factors H were simulated as a function of R_h, i.e. for all tracer radii used in the experiments. These sets of simulation data were compared to the experimental data and an optimal value of a was obtained by the best fit. For model 3b, two fit parameters were used, namely the lattice constant a and the attraction strength ε_a. This results in better fitting in particular for small R_h. We remark here that the attraction was essential. In a purely repulsive dextran-matrix interaction model, a second fit parameter would not give a significant improvement of the fit. Additional simulations performed within model 3b using a Gaussian softened core showed a similar fit quality as that with a WCA-core such that we conclude that the attraction itself rather than the details of the repulsion is crucial to describe the experimental data properly.

Dye	Model	initial gel simple cubic lattice constant [10^{-9}m]	obstacle radius [10^{-9}m]	obstacle self diffusion constant [10^{-11}m^2/s]	spring constant [10^{-4}N/m]	Matrix-dextran-interaction parameters (at T=20 °C) [10^{-20}J]	$\sigma_{obst,obst}$ [10^{-9}m]	$\sigma_{obst,D0}$ [10^{-9}m]	$\sigma_{obst,D3}$ [10^{-9}m]	$\sigma_{obst,D10}$ [10^{-9}m]	$\sigma_{obst,D40}$ [10^{-9}m]	$\sigma_{obst,D70}$ [10^{-9}m]	$\sigma_{obst,D500}$ [10^{-9}m]
TMR	1	11.75	2.48	0	inf	$\varepsilon_s = 1k_BT \approx 0.405$	4.95	3.03	4.19	5.55	8.48	10.34	
	2	11.75	2.48	9.18	6.17	$\varepsilon_s = 1k_BT \approx 0.405$	4.95	3.03	4.19	5.55	8.48	10.34	
	3a	10.03	2.11	10.77	6.17	$\varepsilon_G = 12k_BT \approx 4.86$	4.23	2.66	3.82	5.18	8.11	9.97	
	3b	14.35	3.02	7.52	6.17	$\varepsilon_s = 1k_BT \approx 0.405$ $\varepsilon_a = 3k_BT \approx 1.21$	6.05	3.57	4.73	6.09	9.02	10.88	
FLU	1	31.73	4.86	0	inf	$\varepsilon_s = 1k_BT \approx 0.405$	9.73	5.41	6.57	7.93	10.86		25.16
	2	31.73	4.86	4.68	6.17	$\varepsilon_s = 1k_BT \approx 0.405$	9.73	5.41	6.57	7.93	10.86		25.16
	3a	30.29	4.64	4.90	6.17	$\varepsilon_G = 12k_BT \approx 4.86$	9.29	5.19	6.35	7.71	10.64		24.94
	3b	44.71	6.85	3.32	6.17	$\varepsilon_s = 1k_BT \approx 0.405$ $\varepsilon_a = 3k_BT \approx 1.21$	13.71	7.40	8.56	9.92	12.85		27.15

	D0	D3	D10	D40	D70	D500
radius [10^{-9}m]	0.55	1.7	3.1	6.0	7.9	20

Table S9. Parameters used for Brownian dynamics simulations for model 1 (fixed gel matrix, steric interaction), model 2 (flexible gel matrix, steric interaction), model 3a (flexible gel matrix, soft interaction), model 3b (flexible gel matrix, steric interaction and attractive shell).

Chapter 3 Strategies to improve the fluorescence signal and photostability of the cyanine dye Cy5

D. Sandrin, [1] D. Dörr, [1] R. Kühnemuth, [1] B. Mayer, [2] T. J. J. Müller, [2] C. A. M. Seidel [1]

[1] *Institut für Physikalische Chemie II, Molekulare Physikalische Chemie,*

Heinrich-Heine-Universität, Universitätsstr. 1, 40225 Düsseldorf, Germany

[2] *Institut für Organische Chemie und Makromolekular Chemie,*

Heinrich-Heine-Universität, Universitätsstr. 1, 40225 Düsseldorf, Germany

Abstract

The design of an ideal fluorophore is a big challenge in fluorescence spectroscopy and imaging. The usage of photostabilizing additives that quench long lived dark states seems to be the only available option for improving the photostability of the dye. To stabilize the cyanine dye Cy5, we use quenchers: 4-(phenylazo) benzoic acid (AZB-C) and 6-Hydroxy-2,5,7,8-tetramethylchroman-2-carboxylic acid (Trolox) as additives.

Recently, a new approach is presented where the dye is covalently linked to the quencher in order to overcome biological toxicity of the additives. Moreover, we synthesize two conjugates, where Cy5 is covalently linked to AZB-C (Cy5-AZB-C) and Trolox (Cy5-Trolox) respectively.

Using quantitative fluorescence correlation spectroscopy (FCS) in combination with fluorescence signal saturation analysis and bulk bleaching experiments we compare the effects of the additives with the Cy5-conjugates. Our studies reveal impact of the different quenchers on the photostability of the dye in buffer/ethanol and air/argon solution.

In air saturated solution, the FCS experiments indicate presence of three processes involving dark states namely: *cis* isomer, triplet and radical cation. Under argon conditions only *trans-cis* isomerization and intersystem crossing are the dominating processes. The measurements reveal that AZB-C is a triplet quencher that can also reduce the radical cation state produced only in oxidizing aqueous solutions. Trolox affects only the triplet state of the dye.

By using conjugated Cy5-AZB-C the population of dark states is strongly reduced. With Cy5-AZB-C the triplet state is dramatically quenched in argon experiments and is also the best way to suppress the production of $R^{\bullet+}$ in air saturated solution due to high formal local concentration of the quencher. However, the conjugated compounds show strong fluorescence quenching in water and very weak in ethanol. Additives and conjugates do not have any influence in the isomerization process.

The photobleaching experiments show that oxygen is the main source for bleaching reaction via singlet state under air saturated conditions. The presence of O_2, in aqueous solution promotes very fast degradation of the dye, and only the presence of Cy5-AZB-C resulted in the most significant stabilization by a factor of ~5. Under buffer argon conditions triplet state represents the main pathway of the bleaching reactions.

A good strategy for improving fluorescence signal (by factor of ~ 2) together with photostability of the dye consists of the oxygen removal and addition of the triplet quencher like AZB-C simultaneously. Our studies allow us to give recommendations regarding the best conditions to employ in order to get the most ideal fluorophore.

3.1 Introduction

Investigation of biological systems with fluorescence spectroscopy and microscopy,[33] involves the use of organic fluorophores. In an ideal chromophore, optical excitation results only in cycles between the first singlet excited state (S_1) and the ground state (S_0) under fluorescence emission. The instability of the fluorophores is caused by multiple processes, starting from the triplet state transition (blinking) and ending with irreversible damage (photobleaching).[25, 132] In air, the production of a superoxide radical ($^{\bullet}O_2^-$) and a non-fluorescent, cation radical state ($R^{\bullet+}$) of the dye is highly probable, caused by the electron transfer between triplet state of the dye and O_2.[31] Moreover, the energy transfer from a triplet fluorophore to molecular oxygen can produce singlet oxygen ($^1O_2$).[133-135] The combination of $^{\bullet}O_2^-$, $^1O_2$ with other chemical reactions could generate many reactive oxygen species like $OH^{\bullet}$, $HO_2^{\bullet}$ and H_2O_2 causing photobleaching and therefore damage of the dye.[23] Then, the presence of oxygen and the nature of the solvent are important factors that influence the fluorescence signal of the fluorophore. Therefore, chemical structure and the redox potentials are crucial for its stability, predetermining the success of the experiment in different environments and solvents.

For this reason, in the last years many studies were conducted in order to improve the photostability of the fluorophores using additives. Compounds, like 6 Hydroxy-2,5,7,8-tetramethylchroman-2-carboxylic acid (Trolox), ascorbic acid, cyclooctatetraene (COT), 4-nitrobenzyl alcohol (NBA) were applied, showing improvements of fluorescence signal.[26-28, 56, 136-138]

Recently, a new approach was presented to stabilize a cyanine chromophore where the dye is covalently linked to the quencher.[29-32, 139-141] The self-healing method overcomes problems like poor aqueous solubility of the quenchers, membrane permeability and biological toxicity.

The importance to study the photochemistry of cyanine dye is due to their large absorption cross sections, fluorescence efficiencies and commercially availability as derivatives for covalent labelling of proteins and nucleic acids.[23]

Here we study the influence of the quenchers: 4- (phenylazo) benzoic acid (AZB-C) and Trolox on the Cy5 dye stability.

In this work we synthetize Cy5-conjugates with AZB-C and Trolox respectively, and characterize their chemical-physical properties by comparing them with the Cy5 free dye without and with additives. To get a complete picture, we perform ensemble spectroscopy experiments in two solvents (aqueous buffer Na_2HPO_4/NaH_2PO_4, 20 mM, pH 7 or ethanol) and in different atmospheres (air or argon) to distinguish between different photophysical processes that could occur in different environments. We use FCS to gain the information about the impact of the quenchers on the brightness and on the photochemistry of Cy5.

3.2 Materials and methods

3.2.1 Samples

All the measurements were performed in phosphate buffer (Na_2HPO_4/NaH_2PO_4) 20 mM, pH 7 and in ethanol (see below) with temperature of 20±1 °C. The quenchers (Q), AZB-C (4-(phenylazo) benzoic acid) and Trolox ((±) 6 Hydroxy-2,5,7,8-tetramethylchroman-2-carboxylic acid) were purchased from Sigma-Aldrich and used without further purification. The Cy5 dye (sulfo-Cy5 carboxylic acid) and its Cy5 conjugated quenchers were prepared by us with chemical synthesis[29, 142-145] and purified with silica gel column chromatography and HPLC (See S1 for details of synthesis). Below, the compounds used in our studies are shown: free dye (Cy5), dye with the addition of quenchers (Cy5+Q) and dye-conjugates (Cy5-Q).

Dye	Quencher	Dye-Quencher
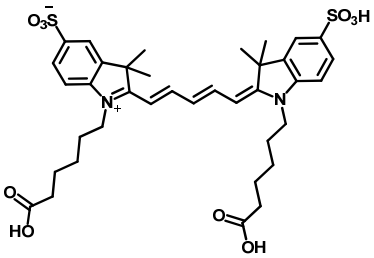 Cy5	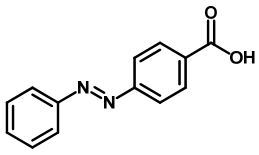 AZB-C	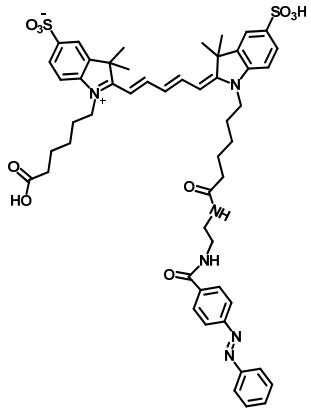 Cy5-AZB-C
	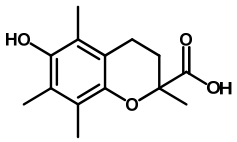 Trolox	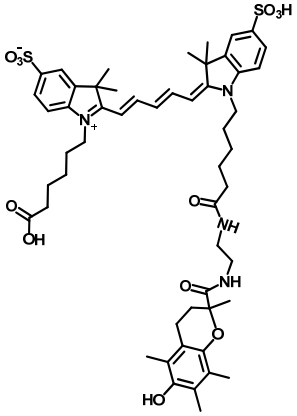 Cy5-Trolox

Table 3.1. Compounds used in our experiments: Cy5, Cy5 + quenchers in solution and Cy5-conjugates (Cy5-AZB-C and Cy5-Trolox).

3.2.2 Measurements Methods

3.2.2.1 Ensemble Spectroscopy

Absorption and emission spectra

To characterize the Cy5-Q prepared with synthesis, we performed absorption measurements with the UV-Vis spectrometer (Cary 4000, Agilent Technologies) and fluorescence emission and excitation spectra with fluorescence spectrometer (FluroMax-4, Horiba Scientific), in phosphate buffer (Na_2HPO_4/NaH_2PO_4) 20 mM, pH 7 and in ethanol. To exclude polarization effects, the fluorescence of the probe was observed in a conventional 90° setup with the emission polarizer

set to the magic angle (54.7°). For emission spectra λ_{Ex}= 615 nm was used and for excitation spectra λ_{Em}= 710 nm.

To study the dynamic and static quenching by Stern-Volmer experiments, we recorded emission spectra of Cy5 with different concentrations of AZB-C and Trolox in ethanol due to the poor solubility of quenchers in aqueous solution.

Fluorescence quantum yield

Fluorescence quantum yield (Φ_F) was determinate using a comparison with a standard dye taking adsorption and emission spectra according to ref. [146] Rhodamine 700 in ethanol (Φ_F = 0.38)[147] was used as reference dye for Cy5 and Cy5-Q. For absorption spectra the optical density was kept below 0.01 to avoid inner filter effects. For the emission we recorded the complete spectra exciting at λ_{Ex}= 615nm and in a second stage we excited at λ_{Ex}= 640nm close to the maximum absorption. The emission polarizer was set to the magic angle (54.7°). Exactly the same conditions were used for all our samples and for the standard dye. The background of the solvent was also measured in the same conditions and subtracted from the emission spectrum. The measurements were performed in phosphate buffer (Na_2HPO_4/NaH_2PO_4) 20 mM, pH 7 and in ethanol.

Fluorescence lifetime

Ensemble time-correlated single-photon-counting (eTCSPC) measurements were performed using white light laser from NKT Photonics with repetition rate 20 MHz at Picoquant FT300 setup. The maximum counts in the peak for the fluorescence decay– 50000 counts.

The measurements were performed in phosphate buffer (Na_2HPO_4/NaH_2PO_4) 20 mM, pH 7 and in ethanol. To determine dynamic quenching constants by Stern-Volmer experiments, we performed measurements of Cy5 with different concentrations of AZB-C and Trolox in ethanol due to the poor solubility of quenchers in aqueous solution.

3.2.2.2 Measurements in a confocal setup

The experiments were carried out with a confocal epi-illuminated microscope. The fluorescent molecules were excited by a diode laser (Cobolt MLD™) at 638 nm in (continuous wave) CW mode. The laser was focused into the sample by a water-immersion objective lens (UPLAPO 60 NA = 1.2, Olympus, Hamburg, Germany). The fluorescence was collected by the same objective,

separated from the excitation by a dichroic beam splitter (488/636 PC, AHF, Tübingen, Germany). The signal was detected by two avalanche photodiodes (photon counting module SPCM-AQR-14, Perkin Elmer) in a beam splitting arrangement to eliminate dead time and after-pulsing artefacts. Fluorescence band pass filters (HQ 730/140 M and HQ 680/60 M) block residual light and reduce the Raman-scattered light from the solvent. The O.D. filters (Thorlabs) of 0.5 and 0.4 were used for air saturated buffer measurements.

For FCS experiments the signals of the two detectors were processed by homebuilt hardware correlator (4 ns -13 s). Using the same correlator we measured the fluorescence signal with 1 ms resolution. Electric shutter was used, where 5 ms was the opening time.

The mean intensity $\langle I \rangle$ is equal $\langle I \rangle = I_0 / 2$ and depends on the power objective (See S2). For our fit analysis we use more accurate power density using Gauss-Lorentzian profile where power for FCS and signal are treated differently (for details See S2). We performed measurements in phosphate buffer (Na_2HPO_4/NaH_2PO_4) 20 mM, pH 7 and in ethanol. Moreover, we performed experiments in air saturated solution and in argon environments. For experiments in argon, before to start the measurement, the solution has been deoxygenated by using argon for 30 min. in a closed chamber with a septum.

3.2.2.3 Photobleaching

In the setup of the cell-bleaching experiment, a constantly stirred dye solution in a quartz cuvette (1×1 cm^2) is illuminated by a continuous wave krypton ion laser (Innova Sabre, Coherent, Palo Alto, CA) at 647.1 nm. Using appropriate long-pass filters (HQ 730-140), the fluorescence light is detected perpendicular to the excitation light by a photodiode (S1226-8BQ, Hamamatsu, Hamamatsu City, Japan). A part of the excitation light is monitored by a second photodiode to correct for possible fluctuations (reference detector). The two time-dependent amplified signals are read into a computer by an analog-to-digital converter PC board (WIN 30D, Meilhaus Electronic, Puchheim, FRG).

The concentration of Cy5 and Cy5-Q was kept constant for each experiment (0.5 nM) with total volume of 3 mL. We studied the influence of the solvent performing measurements in phosphate buffer (Na_2HPO_4/NaH_2PO_4) 20 mM, pH 7 and in ethanol. Moreover, in order to investigate different environment conditions, we performed our experiments in air saturated solution and in

argon environments. For experiments in argon, before to start the measurement, the solution has been deoxygenated by using argon for 30 min. in a closed cuvette.

3.2.3 Analysis Methods

3.2.3.1 Ensemble Spectroscopy

Fluorescence quantum yield

According to the ref.,[146] the quantum yield of the unknown compound was calculated using eq.(3.1):

$$\Phi_F = \Phi_{F,R} \frac{F}{F_R} \frac{OD_R}{OD} \frac{n^2}{n_R^2} \tag{3.1}$$

where Φ_F is the fluorescence quantum yield, F is the integrated fluorescence intensity, OD is the optical density, and n is the refractive index. The subscript R refers to the reference fluorophore of known fluorescence quantum yield. In our case Rhodamine 700 in ethanol was used, with $\Phi_{F,R} = 0.38$.[147]

For the absorption spectra we applied baseline correction, while for emission spectra the background of the solvent was subtracted. During the analysis the emission spectra measured with λ_{Ex}= 615 nm was normalized to the maximum and then multiplied with the fluorescence intensity measured at λ_{Ex} = 640 nm. The area was integrated and used in the eq. (3.1), we applied the same analysis for the samples and for the reference. Correction for the solvent refractive index was necessary for phosphate buffer measurements.

Fluorescence lifetime and fluorescence quenching

We describe the fluorescence decays $F(t)$ of Cy5 and Cy5-Q by up to four fluorescence lifetimes τ_i with the species fractions x_i and a species-averaged fluorescence lifetime $\langle\tau\rangle_x$.

$$F(t) = x_1 \exp(-t/\tau_1) + x_2 \exp(-t/\tau_2) + x_3 \exp(-t/\tau_3) + x_4 \exp(-t/\tau_4) \tag{3.2}$$

$$\langle\tau\rangle_x = x_1\tau_1 + x_2\tau_2 + x_3\tau_3 + x_4\tau_4 \tag{3.3}$$

The part of the decay in the range from the maximum of the instrument response functions (IRF) to the first time channel with less than 100 detected photons was fitted.

The results of the fluorescence lifetime analysis are summarized in Table 3.2.

The investigation of bimolecular static quenching (formation of a non-fluorescence ground-state complex between fluorophore and quencher) and dynamic quenching (collisional quenching during the lifetime of excited state of fluorophore), was done using Stern-Volmer analysis approach:[146]

$$F_0 / F = (1 + K_D[Q])(1 + K_S[Q]) = (1 + k_{q,D}\tau_0[Q])(1 + k_{q,S}\tau_0[Q]) \quad (3.4)$$

where F_0 is the fluorescence intensity in absence of quencher and F is fluorescence intensity in the presence of quencher Q with the concentration [Q]. K_D and K_S are respectively the static and the dynamic Stern-Volmer constants. The dynamic portion of the quenching can be determined by lifetime measurements:

$$\tau_0 / \tau = 1 + K_D[Q] = 1 + k_{q,D}\tau_0[Q] \quad (3.5)$$

where τ_0 is fluorescence lifetime without quencher and τ is fluorescence lifetime with the quencher. If only the collision quenching (dynamic) occurs:

$$F_0 / F = \tau_0 / \tau \quad (3.6)$$

Static quenching does not decrease the lifetime because only the fluorescent molecules are observed, and the uncomplex fluorophores have the unquenched lifetime τ_0.

It should be noted that the lifetime used in our data analysis (See Sec. 3.3) is species-averaged fluorescence lifetime $\langle\tau\rangle_x$.

3.2.3.2 Electrochemical potentials

The spontaneity of chemical reactions is given by the change in free energy, ΔG^0. The negative value of ΔG^0 indicates thermodynamically allowed reactions. The Rehm-Weller equation[148, 149] permits to calculate the ΔG^0 value of electron transfer between an excited-state sensitizer and quencher:

$$\Delta G^0 = E_{ox} - E_{red} - \Delta E_{n0} - \Delta G^0(\varepsilon) \quad (3.7)$$

where E_{ox} and E_{red} are the oxidation and reduction potentials of electron donor and acceptor, respectively and ΔE_{n0} is the singlet or triplet excitation energy. The correction term $\Delta G^0(\varepsilon)$ describes the solvation and Coulomb interaction of solvent-separated ion pairs and is neglected in water.

3.2.3.3 Data analysis of confocal measurements

Kinetic scheme

The Figure 3.1 shows the electronic state model scheme applied in our studies[35, 56], the data were analyzed according to scheme (b) and (c), the representation in scheme (a) depicts the contribution of higher excited electronic states, which is the basics for Figure 3.1 (b).

The photo-oxidation process will occur in presence of oxygen generating the radical cation state ($R^{\bullet+}$). In argon solution no radical state is visible. Moreover, the solvent is also crucial in the stabilization of the charged states, i.e. the $R^{\bullet+}$ state is only visible in aqueous solution (See 3.3).

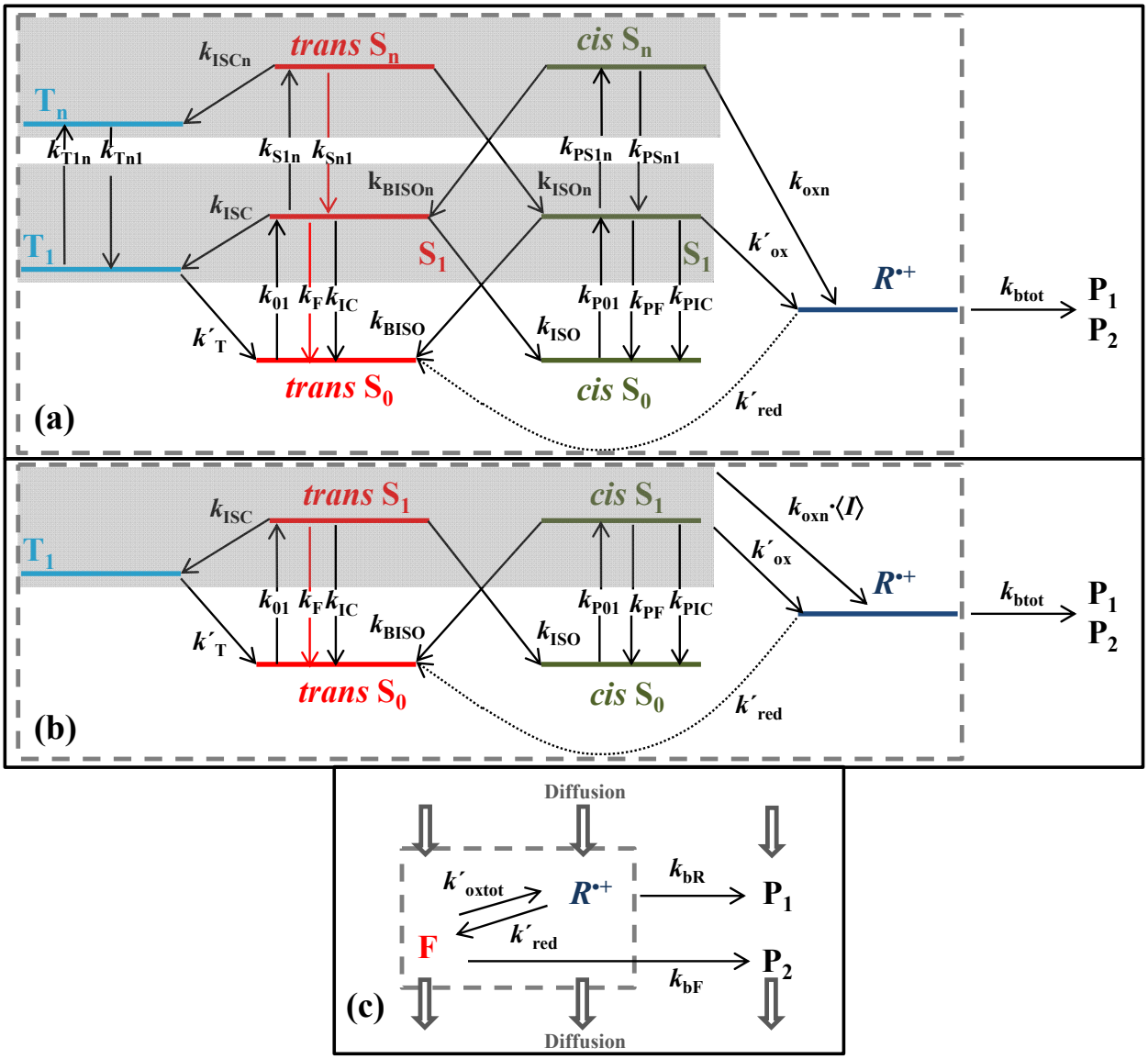

Figure 3.1. (a) Electronic energy diagram for cyanine dye where the contributions of higher excited electronic states (S_n and T_n) are directly considered. (b) Simplified scheme for Cy5

where the higher excited states are considered using irradiance dependent rate k_{oxn}. After the excitation process from *trans* S_0 to *trans* S_1 (k_{01}) the S_1 depopulation can occur via the typically fluorescence emission (k_F), internal conversion (k_{IC}), intersystem crossing (k_{ISC}) or photoinduced *trans-cis* isomerization (k_{ISO}). Once the dye is in *cis* S_0 state, it can be excited in *cis* S_1 and going back (k_{BISO}) to the *trans* state. The fluorescence quantum yield of the *cis* isomer is considered negligible (k_{PF}).[35] The photo-oxidation (k'_{ox}) can happen from all 3 excited states: singlet *trans* (S_1), singlet *cis* (S_1) and triplet (T_1) originating the radical cation ($R^{\bullet+}$). The consequent photobleaching (dashed grey line) can occur from all the states (k_{btot}). (c) Further simplification of the scheme with the photo-oxidation (k'_{oxtot}) and reduction (k'_{red}) of Cy5 and consequent photodamage from $R^{\bullet+}$ state (k_{bR}) and from F state (k_{bF}) generating products ($P=P_1+P_2$) is shown.

It is known that the cyanine dyes in the ground state exist primarily in the all-*trans* conformation.[150, 151] Once Cy5 is excited to its first excited singlet state (*trans* S_1) the deactivation can occur in different ways:

- Fluorescence emission from *trans* S_1 state (k_F)
- Internal conversion (k_{IC})
- Intersystem crossing to the lowest triplet state (k_{ISC})
- Photoinduced *trans-cis* isomerization (k_{ISO})

It is believed that the photoisomerization induces the generation of a mono *cis* species, where only the rotation around one of the double bonds occurred.[23, 151] Moreover, the fluorescence quantum yield of mono *cis* conformation is very low.[152-154] The back-isomerization of the cis isomer yields the thermodynamically stable all-*trans* isomer. The total process depends strongly on solvent viscosity; in contrast influence of the polarity is less significant.[23, 35] Indeed, when the cyanine dyes are dissolved in highly viscous solvents or bound to biomolecules, the efficiency of fluorescence increases significantly.[155-158]

Fluorescence correlation spectroscopy (FCS)

FCS is a sensitive analytical tool that, given an appropriate model, permits to analyse spontaneous fluorescence intensity fluctuations of fluorescent molecules as: diffusion coefficients, hydrodynamic radii, average concentrations, kinetic chemical reaction rates, singlet-triplet dynamics. With FCS it is possible to detect the spontaneous fluorescence intensity fluctuations of fluorescent molecules typically excited in a focussed beam. In our case, these

fluctuations are caused by translational diffusion into and out of the sample volume element and by dark states formation like triplet, *trans-cis* isomerization and radical state.
Assuming the model in Figure 3.1, we fitted the data using eq.(3.8):

$$G(t_c) = 1 + \frac{1}{N_S} \cdot \left(\frac{1}{1 + \frac{t_c}{t_D}} \right) \cdot \left(\frac{1}{\sqrt{1 + \left(\frac{\omega_0}{z_0} \right)^2 \cdot \left(\frac{t_c}{t_d} \right)}} \right) \cdot \left(\underbrace{1 - A_2 + A_2 \cdot e^{t_C \cdot \lambda_2} - A_3 + A_3 \cdot e^{t_C \cdot \lambda_3}}_{\text{Fast processes: µs range}} \underbrace{- A_R + A_R \cdot e^{-\left(\frac{t_C}{t_R} \right)}}_{\text{Slow process: ms range}} \right) \quad (3.8)$$

In this case, N_S is the number of molecules in the singlet state in the detection volume element and t_c is the correlation time; A_2, A_3, λ_2 and λ_3 are the amplitudes and the relaxation rates for the fast processes: triplet state and the isomerization term. The slow relaxation time corresponds to the possible formation of the radical cation state. The photo-oxidation depends on the presence of oxygen, solvent, specific additive used, quencher linked to the Cy5.
The model (eq.(3.8)) assumes a three-dimensional Gaussian-shaped volume element with spatial distribution of the detection probabilities $w(x, y, z) = \exp(-2(x^2 + y^2)/\omega_0^2) \exp(-2z^2/z_0^2)$. The $1/e^2$ radii in x and y or in z direction are denoted by ω_0 or z_0, respectively.

Using the model described in ref.[35] the relaxation rates (λ_2 and λ_3) for the fast processes are expressed as follows:

$$\lambda_{2,3} = -\left(\left[k_{ISC}'' + k'_T + k_{ISO}'' + k_{BISO}'' \right] / 2 \pm \left(\left[k_{ISC}'' + k'_T + k_{ISO}'' + k_{BISO}'' \right]^2 / 4 - k_{ISO}'' k'_T - k_{ISC}'' k_{BISO}'' - k'_T k_{BISO}'' \right)^{1/2} \right) \quad (3.9)$$

where:

$$k_{ISC}'' = \frac{k_{01}}{k_0 + k_{01}} k_{ISC} \quad (3.10)$$

$$k_{ISO}'' = \frac{k_{01}}{k_0 + k_{01}} k_{ISO} \quad (3.11)$$

$$k_{BISO}'' = \frac{k_{01}}{k_0 + k_{01}} k_{BISO} \approx \sigma_{BISO} \phi_{exc} \quad (3.12)$$

The amplitudes are described by eq.(3.13-3.14) :

$$A_2 = (\beta + \gamma)(k_T'\gamma + \delta)/(4\alpha\gamma) \tag{3.13}$$

$$A_3 = (\beta - \gamma)(k_T'\gamma - \delta)/(4\alpha\gamma) \tag{3.14}$$

where:

$$\alpha = k_{ISO}''k'_T + k_{ISC}''k_{BISO}'' + k'_T k_{BISO}'' \tag{3.15}$$

$$\beta = k_{ISC}'' + k_{ISO}'' + k'_T - k_{BISO}'' \tag{3.16}$$

$$\gamma = ((k_{ISC}'' + k_{ISO}'')^2 + (k_{BISO}'' + k'_T)^2 + 2(k_{ISO}'' + k_{ISC}'')(k_{BISO}'' + k'_T))^{1/2} \tag{3.17}$$

$$\delta = k'_T(k_{ISO}'' + k_{BISO}'' - k'_T - k_{ISC}'') + 2k_{ISC}''k_{BISO}'' \tag{3.18}$$

For the occupation probability of the states see ref.[35]

In our approach we assume to be negligible: (i) the fluorescence of the *cis* isomer and (ii) the contribution of higher excited triplet and singlet states, considering therefore only the model 1(b). In this way the photo-oxidation of Cy5 generating the radical state can occur from the 3 excited states (singlet *trans* (S_1), singlet *cis* (S_1) and triplet (T_1)) and the completely irreversible damage of the dye is possible from all the states (dashed grey line in Figure 3.1). The nature of the quencher is crucial for the photostability of the dye. In particular, it is reported that Trolox is a triplet quencher;[138, 159]differently AZB-C has strong effect on the triplet state and unexpectedly in our case it shows (See 3.3) also radical quenching effect. The presence or absence of oxygen and the nature of the solvent also affect the involvement of different electronic states and therefore in the photostability of Cy5.

In general, the rate constants k' depend on the nature of the specific quencher and its concentration [Q], influencing the speed of oxidation, reduction, and depopulation of triplet and single states:

$$k'_X = k_X + k_{qX}[Q] \tag{3.19}$$

In presence of photo-oxidation, the composite rate of oxidation is given by eq.(3.20)[160, 161]

$$k'_{oxtot} = (k'_{ox} + k'_{oxn}\langle I \rangle) \cdot S_{1eq}^5 \tag{3.20}$$

The oxidation contribution of higher excited states which is described by product of k_{oxn} and excitation irradiance is defined in the same way as the bleaching rate from excited states by Eggeling and co-authors.[160]

The steady state population S_{1eq} is defined for our model by eq. (3.21):

$$S_{1eq}^{5} = \frac{k'_T k_{BISO}''}{k_{ISO}'' k'_T + k_{ISC}'' k_{BISO}'' + k'_T k_{BISO}''} \left(\frac{k_{01}}{k_{01} + k_0} \right) \tag{3.21}$$

Using the diffusion coefficient (D_{cy5}=0.39 μm^{2}ms^{-1}) and the radius of excitation volume (ω_{0_ex} = 0.75 μm See S2) we calculate the characteristic diffusion time t_d which Cy5 needs to diffuse through excitation profile ($t_d \approx$ 0.3ms). For radical cation populations, kinetics in millisecond ranges are expected, hence the effect of diffusion on observed proprieties of $R^{\bullet+}$ must be considered. Due to diffusion the additional exchange between the molecules outside of excitation volume with lower probability for radical state and molecules inside of excitation volume with higher probability for radical state occur. Thus, the diffusion decreases the observed radical amplitude. We consider this effect of diffusive exchange by introducing radical lifetime dependent function $\eta_{D(t_R)}$, which was calculated using numerically solution of Fick´s law and assuming Gaussian-Lorentz excitation profile (See S5).

The FCS measurements were performed only with low powers ($\langle I \rangle$ = 2-85 kW/cm^2), under such conditions the amplitudes of photobleaching process are too small to be detected.

Hence, two level system with R and F states, can be used to describe the radical term using [161] eq.(3.24-3.26). However, the photobleaching could influence the equilibrium between R and F states. Then we include yields of bleaching for F and R states ($\Phi_{b,F}$ and $\Phi_{b,R}$ respectively) for calculation of R_{eq} and F_{eq}.

$$\Phi_{b,F} = \frac{k_{bF}}{k'_{ox} + k_{bF}} \tag{3.22}$$

$$\Phi_{b,R} = \frac{k_{bR}}{k'_{red} + k_{bR}} \tag{3.23}$$

The radical term is described like follows:

$$R_{eq} = \left(\frac{k'_{oxtot}}{k'_{oxtot} + (k'_{red}\eta_{D(t_R)})} \right) \left(1 - \Phi_{b,R}\right) \tag{3.24}$$

$$t_R = \frac{1}{k'_{oxtot} + (k'_{red}\eta_{D(t_R)})} \tag{3.25}$$

Due to the correction with the yields the sum of equilibrium amplitudes (R_{eq} and F_{eq}) became not equal 1. In all our fits we normalized both amplitudes to their sum (R_{eq}+F_{eq} =1).

And F_{eq} with eq. (3.26)

$$F_{eq} = (1 - R_{eq})(1 - \Phi_{b,F}) \tag{3.26}$$

In our FCS model eq.(3.8) R_{eq} corresponds to $A_{R.}$

FCS curves recorded under identical conditions for different excitation powers were analyzed by a global fit to calculate the kinetic parameters in Figure 3.1. The global fit consists of two steps. In the first step we determined the photophysical parameters that described the fast terms of the curves: triplet and isomerization processes by fitting FCS curves measured between $\langle I \rangle$ = 2-34 kW/cm^2. Then we fixed them for the second step of global analysis and fitted the curves for $\langle I \rangle$ > 34 kW/cm^2, to determine the parameters regarding radical term (only for air/buffer). Then, the constants obtained from FCS were used to fit F_{cpm} data (See 3.3). This analysis procedure is feasible because triplet and *trans-cis* isomerization kinetics can be treated independently from relaxation times of the radical term that differs by more than one order of magnitude (from µs to ms).

Fluorescence Signal

The average excitation rate constants k_{if} for excitation from an electronic state i to a higher excited state f depend on the mean excitation intensity within the detection volume $\langle I \rangle$ and are generally given by eq.(3.27)

$$k_{if} = \sigma_{if}(\lambda)\gamma\langle I \rangle \tag{3.27}$$

where σ_{if} is the excitation cross section at a wavelength λ , and γ is the reciprocal photon energy. The eq. (3.28) allows to calculate γ using the excitation wavelength λ, Plank's constant h and the velocity of light, c.

$$\gamma = \frac{\lambda}{hc} \tag{3.28}$$

The FCS measurements permit to obtain the fluorescence count rate per molecule F_{cpm}. It is computed by normalizing the measured fluorescence signal F_{sat} (with bleaching correction, see below) to the total number of molecules using eq.(3.29).

$$F_{cpm} = \frac{F_{sat}}{N_{tot}} \tag{3.29}$$

At higher excitation power, the apparent values of number of molecules extracted by FCS can be affected by saturation.[162] To avoid such problem, the total number of molecules N_{tot} for a given power series is an average value from FCS measurements at low irradiances ($\langle I \rangle$ =2-4 kW/cm^2). At such powers the processes involving intensity fluctuations of fluorescent molecules are triplet state and *trans-cis* isomerization of Cy5. At low power no bleaching and radical (A_{R}=0) are observed by FCS, the relaxation time of these process is too long and the amplitude too low to be detected.

Applying our model, the total number of molecule can be express by:

$$N_{tot} = \frac{N_S}{(1 - A_2 - A_3)} \tag{3.30}$$

For confocal measurements at low irradiance ($\langle I \rangle$ < 30 kW/ cm^2) we observed a constant fluorescence signal after starting illumination (See Figure 3.2). However, at high irradiances we observed complicated fluorescence decay behavior with two separated components. The fastest one is in the order of ms range. This fast decay can be explained by formation of ionic dye species, where immediate bleaching is also present. The slower processes (in the order of seconds) are assumed to originate mainly from reaching stationary condition determined by the accumulation of irreversibly photobleached products that exhibit no fluorescence. To be separated these two processes we measured the fluorescence signal decay (3 times) for each power density. A mono exponential fit (eq.(3.31)) at the start of the curve was applied to the fluorescence signal, where t_{dep} is the decay constant, $F(0)$ is the amplitude and F_{sat} is the offset of the curve (the fit was applied for the first 20 ms of measured data after shutter was completely opened, See Figure 3.2).

$$F(t) = F(0)\exp(t / t_{dep}) + F_{sat} \tag{3.31}$$

The offset of F_{sat} corresponds to the steady state fluorescence signal level.

Where no decay is visible (low power) we used the average value, for higher powers eq.(3.31) is applied to get F_{sat} (See Figure 3.2).

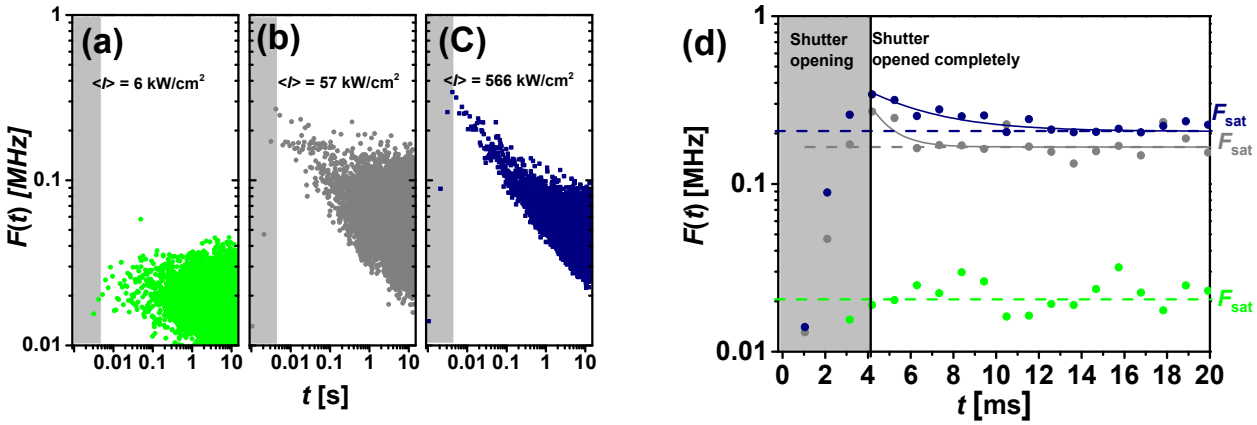

Figure 3.2. Fluorescence signal decay, $F(t)$ of Cy5 in phosphate buffer/air conditions measured at different excitation powers. For (a) $\langle I \rangle$ = 6 kW/cm^2 (green dots) no bleaching is observed, average value is taken. (b) $\langle I \rangle$ = 57 kW/cm^2 (gray dots) and (c) $\langle I \rangle$ = 566 kW/cm^2 (blue dots) the mono-exponential fit (eq.(3.31)) permit to obtained the fluorescence signal without bleaching The grey box indicates the time at the beginning of signal measurements, where the sample is already excited, but the shutter is still not completely opened.

In general the fluorescence signal can be calculated according to eq.(3.32)

$$F_{cpm} = G_{Detect} k_F S_{1eq} \tag{3.32}$$

where G_{Detect} is the detection efficiency of the fluorescence setup, k_F is the rate constant of fluorescence (reciprocal radiative lifetime) and S_{1eq} is the steady-state population probability of S_1 state.

The maximal achievable fluorescence signal F_{cpm_max} can be calculated by using a 2-level model where fluorescence quantum yield is defined as $\Phi_F = k_F / k_0$:

$$F_{cpm\_\max} = G_{Detect} \Phi_F k_0 S_{1eq}^2 \tag{3.33}$$

The substitution of k_F with $\Phi_F k_0$ permits to use the experimental fluorescence quantum yield of Cy5, Φ_F = 0.30 in buffer and 0.36 in EtOH. The reciprocal fluorescence lifetime was measured by TCSPC giving $k_0 = 9.8\times10^8$ s^{-1} in buffer and $k_0 = 7.9\times10^8$ s^{-1} in EtOH (See S9).

For the calculation of S^2_{1eq} eq.(3.34) was used:

$$S_{1eq}^2 = \frac{k_{01}}{k_{01} + k_F + k_{IC}} \tag{3.34}$$

Then F_{cpm} is calculated according to eq. (3.35)

$$F_{cpm} = G_{Detect} \Phi_F k_0 S_{1eq}^5 F_{eq} \tag{3.35}$$

where $S^5_{1\mathrm{eq}}$ is defined by eq. (3.21), F_{eq} by eq. (3.26)

k_0 is described for our model in Figure 3.1 with eq.(3.36):

$$1/k_0 = 1/(k_F + k_{IC} + k_{ISC} + k_{ISO} + k_{qS}[Q]) \tag{3.36}$$

where k_{F}, k_{IC}, k_{ISC}, k_{ISO} and k_{qS} are the depopulation rate constants of S_1 by fluorescence emission, internal conversion, intersystem crossing, isomerization and singlet quenching respectively.[160]

However, in our experiments we observed saturated fluorescence signal F_{sat}:

$$F_{sat} = G_{Detect} \Phi_F k_0 S_{1eq}^5 F_{eq} N_{tot} \tag{3.37}$$

Therefore fluorescence count rate per molecule F_{cpm} is defined by using eq.(3.29): $F_{cpm} = F_{sat} / N_{tot}$.

In FCS measurements, only measurements at low power ($\langle I \rangle$ = 2-85 kW/cm^2) were included in the analysis. In the signal measurements we analyzed till the excitation irradiance of $\langle I \rangle$ = 550 kW/cm^2. Therefore we can't neglect the effect of irreversible photobleaching (See Figure 3.2) in fluorescence signal analysis as we have done for FCS data analysis (too small to be detected).

When bleaching is involved we have additionally to consider a fraction of bleached molecules (P) by calculation of F_{cpm}, eq.(3.38).

$$F_{cpm} = \frac{F_{sat}}{N_{tot}(1-P)} \tag{3.38}$$

The composite rate constant for the irreversible photobelaching is defined[160]:

$$k_{btot} = k_{bS} S_{1eq} + k_{bT} T_{1eq} + k_{bR} R_{eq} = (k_{bS} + k_{bT} \frac{k''_{ISC}}{k_T} + k_{bR} \frac{k_{oxtot}}{k_{red}}) S_{1eq} = k_{bF} F_{eq} + k_{bR} R_{eq} \tag{3.39}$$

where k_{bS}, k_{bT} and k_{bR} are the bleaching rate constants from singlet, triplet and radical states (See Sec.3.3.3).

Assuming k_{btot} does not influence equilibrium conditions between R and F but "slowly" reduces the stationary populations of both species.

In the case of irreversible photobleaching reaction, the equilibrium state means formally that all molecules are bleached. Because of that, we can't assume the equilibrium state conditions. Hence, we need to define the start condition to be able to find analytical or numerical solution for our kinetics scheme. At the same time, in the beginning of our signal measurements before the shutter was completely open (Figure 3.2) the bleaching already starts (first 4 milliseconds of measurements). This doesn't allow us to define the starting conditions for kinetics precisely. Because of that, there is no simple exact solution for description of bleaching process in our signal measurements. By our analysis we assumed, that the fraction of bleached molecules P is proportional to the rate of their formation (eq. (3.40))

$$P = \eta_{bleach} \cdot k_{btot} \tag{3.40}$$

The proportionality factor η_{bleach} combines properties of our setup (shape and strength, of excitation irradiance, shutter speed) with kinetic parameters of the dye. Hence in the data fit of saturation curves the parameter η_{bleach} was left free for every single saturation curve.

An example of saturation curve for Cy5 in air saturated buffer where η_{bleach} is fixed to 0 show that the fit is not possible (See S6). To prove our assumptions we performed the numerical simulations of Cy5 without quencher, where we put all kinetic parameter which where estimated by FCS, saturation curve analysis and steady state bleaching (See S4, Figure S19).

3.2.3.4 Photobleaching

The photobleaching experiments were conducted at low irradiance, consequently all possible reactions that compromise the fluorescence emission process, involve the first excited singlet states (*trans* S_1 and *cis* S_1), triplet (T_1) and the radical state ($R^{\bullet+}$). The complete description of photobleaching processes is in ref.[160, 163]

The individual bleaching rate constants of the singlet, triplet, and radical state can be modulated by adding different chemical quenchers in to the solution and varying the concentration of them or using Cy5 conjugated with a quencher. Also use of different solvents and the presence of oxygen are crucial in the photostability of the dye.

In the experimental point of view, in the cell-bleaching experiments we measured the time-dependent decrease of the fluorescence, $F(t)$ of an illuminated and stirred dye solution:[160]

$$F(t) = F_0 \exp(-k_z \cdot t) \tag{3.41}$$

The microscopic photobleaching constant rate k_b is given by eq.(3.42):

$$k_b = \frac{\Phi_b}{\tau_0} \tag{3.42}$$

where Φ_b is the quantum yield of photobleaching, τ_0, is the fluorescence lifetime. It should be noted that for our measurements we use species-averaged fluorescence lifetime $\langle\tau\rangle_x$ (See S7).

The quantum yield of photobleaching is described by eq. (3.43)

$$\Phi_b = \frac{V \cdot k_z}{\sigma_{01} \cdot \gamma \cdot b_c \cdot L} \tag{3.43}$$

where σ_{01} is the absorption cross-section of the dye molecules, b_c is the optical path length of the bleaching cell, L is the excitation power, γ is the inverted photon energy and V the solution volume. Taking into account the fluorescence quantum yield we can calculate the number of photons (N_F) according to eq. (3.44)[160, 163]

$$N_F = \frac{\Phi_F}{\Phi_b} \tag{3.44}$$

As already reported in ref.[160] for Rhodamine dye, adsorption-desorption equilibrium of the dye molecules to the cuvette surface is present. Therefore, the kinetic of the photobleaching reaction can be written in the following form:

$$c_{ad} \underset{k_{ads}}{\overset{k_{des}}{\rightleftharpoons}} c_{solv} \xrightarrow{k_z} \text{Bleached dye, } c_b \tag{3.45}$$

Such kinetic scheme can be described by two exponentials terms:

$$c_{solv}(t) = a_1 \exp\left(-\frac{t}{\tau_{b1}}\right) + a_2 \exp\left(-\frac{t}{\tau_{b2}}\right) \tag{3.46}$$

This approach was used also to the analysis Cy5 data measured in air saturated solution for both solvents and in EtOH under argon, where k_z can be easily extracted from the amplitudes a_2 and

rate constant $k_z = 1/\tau_{b2}$. In such measurements we obtain bi-exponential decays where small fraction (<10%) corresponds to the adsorption-desorption kinetics.

Once k_z is obtained, it is possible to calculate Φ_b using eq.(3.43) and therefore also calculating k_b for each set of experimental conditions eq.(3.42).

In buffer under argon, we observed complicated bleaching kinetics pathways via fluorescent intermediates and photo protective photobleaching products. A detailed examination of this kinetics of photo-oxidizing and bleaching intermediates is beyond the scope of this paper.

3.3 Results and discussion

The Cy5-conjugates were produced by organic synthesis and characterized with mass spectroscopy and NMR. The purification was done with silica gel column chromatography and HPLC. For details See S1.

3.3.1 Ensemble Spectroscopy

We characterized the absorption and fluorescence properties of Cy5 and Cy5-Q in phosphate buffer (Na_2HPO_4/NaH_2PO_4) 20 mM, pH 7 and in ethanol. The spectra are reported in S8.

Table 3.2 summarizes the results regarding absorption, emission and excitation spectra, as well steady state fluorescence quantum yield and species-averaged fluorescence lifetime $\langle\tau\rangle_x$ for Cy5 and Cy5-Q in phosphate buffer, 20 mM, pH 7 and in ethanol.

	Phosphate Buffer					**EtOH**				
	$\lambda_{max,abs}$ [a] **[nm]**	$\lambda_{max,ex.}$ [a] **[nm]**	$\lambda_{max,em.}$ [a] **[nm]**	Φ_F [b]	$\langle\tau\rangle_x$ [c] **[ns]**	$\lambda_{max,abs}$ [a] **[nm]**	$\lambda_{max,ex.}$ [a] **[nm]**	$\lambda_{max,em.}$ [a] **[nm]**	Φ_F [b]	$\langle\tau\rangle_x$ [c] **[ns]**
Cy5	649	646	665	0.30±0.008	1.02	656	654	672	0.36±0.013	1.26
Cy5-AZB-C	651	648	664	0.06±0.002	0.22	655	653	674	0.34±0.010	1.22
Cy5-Trolox	650	649	665	0.21±0.07	0.73	654	652	673	0.31±0.011	1.01

Table 3.2. [a]Maximum wavelengths in absorption, excitation and emission spectra (See S8). [b]Fluorescence quantum yield (with standard errors of four measurements). For the analysis method see Section 3.2.3.1, Rhodamine 700 in ethanol was used as reference with $\Phi_{F,R} = 0.38$.[147] [c]Species-averaged fluorescence lifetime (See S7) of Cy5, Cy5-AZB-C and Cy5-Trolox in buffer and in ethanol.

In buffer and in ethanol, maximum wavelengths of absorption, excitation and emission are almost identical for the three compounds, but as expected a bathochromic effect between the two solvents is noticeable (see Figure S23).

In aqueous solution, the fluorescence quantum yields and fluorescence lifetimes of Cy5-Q are much lower in comparison to Cy5 free dye. For Cy5-Trolox is ≈ 1.4 times lower and for Cy5-AZB-C ≈ 5 times lower in comparison to Cy5 free dye. One possible explanation is, that it is attributed to the singlet quenching due to the high formal local concentration of the quencher. Such parameter is determined with global fit analysis (See S9) for different experimental conditions. The formal local concentration has no physical meaning, is a technical way to treat the process.

The solvent significantly changes the fluorescence quantum yields and lifetimes. For Cy5 free dye the value obtained in ethanol is higher in comparison to buffer conditions. Such effect is more significant for Cy5-Q, where the quantum yield increases dramatically and approaches the value of the free dye. The fluorescence quantum yield ratio between Cy5 free dye and Cy5-Trolox is ≈ 1.2 and for Cy5-AZB-C ≈ 1.06. Such behavior is observed also in lifetime experiments (See Table 3.2).

It is known, that solvent polarity influences the absorption and the fluorescence properties of the dyes. Application of the theory for general solvent effects is often inadequate when detailed behavior of fluorophores in a variety of environments is of interest.[164, 165 163] The fluorescence quantum yield and the triplet quantum yield is often critically solvent dependent. In general, the photostability of many organic dyes in organic solvents is higher than in water.[133, 166] For the specific case of cyanine dyes, it was reported that viscosity is the dominating solvent property affecting the isomerization kinetics at room temperature,[23, 155, 167-169] and the effect of polarity of the solvent is very small.[170, 171]

The Stern-Volmer analysis of fluorescence intensity and fluorescence lifetime is displayed in the Figure 3.3. For both quenchers the ratio (F_0/F) / $(\langle\tau\rangle_{x,0}/\langle\tau\rangle_x)$ is equal to 1 (± 5% within the experimental error), proving that dynamic quenching is the dominating process.

The dynamic quenching constant $k_{q,D}$ for Trolox is higher in comparison to AZB-C and it is very close to the diffusion controlled rate constant, that it is $5.4 \cdot 10^9$ $M^{-1}s^{-1}$ in ethanol.[172] Values of k_{qD}

smaller than the diffusion-controlled value can result from steric shielding of the fluorophore or a low quenching efficiency.[146]

(a) **(b)**

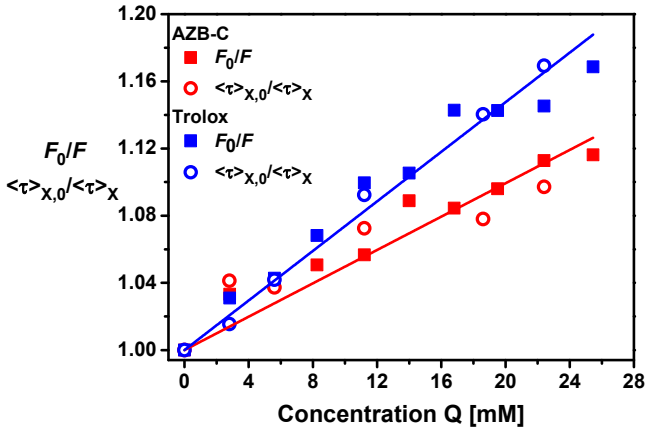

Q	$\langle\tau\rangle_{x,0}$ [ns]	K_D [M^{-1}]	$k_{q,D}$ [$M^{-1}s^{-1}$]
AZB-C	1.26	4.03	$3.20 \cdot 10^9$
Trolox	1.26	6.85	$5.44 \cdot 10^9$

Figure 3.3. Stern-Volmer quenching analysis in EtOH (a) Ratio of fluorescent intensity without quencher (F_0), lifetime ($\langle\tau\rangle_{x,0}$) and fluorescent intensity with quencher (F), lifetime ($\langle\tau\rangle_x$) at different concentrations for Trolox (blue markers) and AZB-C (red markers) in ethanol. The lines represent the linear fits for the two quenchers. (b) Results of the fits for Trolox and AZB-C are summarized in the Table.

3.3.2 Redox potentials

In order to investigate the electron transfer reactions involved, we calculated free energies (ΔG^0) for each process. We applied eq.(3.7) using redox potentials of Cy5 (data from ref.[26]), redox potentials of quenchers (measured by cyclic voltammetry[55]), redox potentials of O_2 (data from ref.[173]) and S_1 and T_1 energies of Cy5 (data from ref.[26, 174]).

	ΔG^0 (electron transfer) / eV						E_{ox}	E_{red}	E_S	E_T
	Reduction of Cy5			Oxidation of Cy5			[V] vs. NHE		eV	
	S_1	T_1	$R^{\bullet+}$	S_1	T_1	$R^{\bullet-}$				
Cy5	---	---	---	---	---	---	1.21[a]	-0.60[a]	1.88[d]	1.60[d]
Trolox	-0.88	-0.60	-0.81	0.15	0.43	0.22	0.40[b]	-0.82[b]	---	---
AZB-C	0.78	1.06	0.85	0.14	0.42	0.21	2.06[b]	-0.81[b]	---	---
O_2	-0.05	0.23	0.02	-0.34	-0.06	-0.27	1.23[c]	-0.33[c]	---	---

Table 3.3. ΔG^0 values of the reductive and oxidative electron transfer between quencher, O_2 and S_1, T_1 and the radical of Cy5 calculated according to eq. (3.7). [a]Redox potentials of Cy5,[26] [b]redox potentials of quenchers,[55] [c]redox potentials of O_2[173] and S_1 and T_1 energies of Cy5.[26, 174]

Theoretically, according to our results, listed in Table 3.3, there are three classes of reactions:

1. $\Delta G^0 < 0$ exergonic reaction
2. $\Delta G^0 \approx 0$ where the usage of protic solvents (H_2O) could shift the free energies to negative values due to the proton transfer[175]
3. $\Delta G^0 > 0$ endergonic reaction

For exergonic reactions, Trolox can reduce S_1, T_1 and $R^{\bullet+}$ states and in addition, radical cation formation via photo-oxidation by oxygen is possible. The reactions that might occur ($\Delta G^0 \approx 0$) are oxidation of S_1 and $R^{\bullet-}$ by Trolox and AZB-C. The rest of reactions are endergonic.

From our experimental data we found that Trolox has triplet and singlet quenching effect but no effect in the radical term is visible.

In contrary, AZB-C has triplet quenching effect by energy transfer (not visible in the table) and also surprisingly effect on the radical quenching (See Section 3.3.4).

Taking in account that the redox potentials are measured in DMF, the data are not completely comparable with our experimental conditions.

3.3.3 Photobleaching

For the photobleaching of Cy5 we investigated the combination of three factors:

- presence of oxygen,
- nature of the solvent (buffer / EtOH),
- usage of additives or employment of Cy5-conjugates.

The Figure 3.4 shows different behavior of the dye in buffer, depending on whether it is in air saturated conditions or in argon environment. For clarity reasons, the curves for the Cy5-conjugates were rescaled with respect to the fluorescence quantum yield of the free dye.

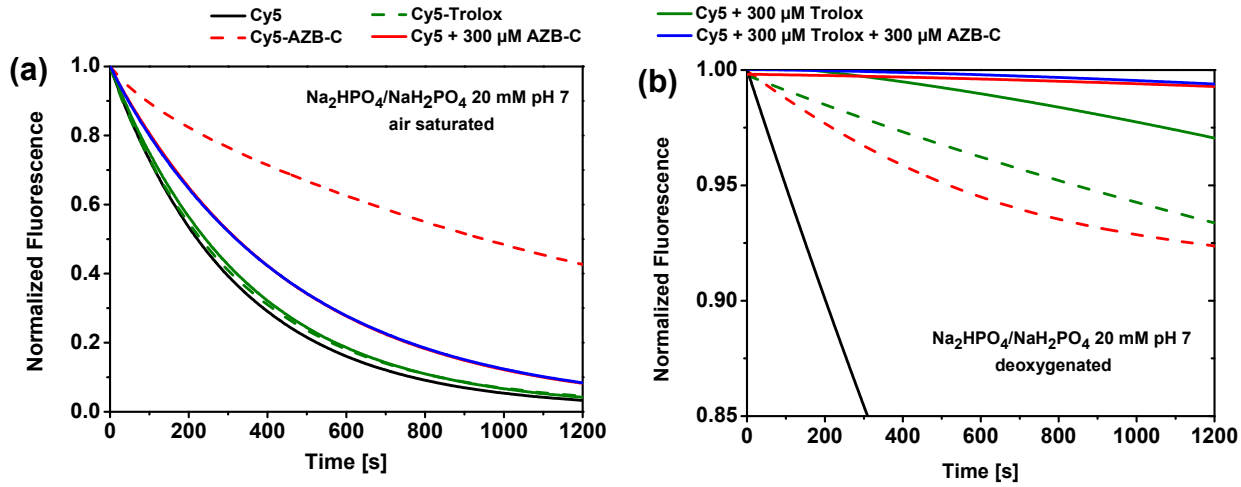

Figure 3.4. (a)Photobleaching curves for free Cy5 and Cy5-conjugates in air saturated buffer. (b) Photobleaching curves for Cy5 and Cy5-conjugates in buffer under argon.

In air saturated buffer Cy5 has the tendency to degrade very fast (Φ_b=3.1E-6), the removal of oxygen makes the dye more stable (Φ_b~5E-7). Notably, addition of quenchers or usage of the conjugated compounds improved the photostability of Cy5. Cy5-AZB-C is the best way to stabilize Cy5 in air saturated buffer (Φ_b=1.3E-7). In aqueous solution under argon the free dye gets very stable and the usage of additives or conjugated compounds improves its photostability even further. Our values of Φ_b for Cy5 free dye are in the same order of magnitude of Rhodamine dyes obtained in air saturated water from Eggeling and co-authors.[160]

In contrary, Cy5 in air saturated EtOH (Φ_b=1.9E-8) is more stable without any additives or conjugated quenchers. One possible explanation could be attributed to a formation of new intermediates which open new photobleaching paths.

The stability of Cy5 free dye is the highest in EtOH solution without oxygen (Φ_b=2.8E-9). In EtOH under argon, the usage of quenchers in solution and Cy5-AZB-C permit to gain stability, only Cy5-Trolox is more inclined to faster degradation.

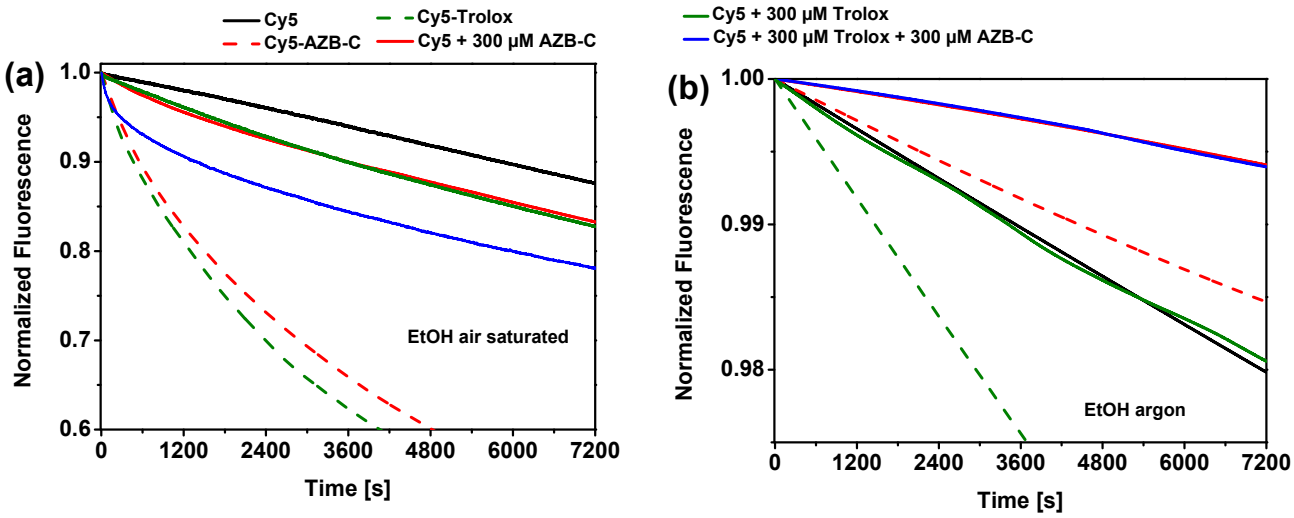

Figure 3.5. (a) Photobleaching curves for Cy5 and Cy5-conjugates in air saturated EtOH (b) Photobleaching curves for Cy5 and Cy5-conjugates in EtOH under argon.

In the Table 3.4 the quantitative results of photobleaching (k_b) are shown. We considered a five level system for air saturated in both solvents and for EtOH under argon. The values of k_b are calculated using eq. (3.41-3.43) taking in account the different fluorescence lifetime (τ_0) for Cy5 free dye and for Cy5-Q in the two different solvent. It should be noted that our τ_0 is species-averaged fluorescence lifetime $\langle\tau\rangle_x$. In buffer under argon the data look complicated, permitting to give only an estimation of the k_b values. A multi-exponential fits was used in order to obtain averaged values.

			In air saturated										In argon									
	Quencher		Buffer					EtOH					Buffer					EtOH				
	AZB-C in solution [μM]	Trolox in solution [μM]	k_b[a] [s^{-1}]	N_F[b] 10^6	Φ_b[c] 10^{-8}	τ_0 [ns]	Φ_F	k_b[a] [s^{-1}]	N_F[b] 10^6	Φ_b[c] 10^{-8}	τ_0 [ns]	Φ_F	k_b[a,d] [s^{-1}]	N_F[b,d] 10^6	Φ_b[c,d] 10^{-8}	τ_0 [ns]	Φ_F	k_b[a] [s^{-1}]	N_F[b] 10^6	Φ_b[c] 10^{-8}	τ_0 [ns]	Φ_F
Cy5	**0**	**0**	**3064**	**0.097**	**310**	**1.02**	**0.30**	**15**	**18.9**	**1.9**	**1.26**	**0.36**	**~ 500**	~0.6	**~50**	**1.02**	**0.30**	**2.2**	**129**	**0.28**	**1.26**	**0.36**
Cy5	300	0	2121	0.136	220	1.02	0.30	17	17.1	2.1	1.26	0.36	~5	~60	~0.5	1.02	0.30	0.37	766	0.047	1.26	0.36
Cy5	0	300	2807	0.103	290	1.02	0.30	17	17.1	2.1	1.26	0.36	~10	~30	~1	1.02	0.30	1.5	189	0.19	1.26	0.36
Cy5	300	300	2000	0.150	200	1.02	0.30	15	18.9	1.9	1.26	0.36	~5	~60	~0.5	1.02	0.30	0.99	300	0.12	1.26	0.36
Cy5-AZB-C	**0**	**0**	**611**	**0.462**	**13**	**0.22**	**0.06**	**31**	**9.0**	**3.8**	**1.22**	**0.34**	**~30**	~2	**~3**	**0.22**	**0.06**	**1.5**	**189**	**0.18**	**1.22**	**0.34**
Cy5-Trolox	**0**	**0**	**3076**	**0.096**	**220**	**0.73**	**0.21**	**28**	**12.9**	**2.4**	**1.01**	**0.31**	**~15**	~14	**~1.5**	**0.73**	**0.21**	**7.1**	**221**	**0.14**	**1.01**	**0.31**

Table 3.4. Photobleaching results in air saturated buffer/EtOH and under argon buffer/EtOH. [a] Photobleaching rate constant, k_b (eq. (3.42)), [b] number of photons, N_F (eq. (3.44)), [c] quantum yield of photobleaching, Φ_b (eq. (3.43)). τ_0 is the fluorescence lifetime and Φ_F the fluorescence quantum yield used for the calculation of k_b and N_F. [d] Complex multiexponential photobleaching curve, therefore for buffer under argon unweighted average of k_b and Φ_b values are calculated, here they are shown only for reference.

Under air saturated conditions, the photostability (measured via Φ_b) is 200 times higher in ethanol than in buffer. Without oxygen and any additives, we see the same difference of 200 times between ethanol and aqueous solution. If quenchers are used under argon conditions then the dye is 10 times more stable than in ethanol. In general, in ethanol the bleaching rate constants are smaller than in aqueous solution. Such behavior could be attributed to the negligible amount of ionic and radical species present in the organic solvent. Indeed, ethanol is not able to stabilize charges like water, due to its lower dielectric constant.

In ethanol the photostability without oxygen is 10 times higher than in air saturated ethanol. The photostability of Cy5 without quenchers in buffer and without oxygen is 6 times higher than in buffer under air saturated condition. If quenchers are used the photostability under argon condition is 200 times higher than in air saturated buffer.

AZB-C in buffer under air saturated conditions increases the photostability. The biggest effect is observed if Cy5-AZB-C is used, where the photostability is improved 5 times with respect to the free Cy5. Trolox does not change photostability of Cy5 in buffer under air saturated conditions.

In buffer under argon the addition of any kind of quenchers leads to improvement of about 50 times. In ethanol where in general the bleaching is very slow we see no effect of quenchers.

The trends shown for the photobleaching rate constants k_b is also reflected in number of photons, N_F for the different environments and solvents. Indeed, using eq. (3.44) we can calculate the average number of photons (N_F) emitted by a single dye before bleaching occurs. For Cy5 without quencher in air saturated buffer we obtain $N_F \approx 1 \bullet 10^5$ photons. The best improvement of photostability in air saturated buffer we achieved using Cy5-AZB-C conjugate, where $N_F \approx 5 \bullet 10^5$ photons. The highest photostability we observed in ethanol under argon if Cy5-AZB-C conjugate was used resulting in $N_F \approx 2 \bullet 10^8$ photons before bleaching, which is 2000 times more in comparison to dye in air saturated aqueous solution.

In air saturated buffer, Cy5-AZB-C shows triplet amplitude close to 0 and the radical state is totally suppressed (See FCS results, Figure 3.9a). Thus, bleaching observed for Cy5-AZB-C under this condition comes from singlet state, according to eq. (3.39) $k_{bs} \approx 600\ s^{-1}$. As was already reported[28, 31], oxygen is the main source for bleaching reaction via singlet state under air saturated conditions. At the same time, due to our FCS measurements under argon condition only singlet and triplet states were present (See 3.3.4). Thus, we can assume that triplet state represents the main pathway of the bleaching reactions in experiments under buffer argon

conditions. The bleaching constant for the dye in buffer under argon is $k_{btot} \approx 500\ s^{-1}$ for Cy5 without quenchers. Using eq. (3.39), it is possible to get a rought estimate on $k_{bT} \approx 20\ s^{-1}$ (assuming k_{bS} and $k_{bR} \approx 0$). In air saturated buffer we measured $k_{btot} \approx 3000\ s^{-1}$ by using eq. (3.39) it is possible to calculate bleaching constant of radical state, k_{bR} is $\approx 235\ s^{-1}$.

3.3.4 Fluorescence correlation spectroscopy (FCS) and fluorescence signal (F_{cpm})

Using FCS we investigated the impact of (i) the solvent, (ii) the excitation power and (iii) the addition of quenchers or the usage of dye-conjugates on the photophysics of Cy5 in air saturated solution and in argon environment.

Solvent effect

Here we show FCS curves for Cy5 in air saturated solution in different solvents but with the same power density: 14 kW/cm^2.

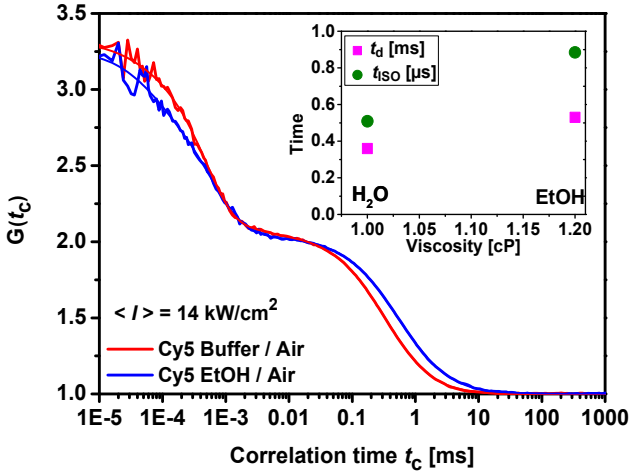

Figure 3.6. FCS curves of Cy5 and respective single fits using eq. (3.8) at $\langle I \rangle = 14$ kW/cm^2, red line for air saturated buffer and blue line for air saturated EtOH. Inset: diffusion time (t_d) and isomerization time (t_{ISO}) vs. viscosity of H_2O (1 cP) and EtOH (1.2 cP) at 20°C.[35]

At power density = 14 kW/cm^2 the curves are fitted with diffusion time, triplet and isomerization term, no radical term is present. The main differences are observed in the isomerization time and in diffusion time. Such effect can mainly be attributed to the different viscosities of the solvents. It was already reported in literature[23, 35, 155, 167-169] that the viscosity is the most important property affecting the isomerization process, in contrary the polarity shows very small effect. Indeed, in ethanol the fits show longer diffusion time and isomerization time.

Excitation power dependence (up to 85 kW/cm^2)

The Figure 3.7 shows the fluorescence correlation curves of Cy5 for four examples of excitation irradiances in air saturated buffer and in EtOH. The global fit analysis was done with 13 different excitation irradiances in the range from 2 kW/cm^2 to 85 kW/cm^2. Once the rate constants regarding the fast processes were obtained ($\langle I \rangle$ =2-34 kW/cm^2), we performed the second global fit analysis for the highest powers where the radical term is present. In the second fit, parameters we got from the first analysis were fixed. Such procedure was applied for Cy5 in different experimental conditions and for Cy5 conjugated compounds.

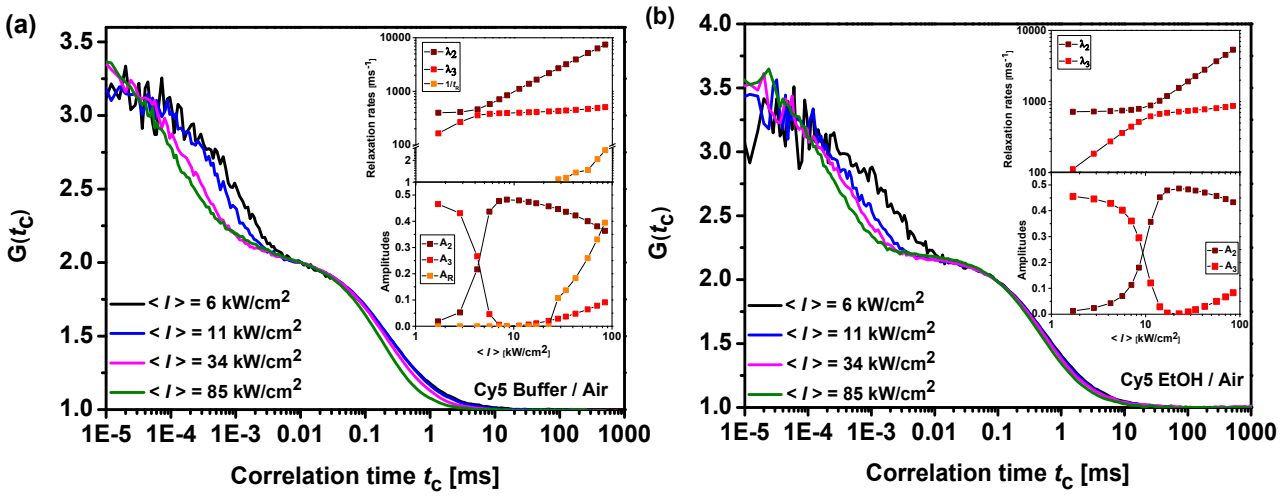

Figure 3.7. (a) FCS curves of Cy5 in air saturated buffer at four different excitation irradiances. Inset: global fit analysis results of relaxation rates and amplitudes of fast processes, eq.(3.8-3.18), fixed parameters are k_0=0.98·10^9 s^{-1} and σ=7.46·10^{-16} cm^2 and for radical process, eq. (3.8-3.26) with fixed parameters k_{ISO}, k_{ISC} and k_T. (b) FCS curves of Cy5 in air saturated EtOH at four different excitation irradiances. Inset: global fit analysis results of relaxation rates and amplitudes of fast processes, eq.(3.8-3.18), fixed parameters are k_0=0.79·10^9 s^{-1} and σ=5.31·10^{-16} cm^2. Rate constants results are summarized in Table 3.5.

By using single fits, the distinction of the two fast processes (triplet and isomerization) is not completely possible since relaxation rates and amplitudes are coupled together over the whole excitation range.[35] Thus, the global fit analysis is the most appropriate approach, permitting to obtain the photophysical parameters for different experimental conditions and samples.

In air saturated aqueous solution with the power > 34 kW/cm^2 formation of the radical state is visible. In EtOH, $R^{\bullet+}$ is not present. The aqueous solution and ethanol are different in terms of: (i) solubility of O_2, (ii) viscosity and (iii) different dielectric constant. The diversity in such

features reflects the difference in the formation and stabilization of the radical species (Table 3.5).

	Solvent	k_{ISO} [a] [10^6 s^{-1}]	k_{ISC} [a] [10^6 s^{-1}]	k_T [a] [10^6 s^{-1}]	k_{ox} [b] [s^{-1}]	k_{red} [b] [s^{-1}]	k_{oxn} [cm^2 $W^{-1}s^{-1}$]
Cy5	Buffer	15.7	1.10	0.43	2500	250	0
	EtOH	12.9	1.90	0.71	0	0	0

Table 3.5. Results of global fit analysis for Cy5 in air/buffer and air/EtOH of FCS curves with different irradiances. [a]Rate constants results for fast components from FCS curves with $\langle I \rangle \leq 34$ kW/cm^2 using eq. (3.8-3.18). [b]Rate constants results of radical term from FCS curves with $\langle I \rangle >$ 34 kW/cm^2 where k_{ISO}, k_{ISC} and k_T are fixed values using eq. (3.8-3.26). For other conditions See S9.

The photo-oxidation and reduction rate constants are quite imprecise numbers; here the average values are given. Taking a fixed value for k_{ox} with in the range of 2500±1500 s^{-1} results in a fit with the same quality as long as the ratio between k_{ox} and k_{red} stays equal to 10.

For Rhodamine dyes, the oxidation from the higher excited states in the range of k_{oxn}=0.004-0.002 cm^2 $W^{-1}s^{-1}$ was reported[160, 161]. For Cy5 k_{oxn} is not needed. However, taking a fixed value for k_{oxn} in the rage of 0-0.001 cm^2 $W^{-1}s^{-1}$ had no influence on fit quality.

In the limit of our precision of our data analysis, bleaching kinetics could influence estimated parameters for radical formation. The interchange between these two processes could cause a possible overestimation of the oxidation rate constant.

Diffusion times of Cy5 in different conditions are shown in S10. The radical term is present only in air/buffer environments. In the other conditions where no radical is present, as expected due to the saturation effects an increase of the diffusion times with the power is visible. For FCS curves of Cy5 conjugated compounds see S11.

Quenchers effect in air saturated solution

The third aspect that we studied is the influence of quenchers on the photophysics of Cy5. We tested additives in solution in buffer/ethanol and in air/argon. Moreover, we performed the same experiments with our Cy5-conjugates in different environments. Once obtained the rate constants for Cy5 free dye (See Table 3.5 and Table S3) these values were fixed in the global fits to obtain the rate constants for triplet and radical quenching (k_{qT}, k_{qox} and k_{qred}).

The FCS global fit analysis at different power excitations (with $\langle I \rangle \leq 34$ kW/cm^2) and different concentrations of additives was applied using eq.(3.19) for triplet and singlet states as follows: $k'_T = k_T + k_{qT}[Q]$ and $k'_S = k_S + k_{qS}[Q]$. The values of k_{qS} (see results in Figure 3.3(b)) and k_T were fixed permitting to obtain the k_{qT} values for AZB-C and Trolox.

Also here a second run of global fit analysis was done for FCS curves with $\langle I \rangle$ >34 kW/cm^2 by fixing the parameters obtained for the fast processes (values in Table 3.5, Table S3, k_{qS} and k_{qT}). The second interaction permitted to obtain the rate constants regarding radical quenching for the reduction and oxidation processes using following equations: $k'_{red} = k_{red} + k_{qred}[Q]$ and $k'_{ox} = k_{ox} + k_{qox}[Q]$.

The rate constants for the quenchers are respectively:

Solvent	Quencher	k_{qS} [a] [10^9 M^{-1}s^{-1}]	k_{qT} [b] [10^9 M^{-1}s^{-1}]	k_{qred} [c] [10^6 M^{-1}s^{-1}]	k_{qox} [c] [10^6 M^{-1}s^{-1}]
Buffer	AZB-C	3.20	0.356	1.57	9.81
	Trolox	5.44	0.0981	0	0
EtOH	AZB-C	3.20	0.317	0	0
	Trolox	5.44	0.0876	0	0

Table 3.6. Quenching rate constants for singlet, triplet and radical state of Cy5 in air saturated buffer and EtOH. [a]From Figure 3.3b, [b]results of global fit analysis of FCS curves with $\langle I \rangle \leq 34$ kW/cm^2 with different concentrations of quenchers and fixed rate constants given in Table 3.5 and k_{qS}, [c] results of global fit analysis of FCS curves with $\langle I \rangle$ >34 kW/cm^2 with different concentrations of quenchers and fixed rate constants given in Table 3.5, k_{qS} and k_{qT}.

Due to the poor solubility of the quenchers in aqueous solution the determination of k_{qS} was possible only in ethanol (See Figure 3.3b). For buffer conditions we assume the same rate constants.

For Cy5-conjugates the data were fitted with the apparent local concentration set to be free parameter and fixed k_{qT} and k_T to Cy5 free dye values (for results See S9).

The mechanism of quenching by Trolox is still under debate. It is not totally clear if the working principle of Trolox is by electron transfer, by Dexter energy transfer or the combination of both processes. Indirect evidences show that Trolox is able to reduce the blinking of Cy5 when enters the transient nonfluorescence states in free oxygen solution.[137] These findings made the authors conclude that Trolox is able to quench the triplet state.[29, 138, 159] Moreover, literature reported that

Trolox in combination with its oxidized state (Trolox quinone) is still able to efficiently eliminate blinking due to triplet states and also due to radical ion states[26, 27, 136]. Indeed, using reducing and oxidizing agents simultaneously leads to rapid depopulation of triplet states via electron transfer and quickly recovers the formed radical ions through the complementary redox reaction.[137]

In the self-healing scenario is assumed that Trolox first serves as a reductant for the triplet state. Then, the Trolox radical cation formed reacts with the dye in the radical anion state in a reverse electron transfer.[140] Other studies by transient absorption spectroscopy reported that dsDNA-Cy5-Trolox has very small effect on the triplet state showing that Trolox is a weak triplet quencher.[30] Since in our FCS experiments we have seen the weak shortening of the triplet time by adding Trolox, there could be compensating effects. The combination of oxygen depletion with weak triplet quenching, given by the addition of Trolox is the most reasonable explanation.

We employed also single molecule detection (SMD) experiments on freely diffusing FRET-labeled molecule in solution in order to demonstrate how Trolox affects the photophysical stability of the Cy5 at different power (data not shown) in dsDNA. The measurements were conducted at two power regimes at the objective: 100 μW and 200 μW. Sample was measured in 20mM $MgCl_2$, 100mM KCl 20mM, K_2HPO_4/KH_2PO_4 buffer with 300 μM Trolox and without.

To get the quantitative overview how does the power at the objective and the presence of Trolox in the buffer solution affect photophysical stability of the Cy5 we performed photon distribution analysis (PDA) on the sm-FRET data.[176] As the sample has a predefined distance as predicted by accessible volume (AV) simulation[177], we could use PDA analysis in order to estimate how much donor fraction varies due to the acceptor photophysics. Indeed the experiment confirms that the donor only fraction increases in both solutions as the power at the objective was changed from 100 μW to 200 μW. Measurement at constant power but different solutions detect changes in donor only fraction. The fits support that in the Trolox solution acceptor reveals less acceptor quenching and more FRET occurs, leading to lower donor only fraction (61.9% in contrast to 80.7% for the measurement without Trolox for 200 μW). The fit results indicated that donor only fraction at 100 μW is lower than in any buffer at 200 μW. At 100 μW, presence of Trolox in solution results in a decrease of the donor fraction from 67.9% to 33.1%.

Differently, AZB-C is a moderate triplet quencher and also surprisingly it affects the radical term. The electron transfer analyses (See Section 3.3.2) show that the reduction of Cy5 by AZB-C involves endergonic reactions ($\Delta G^0 > 0$) and for the oxidation of Cy5 $\Delta G^0 \approx 0$. In the classical Marcus relation[178], the intermolecular quenching constant (k_q) depends on the two steps: (i) diffusion controlled formation/decay of encounter complex and (ii) activation-controlled rate of electron transfer.[179, 180]

The usage of protic solvent like H_2O (in our case buffer) could shift the free energies to negative values (gain of free energy between -0.5 and -0.9 eV)[175]. Indeed, for a specific dye its free energy could be shifted to large values in water solution as shown in ref.[175]. This permits for most of the dye/quencher combinations to have a positive electron transfer ΔG^0. Such behavior could also explain our positive ΔG^0 values that give origin of quenching processes like radical quenching through AZB-C.

We examine the effects caused by the additives quenchers in comparison to the effects of two conjugated compounds. We plot power density vs. count rate and show the occupancies of the states in air saturated buffer (Figure 3.8 and 3.9). In air saturated buffer bleaching is involved and the fraction of bleached molecules (P) has to be taken in account.

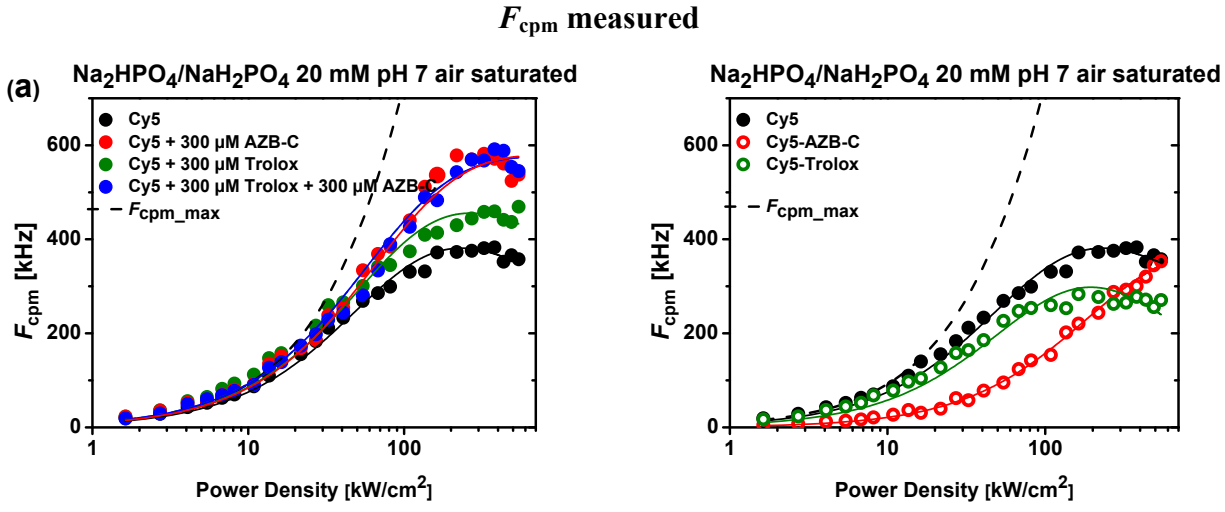

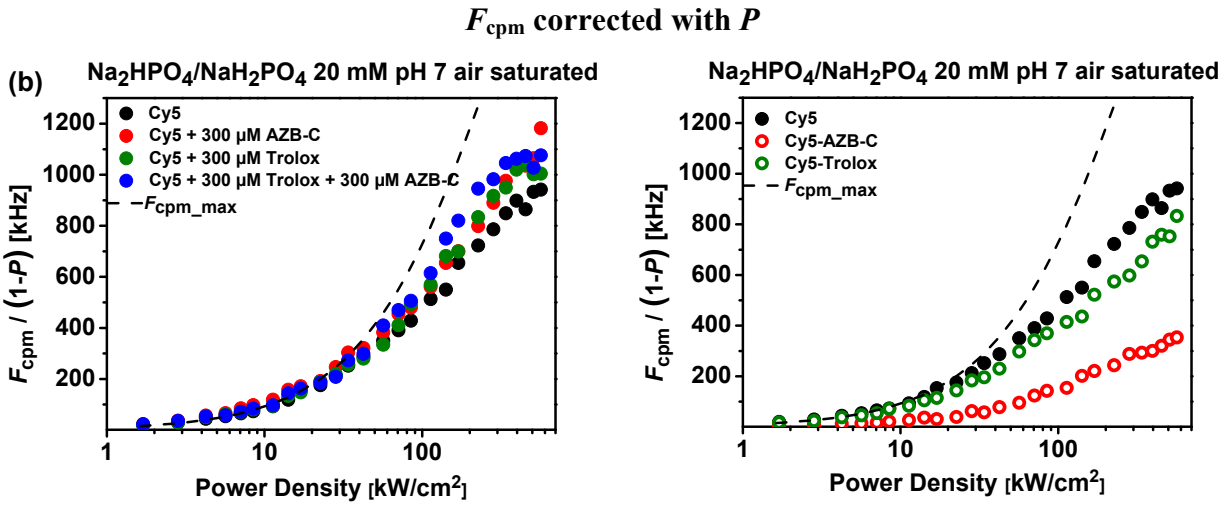

Figure 3.8. (a) Fluorescence signal at different power densities (points, eq.(3.29)) with their respective fits (lines) in air saturated buffer calculated according to eq.(3.9-3.28, 3.35, 3.39-3.40). Parameters used like fixed values: from Table 3.4 (k_b), for fast processes Table S3 (k_0, σ, σ_{BISO}, k_{ISO}, k_{ISC}, k_T), for quenchers Table 3.6 (k_{qS}, k_{qT} k_{qred} and k_{qox}) with k_{ox}=2500 s^{-1} and k_{red}= 250 s^{-1}. For fluorescence quantum yield (Φ_F) see Table 3.2, G_{Detect} is a free parameter for all fits (average value = 0.024 ± 0.002). Black dashed line: maximal achievable fluorescence signal eq. (3.33-3.34). (b) Fluorescence signal at different power densities in air saturated buffer calculated according to eq.(3.38) for additives and for Cy5-conjugates. Black dashed line: maximal achievable fluorescence signal eq. (3.33-3.34).

In Figure 3.8 the F_{cpm} signal "measured" (eq.(3.29)) and the signal recalculated using P (eq.(3.38)) is shown for Cy5 with additives and Cy5 conjugates. Unfortunately Cy5-conjugates do not show higher fluorescence signal than Cy5 due to the fact that such compounds have lower fluorescence quantum yield in comparison to Cy5. Moreover, comparing the occupancies of *trans* S_1 state (See Figure 3.9) and the F_{cpm} signal the same trend is visible. Maximum deviation between those two is about 15%, this is calculated using the ratio between Cy5 signal and Cy5+Q or Cy5-Conj. compared to the ratio in probabilities of *trans* S_1. Such findings suggest that obtained average values of k_{ox} and k_{red} are reasonable and therefore our model is able to predict the fluorescence signal.

In Figure 3.9 the occupation probabilities of the states and the fraction of P state are shown.

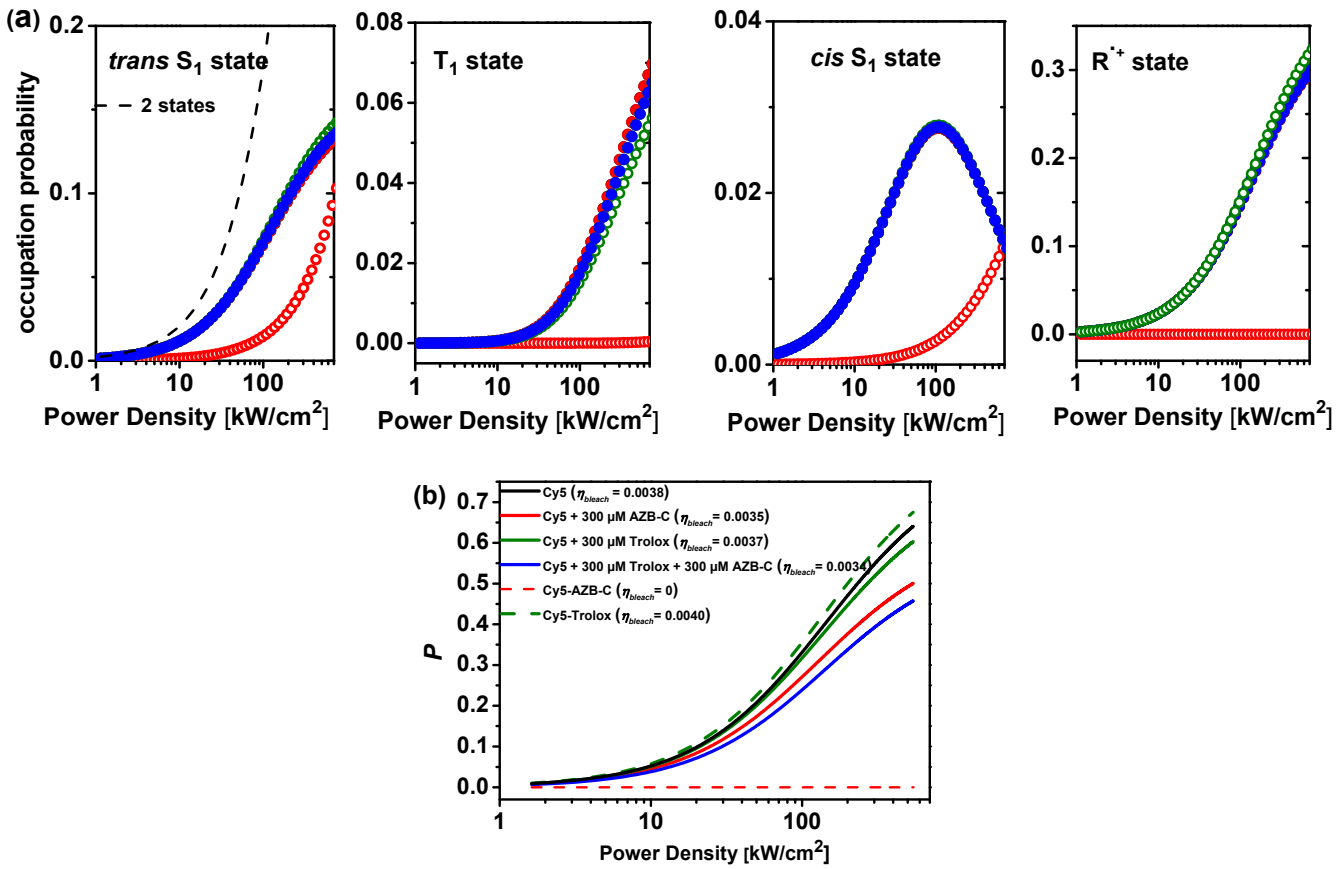

Figure 3.9. (a) Occupation probabilities for *trans* S_1 (black dashed line calculated with eq.(3.32)), T_1, *cis* S_1 and $R^{\bullet+}$ state. (b) Fraction of the *P* state (eq.(3.40)) for Cy5 + additives and Cy5-conjugates with η_{bleach} values obtained from the fits. For Cy5-AZB-C no *P* state is visible.

In such condition we observed that, as evident from the amplitudes of the states (see Figure 3.9a), the addition of AZB-C partially reduces the radical cation state, but at the same time it has small influence on the triplet state. The employment of Cy5-AZB-C due to the high formal local concentration of AZB-C is able to decrease the occupancy of the triplet state dramatically and suppress the production of radical state completely. Indeed, the occupancy of *trans* S_1 state increases with the radical quenching effect, Trolox additive shows very similar effect of Cy5 free dye. Trolox conjugate demonstrates slightly higher radical state occupancy compared to Cy5. This can be explained by the fact that we assume for simplicity that only singlet state could be oxidized in our model ($k_{oxT} \approx 0$).

In the Figure 3.9 (b) one can see the fraction of the *P* state for Cy5 (max ≈ 0.6). Cy5 with additives has influence on the *P* state fraction. Data analysis shows that Cy5-AZB-C does not

produce radical state and *P* state production is totally suppressed. Only Cy5-Trolox shows higher occupancy of state *P* in compared to pure Cy5, such trend is also reflected in $R^{\bullet+}$ state (See Figure 3.9 a).

In Figure 3.10 we show the analysis for air saturated EtOH as we did for buffer.

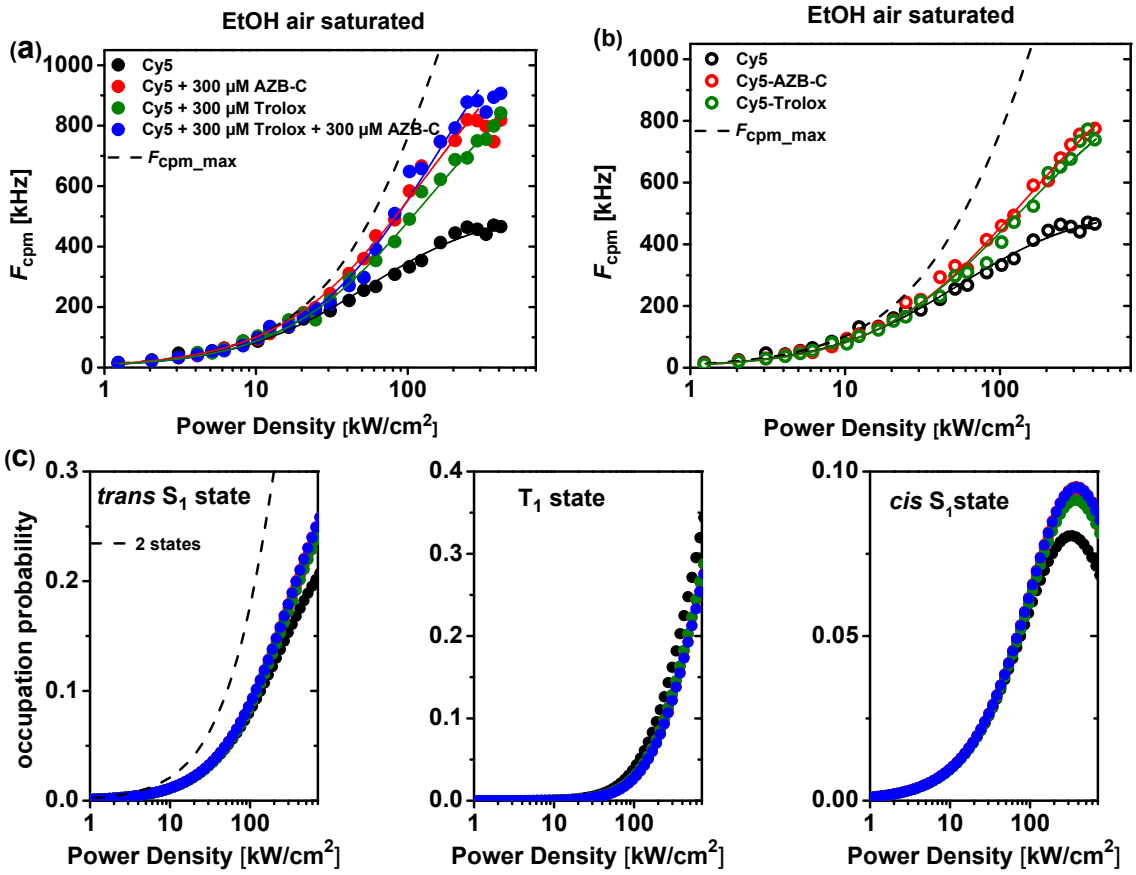

Figure 3.10. Fluorescence signal at different power densities in air saturated EtOH (points) calculated according to eq.(3.29) for additives (a) and for Cy5-conjugates (b). Fits (lines) according to eq.(3.9-3.19, 3.21, 3.27-3.28, 3.35, 3.39) using fixed parameters in: Table 3.4 (k_b), for fast processes Table S3 (k_0, σ, σ_{BISO}, k_{ISO}, k_{ISC}, k_T) and for quenchers Table 3.6 (k_{qS} and k_{qT}). For fluorescence quantum yield (Φ_F) see Table 3.2, G_{Detect} is a free parameter for all fits (average value = 0.025 ± 0.003). Black dashed line: maximal achievable fluorescence signal eq. (3.33-3.34). (c) Occupation probabilities for *trans* S_1 (black dashed line calculated with eq.(3.32)), T_1 and *cis* S_1 state.

In ethanol no production of radical state is visible. High amount of radical in buffer is due to the higher dielectric constant of water (80.0) in comparison to ethanol (24.5). Thus in buffer the radical state is more stabilized. In this case, the behavior of Cy5-conjugates is very similar to

additives due to the fact that in such conditions the apparent local concentration decreases dramatically (below 1 mM), getting close to the concentration of additives.

Quenchers effect in argon solution

In Figure 3.11 we illustrate the effect of the quenchers and conjugated compounds using power density vs. count rate plots and the occupancies of the states in buffer under argon.

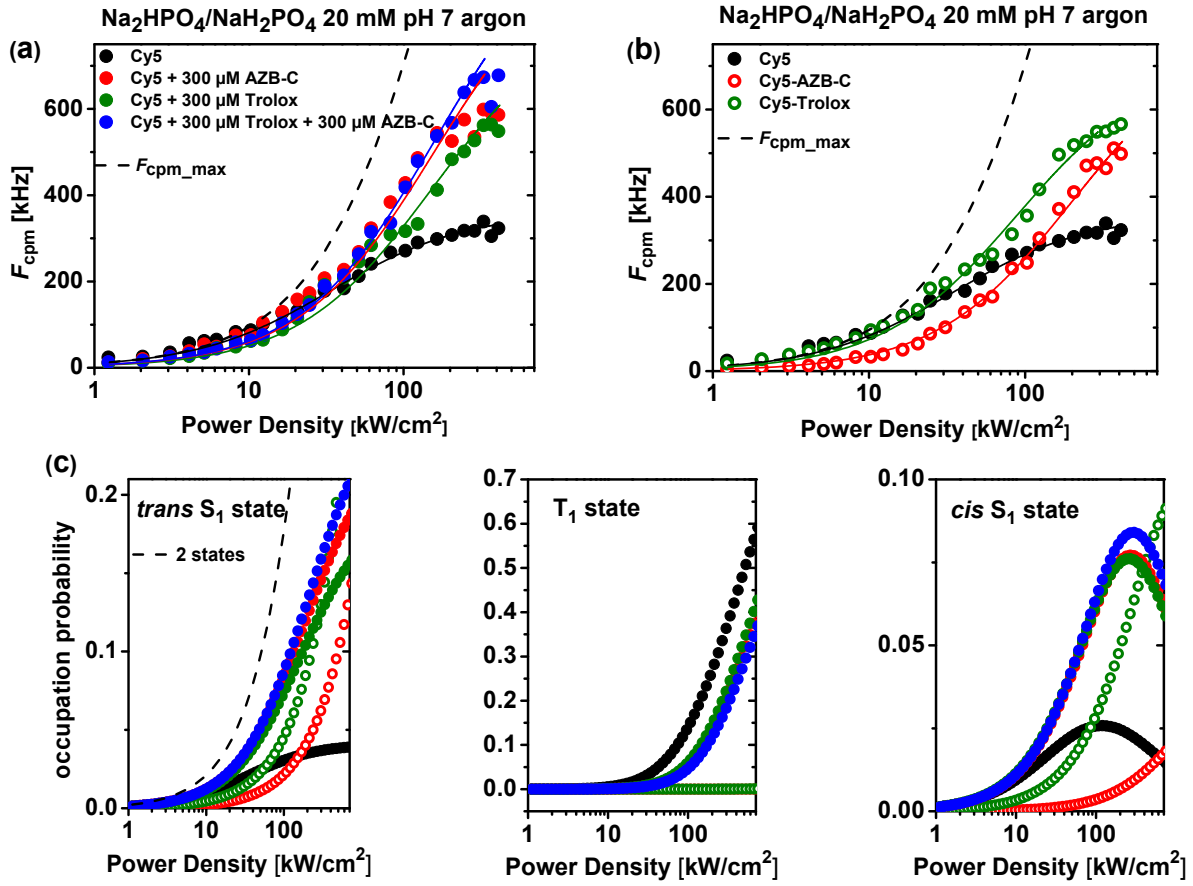

Figure 3.11. Fluorescence signal at different power densities in buffer under argon (points) calculated according to eq.(3.29) for additives (a) and for Cy5-conjugates (b). Fits (lines) according to eq.(3.9-3.19, 3.21, 3.27-3.28, 3.35, 3.39) using fixed parameters in: Table 3.4 (k_b), for fast processes Table S3 (k_0, σ, σ_{BISO}, k_{ISO}, k_{ISC}, k_T) and for quenchers Table 3.6 (k_{qS} and k_{qT}). For fluorescence quantum yield (Φ_F) see Table 3.2, G_{Detect} is a free parameter for all fits (average value = 0.025 ± 0.002). Black dashed line: maximal achievable fluorescence signal eq. (3.33-3.34). (c) Occupation probabilities for *trans* S_1 (black dashed line calculated with eq.(3.32)), T_1 and *cis* S_1 state.

In argon solution the triplet process for free Cy5 is 10 times slower (0.020-0.060 ms) hence the triplet amplitude is about 10 times higher in comparison with air saturated condition. At the same

time no radical state was observed without oxygen (See Figure 3.11). Consequently, the fluorescence intensity in measurements with and without oxygen for free Cy5 was similar (See Figures 3.8 and 3.11). Addition of additives or Cy5-conjugates decreases the occupancy of T_1 state. Conjugated compounds have a significant effect on the triplet term due to the high formal local concentration in buffer. The usage of Cy5-AZB-C resulted in the highest reduction of the triplet state (to 0) but unfortunately the F_{cpm} of such compound is lower than Cy5 due to the smaller fluorescence quantum yield.

In Figure 3.12 we examined the effect of the quenchers in ethanol under argon.

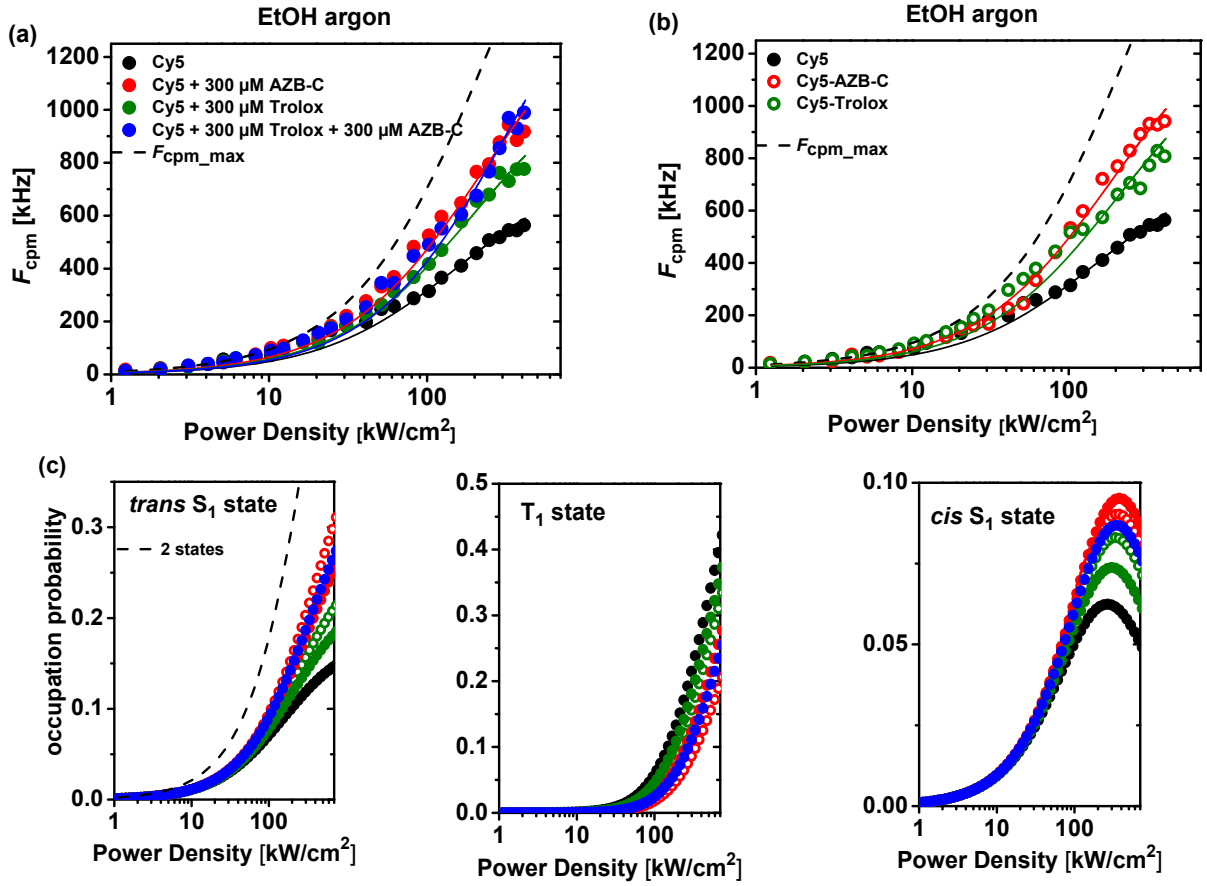

Figure 3.12. Fluorescence signal at different power densities in EtOH under argon (points) calculated according to eq.(3.29) for additives (a) and for Cy5-conjugates (b). Fits (lines) according to eq.(3.9-3.19, 3.21, 3.27-3.28, 3.35, 3.39) using fixed parameters in: Table 3.4 (k_b), for fast processes Table S3 (k_0, σ, σ_{BISO}, k_{ISO}, k_{ISC}, k_T) and for quenchers Table 3.6 (k_{qS} and k_{qT}). For fluorescence quantum yield (Φ_F) see Table 3.2, G_{Detect} is a free parameter for all fits (average value = 0.024 ± 0.002). Black dashed line: maximal achievable fluorescence signal eq. (3.33-3.34). (c) Occupation probabilities for *trans* S_1 (black dashed line calculated with eq.(3.32)), T_1 and *cis* S_1 state.

Also in this case radical state is not present and the triplet process is slower in comparison to the triplet formation in air saturated solution. The usage of additives or Cy5-conjugates decreases the probabilities of T_1 state. In this case the conjugates still show more effect than additives but less in comparison to buffer (Figure 3.12). Such findings reflect also the trends in terms of F_{cpm} signal.

3.4 Conclusions and outlook

Ideally, the maximum achievable fluorescence signal is given by a two state system where cycles between a first singlet excited state (S_1) and the ground state (S_0) with in a regular fluorescence photon emission, take place. In reality, also dark states are involved, like triplet state (T_1) and radical cation state ($R^{\bullet+}$) which reduce the fluorescence signal. To overcome this problem, we have used quenchers as additives or employed Cy5-conjugates produced by organic synthesis, in different environments and solvents. We demonstrated that AZB-C is a moderate triplet quencher and it also has influence on the radical term, Trolox reveals effect only on the triplet state. We observed photo-oxidation only in aqueous buffer with atmospheric oxygen where the formed radical cation state is stabilized by H_2O. In this case the quantum yield of bleaching increases dramatically and only Cy5-AZB-C has beneficial effect on the radical term. Indeed, the high formal local concentration of AZB-C in such compound allows to suppress totally the formation of $R^{\bullet+}$. In argon environment where no radical term is present, the triplet kinetics is at least 10 times slower than air saturated solution. Under such conditions, the usage of additives or Cy5-conjugates permits to reduce the triplet time and its amplitudes in FCS. The F_{cpm} trends are reflected in the occupancies of the fluorescent S_1 state; this is an evidence of the validity of our model, which allows us to predict and to improve the fluorescence signal.

Oxygen is responsible for photodestruction and photo-oxidation of the dye causing the production of radical cation ($R^{\bullet+}$). Oxygen can also be a good triplet state quencher causing the reduction of relaxation time of the triplet process. Indeed, removal of oxygen improves photostability of the dye, but does not influence the fluorescence signal significantly. Consequently, a good strategy for improving fluorescence signal together with photostability of the dye consists from the oxygen removal and addition of the triplet quencher like COT or AZB-C simultaneously.

Using eq. (3.44) we can calculate the average number of photons (N_F) emitted by a single dye before bleaching occurs. For Cy5 without quencher in air saturated buffer we obtain $N_F \approx 1 \cdot 10^5$ photons. The best improvement of photostability in air saturated buffer we achieved using Cy5-AZB-C conjugate, where $N_F \approx 5 \cdot 10^5$ photons. The highest photostability we observed in ethanol under argon if Cy5-AZB-C conjugate was used resulting in $N_F \approx 2 \cdot 10^8$ photons before bleaching, which is 2000 times more in comparison to dye in air saturated aqueous solution.

However, Cy5-conjugates did not improve the fluorescence signal with respect to the free dye in aqueous solution due to the lower fluorescence quantum yield in the conjugated compounds. In ethanol no strong singlet quenching was observed. The behavior of Cy5-conjugates in this case is very similar to additives due to the fact that in such conditions the apparent local concentration is close to the used concentration of additives (below 1 mM). In our experiments Cy5-conjugates in EtOH and additives had similar effect on the fluorescence signal.

Often in living-cell no free additives can be used which makes conjugates the only applicable option for improving fluorescence signal.

We achieved maximum countrate of 1 MHz with AZB-C in ethanol and buffer at excitation irradiance of $\langle I \rangle$ = 500 kW/cm^2. Considering, the theoretically possible local concentration of dark state quenchers in conjugated compounds of ≈100 mM (depending on linker length). We think that disadvantages of conjugates such as singlet quenching and inappropriate orientation for energy transfer between the quencher and the dye could be overcome using different linker lengths and stiffness. For AZB-C conjugate with such high local quencher concentration, no dark states will be present and the maximum possible count rate (2-level system) at our measurement condition would be 3 MHz.

Moreover, more detailed studies are needed to find the best linker length that permits the reduction of dark states amplitudes and in the same time no singlet quenching.

More experiments, in order to study the behavior of the dye quencher conjugated with also biomolecules could be done in the future.

3.5 Supporting Information

Material and methods

S1. *Chemical synthesis*

S1.1. *Chemical compounds used for synthesis*

Compound	Abbreviation	Structure	M_w
4- (phenylazo) benzoic acid	AZB-C	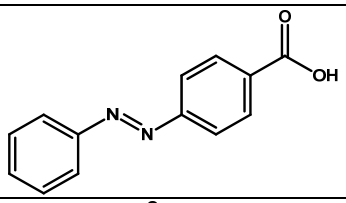	226.23
N-Hydroxysuccinimide	NHS	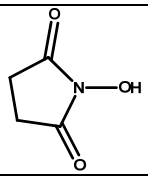	115.09
N-N´-Dicyclohexylcarbodiimide	DCC	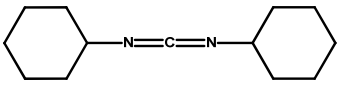	206.33
Dichloromethane	DCM	CH_2Cl_2	84.93
Ethylenediamine	EDA	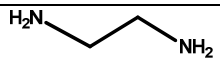	60.10
Tetrahydrofuran	THF	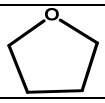	72.11
Sodium sulfate	/	Na_2SO_4	142.04
(±)-6-Hydroxy-2,5,7,8 tetramethylchroman-2-carboxylic acid	Trolox	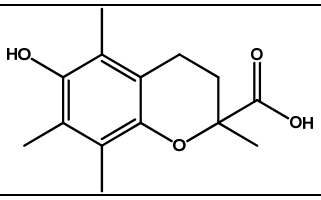	250.29
Hexane	/		86.18
Ethyl acetate	/	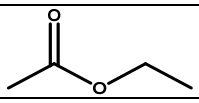	88.11
Sodium carbonate	/	Na_2CO_3	105.99
Dimethyl sulfoxide	DMSO	C_2H_6OS	78.13
Methanol	MeOH	CH_3OH	32.04

Malonaldehyde Dianilide	/	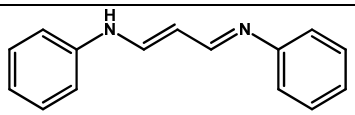	222.29
2,3,3-Trimethyl-5-sulfo-1-(4-carboxy-pentan)-3H-indolium	Indolium	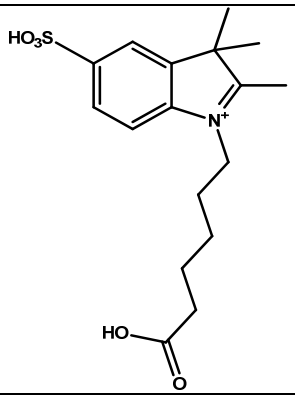	354.44
Acetic acid	/	CH_3COOH	60.05
Potassium acetate	/	CH_3COOK	98.15
Triethylamine	/	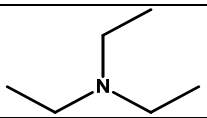	101.19

Table S1. Chemical compounds used for synthesis

S1.2. *General schematic representation of synthesis of Cy5-Quencher*

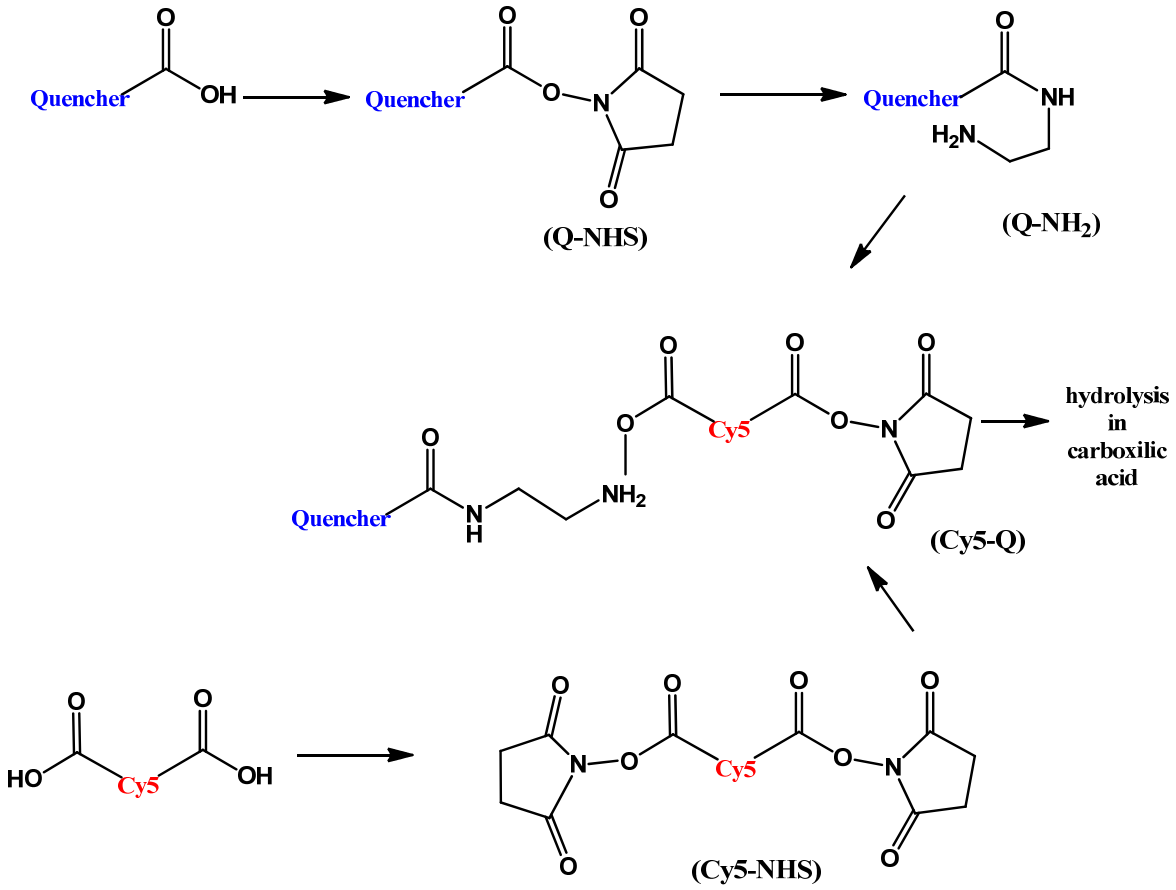

Figure S1. Chemical scheme used for synthetize Cy5-Q

The strategy provides the formation of activated ester of the quencher (Q-NHS) and of Cy5 (Cy5-NHS). Follows the conversion of Q-NHS in quencher amide ($Q-NH_2$) and then coupling of the $Q-NH_2$ with Cy5-NHS.

For the characterization of the compounds (also for intermediate steps) we used NMR and mass spectroscopy. All the ^{1}H-NMR spectra were recorded with 300 MHz. The chemical shifts were recalculated using the solvent as internal standard (δ= 7.26 $CDCl_3$). The mass spectra were recorded with electrospray ionization method or with electronic ionization technique depending on the specific case (See below).

S1.3. *Chemical synthesis of AZB-C activated ester (AZB-C-NHS)*

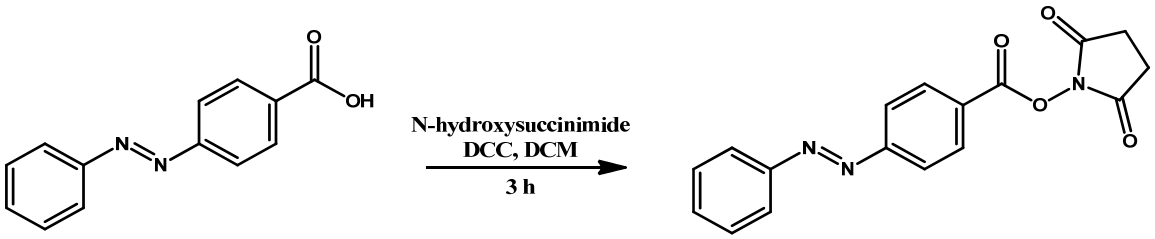

Figure S2. Chemical synthesis of AZB-C activated ester (AZB-C-NHS)

To a stirred solution of AZB-C (0.9045g, 4mmol) and N-Hydroxysuccinimide (0.5098, 4.4 mmol) in anhydrous DCM (20 mL), N-N´-dicyclohexylcarbodiimide (0.9033g, 4.4 mmol) was added under argon in dark room temperature. After 3 hours, the precipitated urea was removed by filtration and the solvent removed by evaporation. The resulting residual was purified by silica gel column chromatography eluting with a mixture of hexane and ethyl acetate in ratio 2:1 to provide AZB-C-NHS as an orange solid (1.130g, 80%). ^{1}H NMR (300 MHz, $CDCl_3$) δ = 2.83 (4H, s), 7.43-7.66 (3H, m), 7.87-8.09 (4H, m) 8.25-8.36 (2H, d).

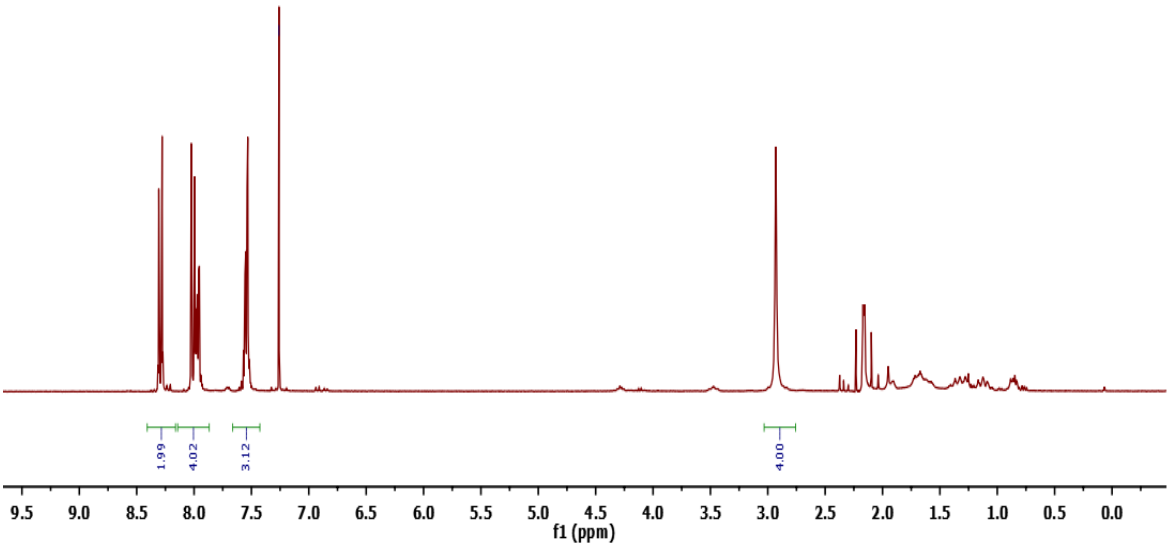

Figure S3. ^{1}H NMR spectrum of AZB-NHS. The blue numbers represent the integrated area for each specific multiplet.

S1.4 *Chemical synthesis of AZB-C amide (AZB-C-NH_2)*

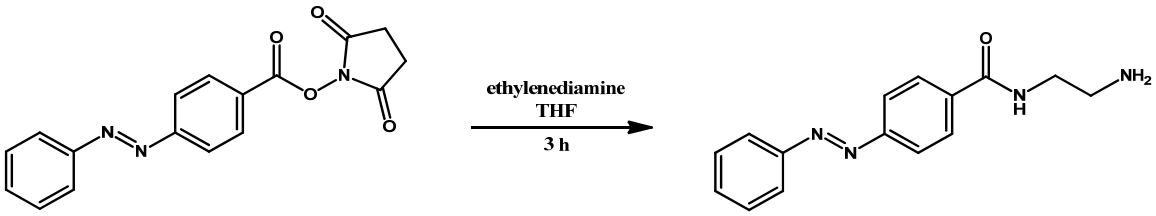

Figure S4. Chemical synthesis of AZB-C amide (AZB-C-NH_2)

2.3 ml (0.034 mol) of ethylenediamine were added in 44 mL THF and 1.130g (0.0034 mol) of AZB-NHS dissolved in 27 mL of THF was joined slowly at room temperature under nitrogen. After 3 hours of stirring at room temperature, 15 mL of DCM were added and the solution was washed three times with water. The organic compound was dried with sodium sulfate and purified by crystallization. After complete evaporation of the solvent, 0.4560g (0.0017 mol) of orange colored AZB-C-NH_2 were obtained. ^{1}H NMR (300 MHz, $CDCl_3$) δ = 2.95-2.86 (2H, t), 3.49-3.68 (2H, q), 7.40-7.60(3H, m) 7.83-8.09 (6H, m). EI-MS m/z calculated, for $C_{15}H_{16}N_4O$ = 268, found fragment m/z= 224 for $C_{13}H_{10}N_3O$.

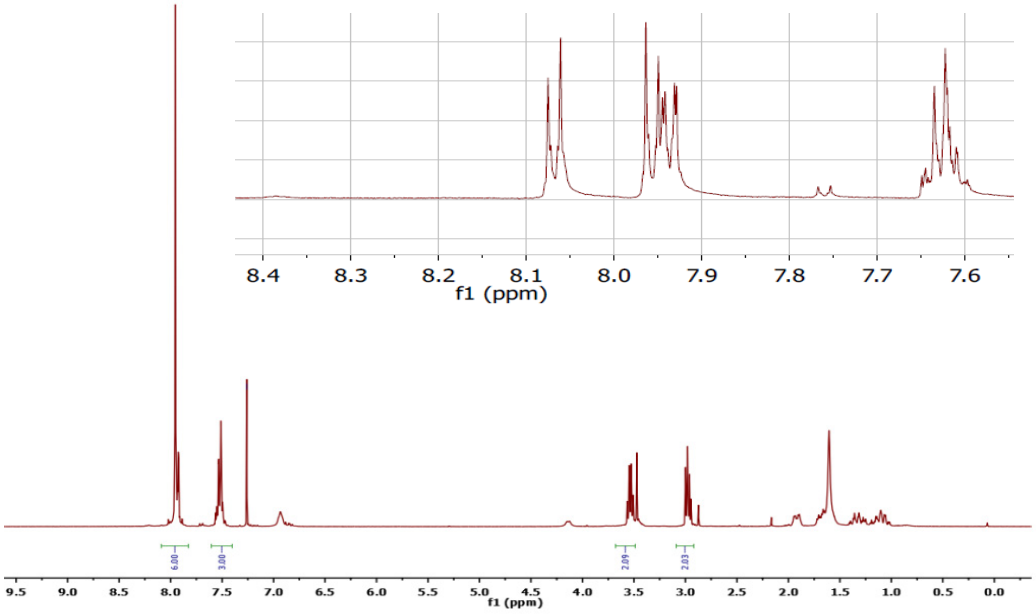

Figure S5. ^{1}H NMR spectrum of AZB-C-NH_2. The blue numbers represent the integrated area for each specific multiplet. On the top panel the magnification of the multiplets at high chemical shifts region.

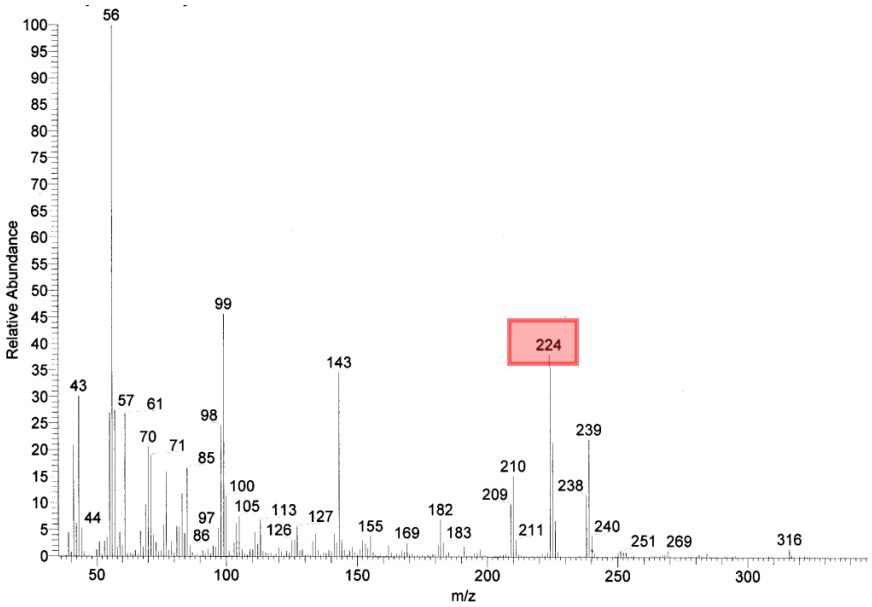

Figure S6. EI-MS spectrum of AZB-NH_2

S1.5 *Chemical synthesis of Trolox activated ester (Trolox-NHS)*

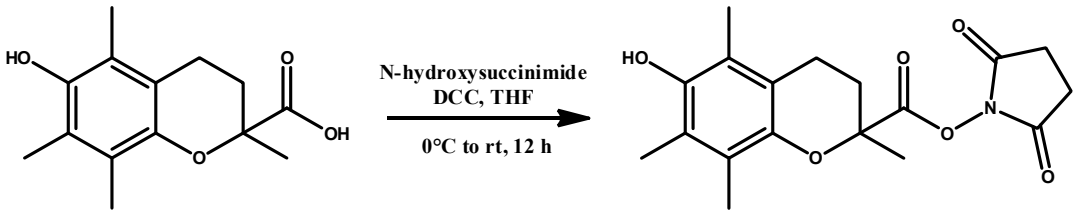

Figure S7. Chemical synthesis of Trolox activated ester (Trolox-NHS)

To a stirred 0°C solution of Trolox-COOH (0.2506g, 1 mmol) and NHS (0.1277g, 1.08 mmol) in anhydrous THF (21 mL) was added a solution of N-N´- Dicyclohexylcarbodiimide (0.2265g 1.08 mmol) in THF (13 mL) dropwise. The reaction mixture was slowly warmed to room temperature and stirred overnight under argon in dark. The precipitated urea was removed by filtration and the combined filtrate and wash was dried over Na_2SO_4 and concentrated. The resulting residual was purified by silica gel column chromatography eluting with a mixture of hexane and ethyl acetate in ratio 2:1 to provide Trolox-NHS as a white solid (0.3522g, 95%). EI-MS: m/z calculated for $C_{16}H_{21}NO_6$ =347, found m/z=347.

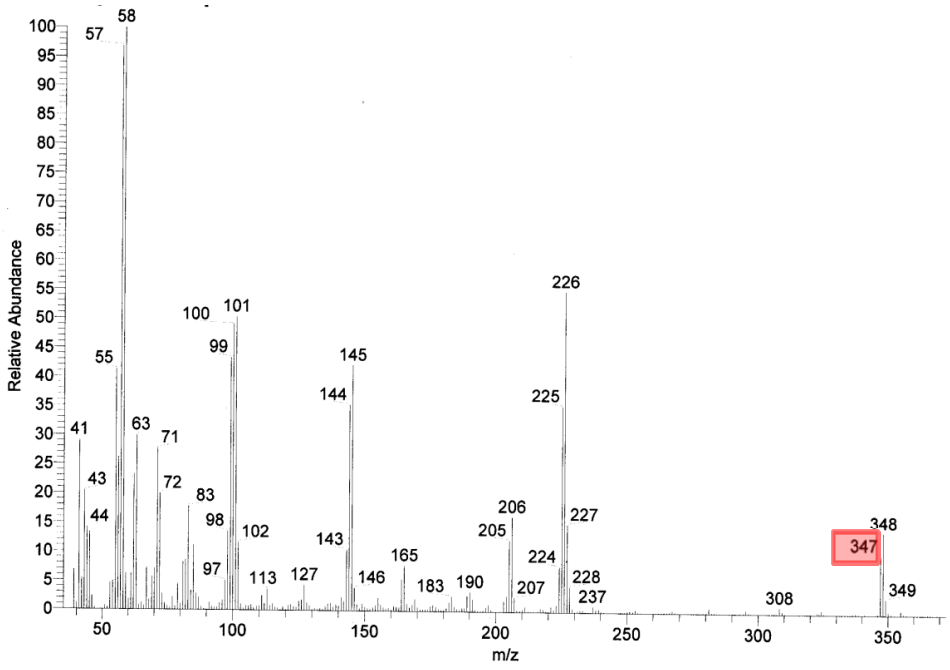

Figure S8. EI-MS spectrum of Trolox-NHS

S1.6 *Chemical synthesis of Trolox amide (Trolox-NH_2)*

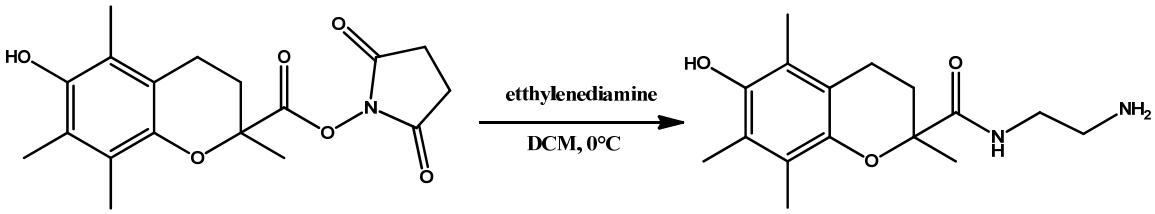

Figure S9. Chemical synthesis of Trolox amide (Trolox-NH_2)

To a stirred 0°C solution of ethylenediamine (0.5 mL) in DCM (30 mL) was slowly added solution of Trolox-NHS(0.2785g, 0.80 mmol) in DCM (15 mL). The solution was warmed to room temperature and stirred for 1 hour, then diluted with DCM (30 mL). The liquid was washed with saturated aq. Na_2CO_3 solution and brine, then dried over Na_2SO_4, filtered and finally concentrated to give a white solid (0.2130, 45%). ^{1}H NMR (300 MHz, $CDCl_3$) δ = 1.41 (3H, s), 1.70-1.81 (1H, m), 1.98(3H, s), 2.07 (6H, s), 2.19-2.29 (1H, m), 2.41-2.62 (4H, m), 3.00-3.14 (1H, m), 3.15-3.29 (1H, m). EI-MS: m/z calculated for $C_{16}H_{24}N_2O_3$ =292, found m/z = 292

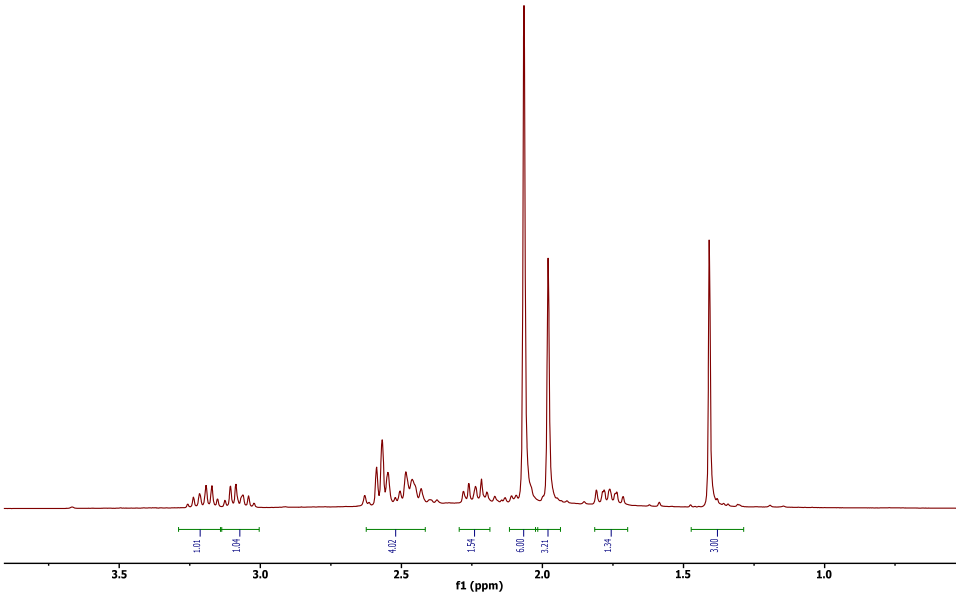

Figure S10. ^{1}H NMR spectrum of Trolox-NH_2. The blue numbers represent the integrated area for each specific multiplet.

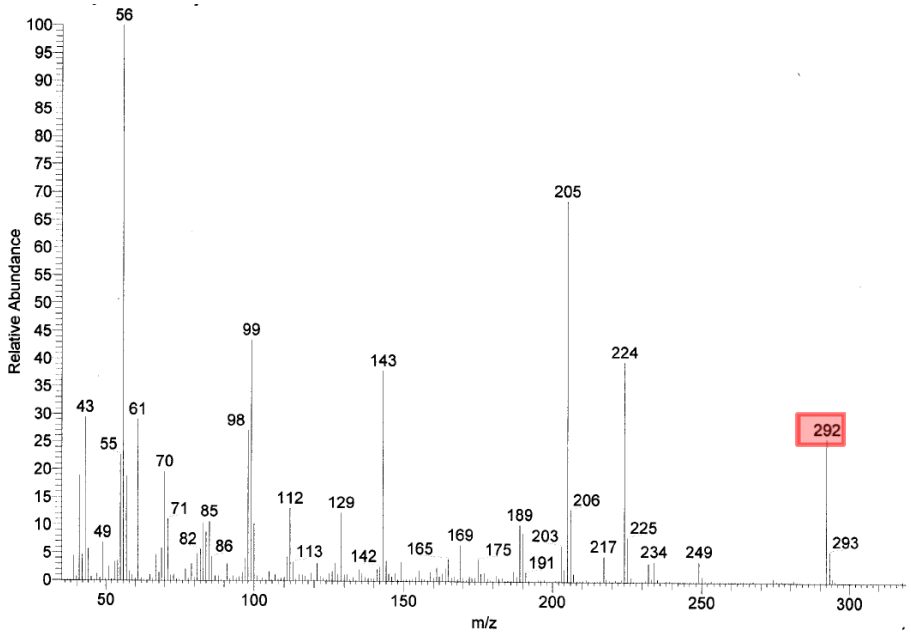

Figure S11. EI-MS spectrum of Trolox $-NH_2$

S1.7 *Chemical synthesis of Cy5*

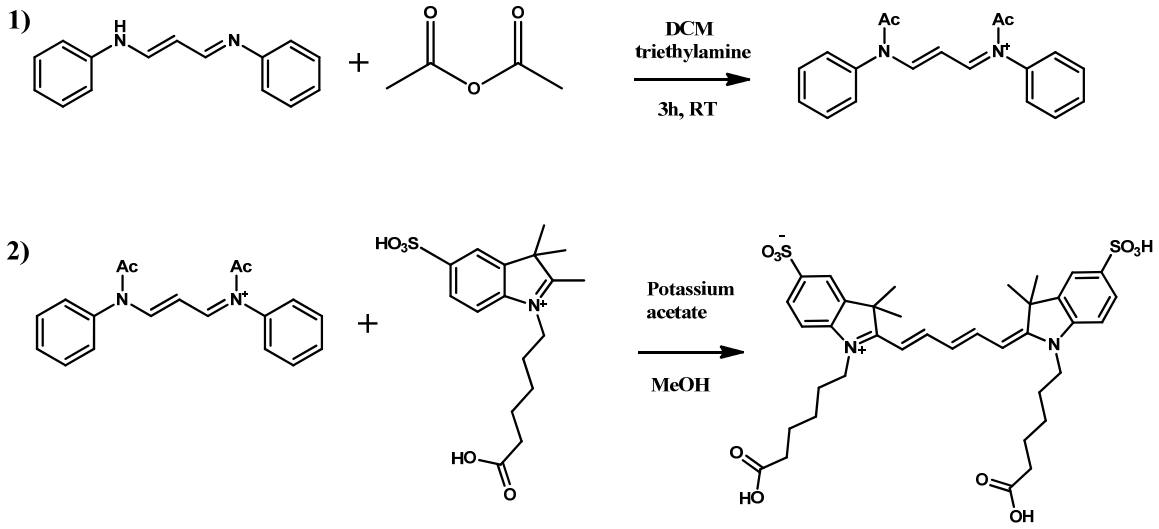

Figure S12. Chemical synthesis of Cy5

1) In the first step, malonaldehyde dianilide (0.35 mmol) is added to acetic acid (0.7 mmol) in 0.5 mL of DCM with 0.35 mmol triethylamine. The reaction was left at room temperature for 3 h in dark and controlled by TLC.
2) After 3 hours in the mixture 1) was added Indolium (0.7 mmol) and potassium acetate (0.35 mmol) in methanol (1.6 mL).

   The reaction was left at room temperature for 3 days. After that time, was added drop by drop diethyl ether and the blue solid (Cy5) was separated from the liquid by centrifugation.
3) The purification of the solid was done with silica gel column flash chromatography with mixture DCM/MeOH (2:1) and the solvent was evaporated to get the final product. ^{1}H NMR (300 MHz, $CDCl_3$) δ = 1.29-1.59 (12H, m), 1.68 (12H, s), 1.95-2.12(4H, m), 2.20-2.36 (4H, m), 6.22-6.38 (2H, m), 6.53-6.67 (1H, m), 7.27-7.36 (2H, m), 7.59-7.68 (2H, m), 7.80 (2H, s), 8.28-8.42 (2H, t). The others signals represent the residual solvents used for the synthesis (DCM, MeOH and diethyl ether).

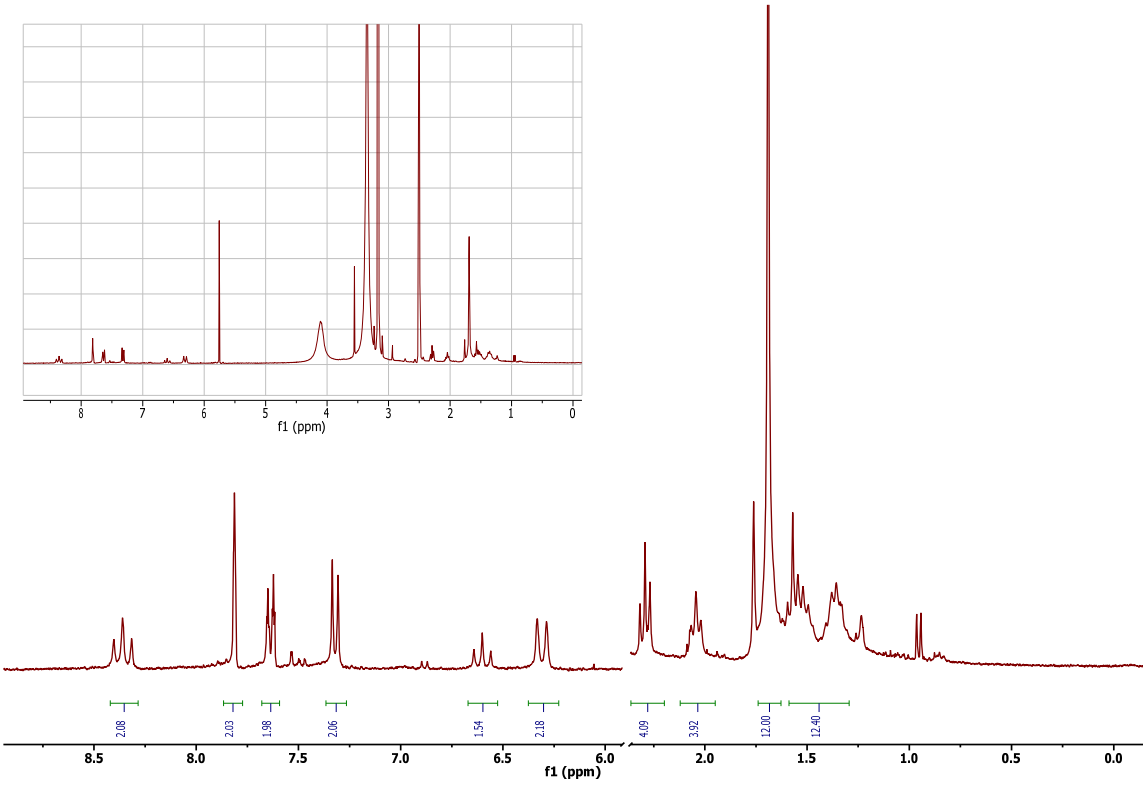

Figure S13. ^{1}H NMR spectrum of Cy5. On the top, the completed spectrum, below a section with the typical Cy5 signals. The blue numbers represent the integrated area for each specific multiplet.

S1.8 *Chemical synthesis of Cy5 activated ester (Cy5-NHS)*

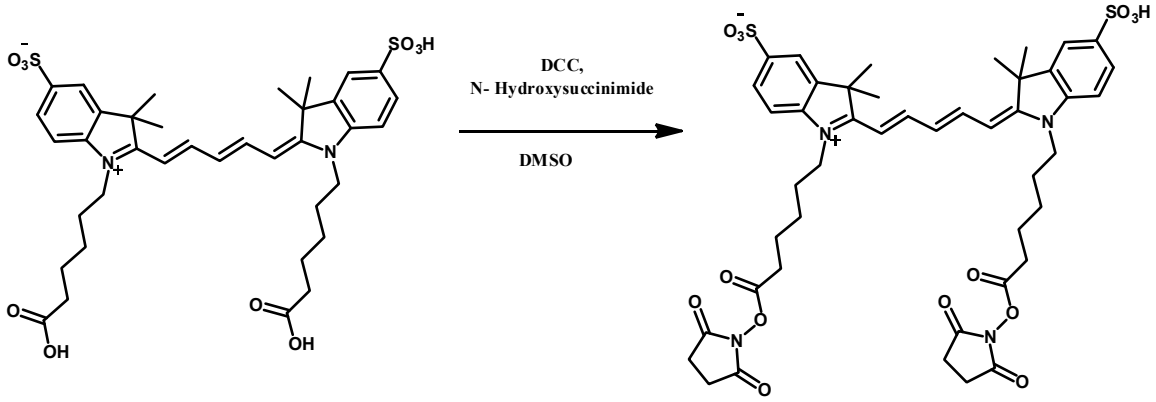

Figure S14. Chemical synthesis of Cy5 activated ester (Cy5-NHS)

The dye (0.064 mmol) was dissolved in 1.4 mL dry DMSO (1mL/ 50 mg of the dye). N,N´ dicyclohexyl carbodiimide (5 eq./carboxyl group) and N-hydroxysuccinimide (10 eq./carboxyl group) was added. The mixture was left at dark room temperature for 10 hours. The reaction was controlled by TLC and in the end the mixture was diluted with dry ethyl acetate. The precipitated urea was removed by centrifugation and the ethyl acetate was removed by evaporation. The Cy5-NHS was left in the DMSO solvent for the next step. ESI-MS calculated $C_{45}H_{50}N_4O_{14}S_2^{2-}$ $[M-2H]^{2-}$ =467.1 found $[M-2H]^{2-}$ =467.1

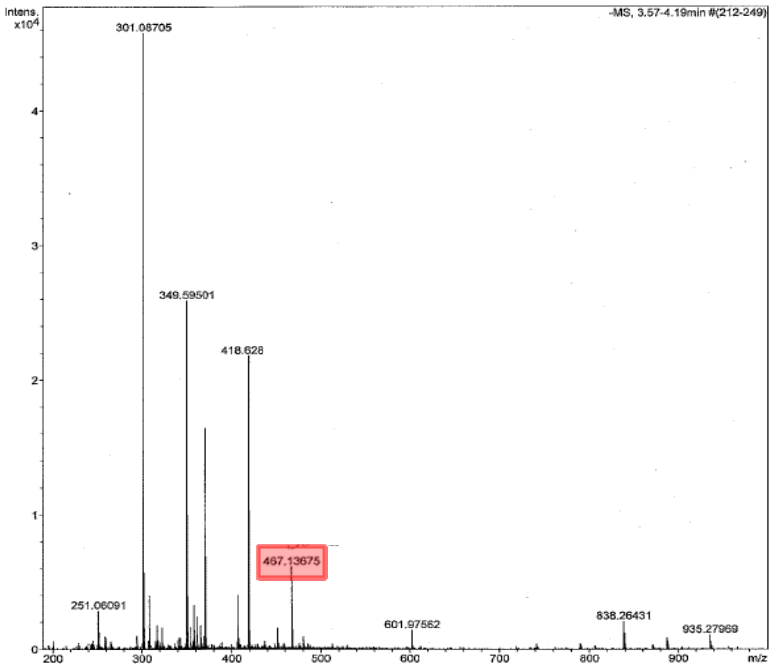

Figure S15. ESI-MS$^-$ spectrum of Cy5-Mono-NHS ester and Cy5-Bis-NHS ester.

S1.9 *Chemical synthesis of Cy5-AZB-C and Cy5-Trolox*

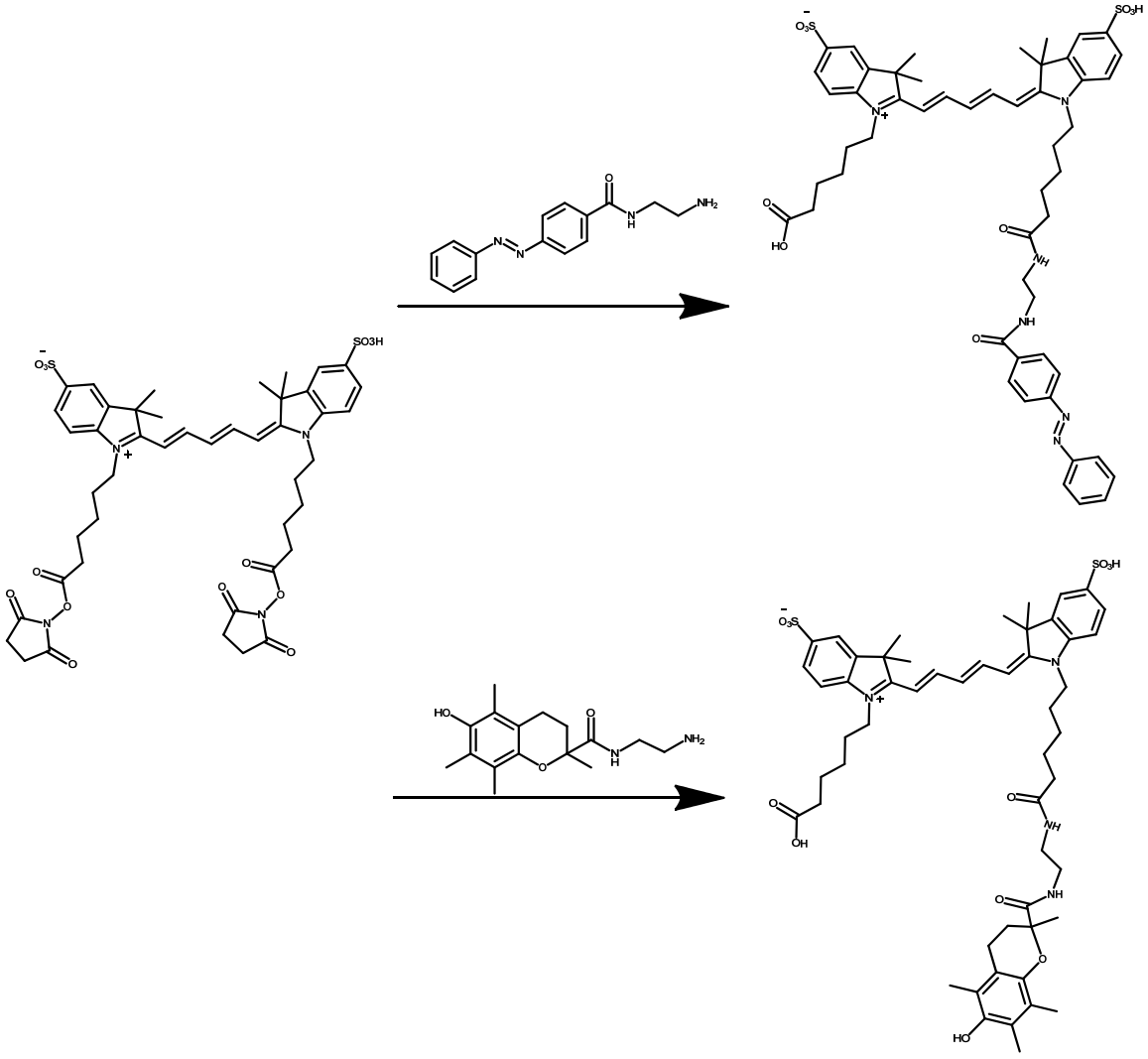

Figure S16. Chemical synthesis of Cy5-AZB-C and Cy5-Trolox

One equivalent of Q-NH_2 (32 mmol) in 0.350 mL DMSO was mixed in 2.6 mL of 50 mM potassium phosphate buffer pH=7.2 followed by addition of 0.7 mL of Cy5 bis-NHS ester (0.032 mol) in DMSO. The mixture was stirred in the dark room temperature. The reaction was monitored by TLC every 5 minutes until the end of reaction, about 30 min. The mixture was diluted with 6 mL of bidistillated water. Monoreacted Cy5-COOH was purified from unreacted and bis-reacted fluorophores using a semi-preparative HPLC C18 column with 0.1% of formic acid in water with a gradient elution of 25%-65% acetonitrile. ESI-MS calculated for Cy5-AZB-C $C_{52}H_{58}N_6O_{10}S_2^{2-}$ $[M-2H]^{2-}$ =495.2 found $[M-2H]^{2-}$ =495.2 and for Cy5-Trolox $C_{53}H_{67}N_4O_{12}S_2^{2-}$ $[M-H]^{1-}$ =1017.4 found $[M-H]^{1-}$ =1017.4.

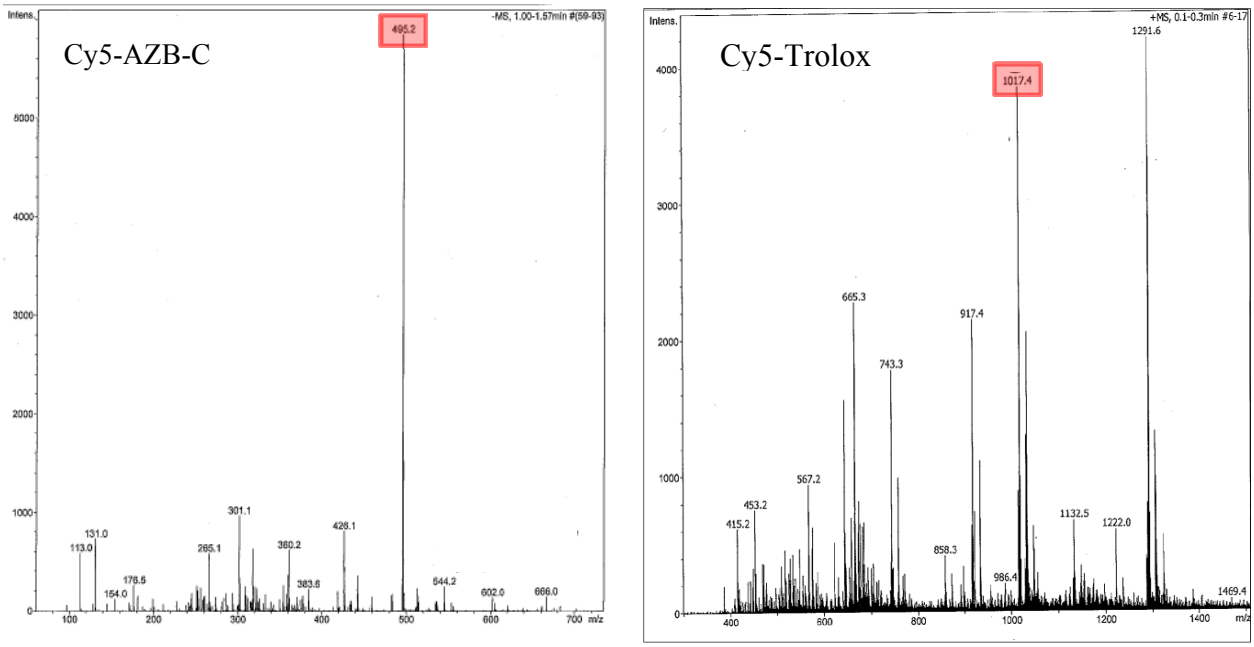

Figure S17. ESI-MS$^-$ spectra of Cy5-AZB-C and Cy5-Trolox

Analysis Methods

S2. *Estimation of mean intensity*

The mean excitation intensity can be estimated using the measured total power of the laser L and the area of the focused beam[181]. The measurements in buffer were performed in a set-up with confocal volume smaller in compare to the instrument used for measurements in ethanol. In both cases the calibration procedure were performed using Atto 647. Assuming a Gaussian beam profile, the focal radius $\omega_{0\_ex} = 0.75$ µm and 0.88 µm for the two set-up is determined. Respectively, the diffusion time $t_d = 0.35$ ms and 0.48 ms (with $D = 3.97\ 10^{-10}$ m^2/s[93]) was measured for Atto 647 using a sufficiently large pinhole. The mean and maximum excitation intensities are defined according to eq. (S1) and eq. (S2) respectively

$$< I >_{ex} = \frac{L}{\pi \omega_{0\_ex}^2} \tag{S1}$$

$$I_0 = \frac{2L}{\pi \omega_{0\_ex}^2} = 2 < I >_{ex} \tag{S2}$$

Usage of a small pinhole requires a correction of the average mean intensity. Diffusion time t_d = 0.23 ms and 0.29 ms for Atto 647 is measured for the two set up with pinhole size of d=70µm. The assumption of a Gaussian detection profile permits to estimate the radius of the detection volume (eq. (S3)) ω_0 = 0.60 µm and 0.69 µm.

$$D = \frac{\omega_0^2}{4 t_d} \tag{S3}$$

Numerical integration of the excitation profile (eq. (S4)) within the limits of $-\omega_0$ to $+\omega_0$ yields the average excitation intensity $\langle I \rangle$ (eq. (S5))

$$I(\mathrm{r}) = I_0 \cdot \exp\left(-2 \cdot \frac{r^2}{\omega_0^2} \right) \tag{S4}$$

with $r = \sqrt{x^2 + y^2}$, giving the following power density for two set up:

$$< I >_{F_{FCS}} \approx 0.73 I_0 = \frac{1.5L}{\pi \omega_{0\_ex}^2} \tag{S5}$$

$$< I >_{F_{FCS}} \approx 0.76 I_0 = \frac{1.5L}{\pi \omega_{0\_ex}^2}$$

$$< I >_{F_{cpm}} \approx 0.48 I_0 = \frac{0.96L}{\pi \omega_{0\_ex}^2}$$

$$< I >_{F_{cpm}} \approx 0.51 I_0 = \frac{1.02L}{\pi \omega_{0\_ex}^2}$$

S3 Excitation profile and molecular detection efficiency

In the present work we computed the laser beam profile (Lorentzian along the z-axis and Gaussian in the radial direction), and corresponding collection efficiency function (CEF) of pinhole with molecule detection efficiency (MDE) numerically (eq. (S6-S8)):[181]

$$I(r_{xy}',z)=\frac{1}{\omega^2(z)}\cdot e^{-2\frac{r_{xy}'}{\omega^2(z)}} \tag{S6}$$

$$CEF(r_{xy}',z)=\int T(r_{xy})\cdot PSF(r_{xy},r_{xy}',z)\cdot dr \tag{S7}$$

$$MDE(r_{xy}',z)=CEF(r_{xy}',z)\cdot I(r_{xy}',z) \tag{S8}$$

with

$$\omega^2(z)=\omega_0{}^2+z^2\cdot\tan^2\delta \tag{S9}$$

$$PSF(r_{xy},r_{xy}',z)=\frac{circ\dfrac{(r_{xy}-r_{xy}')}{R(z)}}{\pi\cdot R^2(z)} \tag{S10}$$

$$T(r)=circ\left(\frac{r_{xy}}{s_0}\right),\qquad circ\left(\frac{r_{xy}}{s_0}\right)=\begin{cases}1 & \text{if } |r_{xy}|\le s_0\\ 0 & \text{if } |r_{xy}|>s_0\end{cases}, \tag{S11}$$

$$R^2(z)=R_0{}^2+z^2\cdot\tan^2\alpha \tag{S12}$$

where ω(z) is the radius of focused Laser eq. (S9), PSF is the point spread function eq. (S10), T(r) is the transmission function of the pinhole approximated by disk function eq. (S11), R(z) is the radius of the image spot of a point source located at distance z from the sample plane xy eq. (S12), ω_0 (ω_0=0.75 μm) is the beam waist radius at 1/e² intensity, δ (δ=0.28 rad) is the focusing angle of laser beam in the sample at 1/e² intensity, z is the distance from the sample plane along the optical axis, r_{xy}' is the radial coordinate of the point source in the sample space. s_0 (s_0=0.5 μm) m is the radius of the pinhole projected to the sample space, r_{xy} is the projection of the image plane radial coordinate, α (α=1.12 rad) is the aperture half-angle of the microscope objective and R_0 (R_0=0.2μm) is the resolution limit of the objective.

The average power density in observation volume was calculated by eq. (S13)

$$I_{av\_obs}=\frac{\sum\left(MDE(r_{xy}',z)\cdot I(r_{xy}',z)\right)}{\sum MDE(r_{xy}',z)} \tag{S13}$$

By calculation of average power density in observation volume by FCS measurements the squared dependence of correlation function from emitter brightness need to be considered. The average power density in this case was computed by eq. (S14)

$$I_{av\_obs\_FCS} = \frac{\sum\left(MDE^2(r_{xy}', z) \cdot I^2(r_{xy}', z)\right)}{\sum MDE^2(r_{xy}', z)} \tag{S14}$$

Note in both eq. (S13) and eq. (S14) the signal saturation effects at higher power density's are neglected.

S4 Numerical simulation of species probabilities in excitation profile

We used three state model represented by Figure S18 to describe the photobleaching and radical cation kinetics of Cy5.

$$F \xrightarrow{koxtot} R^+$$
$$F \xrightarrow{kbFtot} P$$
$$R^+ \xrightarrow{red} F$$
$$R^+ \xrightarrow{kbR} P$$
$$F + R^+ + P = 1$$

Figure S18. Photobleaching and radical cation kinetics scheme of Cy5.

The corresponding transition rate matrix (TRM) for such kinetic model is given by eq. (S15)

$$\begin{pmatrix} F'(t) \\ R^{+\prime}(t) \\ P'(t) \end{pmatrix} = \begin{pmatrix} -k_{oxtot} - kbFtot & k_{red} & 0 \\ k_{oxtot} & -k_{red} - kbR & 0 \\ kbFtot & kbR & 0 \end{pmatrix} \begin{pmatrix} F \\ R^+ \\ P \end{pmatrix} \quad \text{(S15)}$$

Considering influence of translational diffusion we obtain the transition rate matrix which is given by eq. (S16)

$$\begin{pmatrix} F'(t) \\ R^{+\prime}(t) \\ P'(t) \end{pmatrix} = \begin{pmatrix} -k_{oxtot} - kbFtot + D_F\nabla^2\partial F(t,r) & k_{red} & 0 \\ k_{oxtot} & -k_{red} - kbR + D_{R^+}\nabla^2\partial R^+(t,r) & 0 \\ kbFtot & kbR & D_P\nabla^2\partial P(t,r) \end{pmatrix} \begin{pmatrix} F \\ R^+ \\ P \end{pmatrix} \quad \text{(S16)}$$

where D_X is the diffusion coefficient of species X (for diffusion coefficient we assumed D_F=D_{R+}=D_P=D=0.39 μm²ms^{-1}), ∇^2 is Laplace operator, r is the spatial coordinate with $r = \sqrt{x^2 + y^2 + z^2}$

On one hand no reversible formed species (species *P* in Figure S18) are present and on the other hand diffusion processes are involved. Therefore, no simple analytical description for species probabilities in Gaussian-Lorentzian excitation profile is possible. We used finite difference method for numerical calculations of species probabilities in the excitation profile. In our

simulations eq.(S19) was used for numerical calculations of species probabilities where both diffusion and chemical kinetics are included.

The chosen parameter for our simulation where:

spatial resolution $\Delta x = \Delta y = \Delta z$ =0.05 µm

time resolution Δt = 0.25µs

initial Parameter $F(t_0)$= 1, $R(t_0)$= 0, $P(t_0)$= 0

diffusion coefficient D=0.39 $\mu m^2 ms^{-1}$

laser beam profile (Lorentzian along the z-axis and Gaussian in the radial direction, see S3)

k_{red}= 250 s^{-1}

k_{ox}= 2500 s^{-1}

k_{bF}=600 s^{-1}

k_{bR}=240 s^{-1}

Since our simulation represents an already established standard technique, below we give only a short brief description for our simulation procedure.

By discretizing time coordinate ($t \to t_n;\quad t_n = t_0 + n \cdot \Delta t$) the numerical simulation for species probabilities X without diffusion (only chemical kinetics) can be performed using forward difference method (eq.(S17)),where by known $X(t) \equiv X^n$ values, the values at next time step X^{n+1} are computed directly.

$$X_{kin}'(t) \equiv X_{kin}^n ' \approx \frac{X^{n+1} - X^n}{n} \Rightarrow X^{n+1} = X^n + X_{kin}^n ' \cdot n \tag{S17}$$

In our case for each time step the derivatives $X_{kin}'(t)$ is computed using TRM (eq. (S13)) with known initial parameter $F(t_0)$= 1, $R(t_0)$= 0, $P(t_0)$= 0.

For modeling influence of diffusion processes at species probabilities also the spatial coordinate r need also to be discretized:

$$x \to x_i, y \to y_j\ z \to z_k;$$
$$x_i = x_0 + i \cdot \Delta x,\ \ y_j = y_0 + j \cdot \Delta y,\ \ z_k = z_0 + k \cdot \Delta z;$$
$$X^n \equiv X^n_{i,j,k} \equiv X(x_i, y_j, z_k; t_n);$$

Using the discretization of time and spatial coordinates the numerical integration for second derivative was done according to forward Euler method (eq. (S18)):

$$X^{n+1} = X^n + X^n \cdot [\nu_x \cdot \delta_x^2 + \nu_y \cdot \delta_y^2 + \nu_z \cdot \delta_z^2] \tag{S18}$$

with

$$\nu_x = D\frac{\Delta t}{\Delta x^2}, \quad \nu_y = D\frac{\Delta t}{\Delta y^2}, \quad \nu_z = D\frac{\Delta t}{\Delta z^2}$$
$$X^n \cdot \delta_x^2 = X^n_{i-1,j,k} - 2 \cdot X^n_{i,j,k} + X^n_{i+1,j,k}$$
$$X^n \cdot \delta_y^2 = X^n_{i,j-1,k} - 2 \cdot X^n_{i,j,k} + X^n_{i,j+1,k}$$
$$X^n \cdot \delta_z^2 = X^n_{i,j,k-1} - 2 \cdot X^n_{i,j,k} + X^n_{i,j,k+1}$$

The combination of equations (S17) and (S18) leads to eq.(S19) which allows the numerical calculation for species probabilities where both diffusion and chemical kinetics are included.

$$X^{n+1} = X^n + X^n \cdot [\nu_x \cdot \delta_x^2 + \nu_y \cdot \delta_y^2 + \nu_z \cdot \delta_z^2] + X^n_{kin} \cdot n \tag{S19}$$

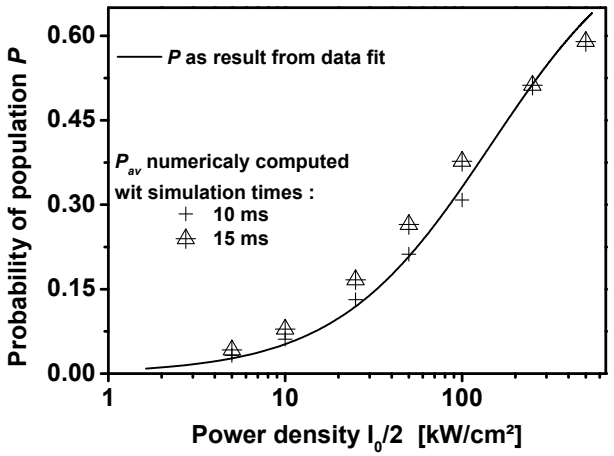

Figure S19 The probabilities of state *P* state numerically calculated P_{av} (symbols) and *P* as result from data fit (solid line) for Cy5 without additives in air saturated buffer (see main text). P_{av} is calculated from simulated spatial distribution *P(r)* using equation (S20).

$$P_{av} = P(r)\frac{\sum\left(MDE(r_{xy}',z)\cdot P(r)\right)}{\sum MDE(r_{xy}',z)} \tag{S20}$$

Note: By analysis of fluorescence data at confocal setup we need to estimate the equilibrium level of fluorescence signal (equilibrium between F and R^+, SI 6), where with increasing power density the time for achieving the equilibrium increases with increasing power density. This corresponds to "waiting time", where the excitation power is already applied but the fluorescence signal is not included in the apparent fluorescence signal, which is used for our data analysis. The formation of irreversible state P while this "waiting time" need to be considered by data analysis. This is the reason, why we use different simulation times for numerical calculations (t_{sim}=5-15 ms) (Figure S19).

S5 Calculation of effective detection profile for diffusing radicals

In our experiments, the characteristic diffusion time (t_d) at laser profile is $t_d \approx 0.3$ ms (ω_0 = =0.75 µm, D=0.39 µm²ms^{-1}). Because the singlet, triplet and *trans-cis* populations occur in a much faster time range they can be dealt separately from diffusion. This is not the case for radical cation populations, where kinetics in millisecond range are expected, thus effect of diffusion at amplitudes of radical cation stat R^+ need to be considered.

Assuming for radical cation lifetime ($t_{R+}=1/k_{red}$) to be independent from power density, we can describe the probability to find the molecule in state R^+ at time t after formation by eq. (S21). The probability for any diffusing particle *p* in three dimensional space with diffusion coefficient *D* to be after time *t* at distance *r* can be described by eq. (S22).

$$R^+(t) = e^{(-kred \cdot t)} \tag{S21}$$

$$p(r,t) = \frac{e^{\left(-\frac{r^2}{4 \cdot D \cdot t}\right)}}{(4 \cdot \pi \cdot D \cdot t)^{3/2}} \tag{S22}$$

The combination of eq. (S21) with eq. (S22) leads to eq. (S23) which describes the probability to find the diffusing molecule in state R^+ at time t radical cation formation and at distance *r* from position of formation radical cation formation.

$$R^+(r,t) = \frac{e^{\left(-\frac{r^2}{4 \cdot D \cdot t}\right)}}{(4 \cdot \pi \cdot D \cdot t)^{3/2}} \cdot e^{(-kred \cdot t)} = \frac{e^{\left(-\frac{r^2}{4 \cdot D} - kred \cdot t^2\right)}}{(4 \cdot \pi \cdot D \cdot t)^{3/2}} \tag{S23}$$

Assuming conditions where the radical cations continuously formed at one single point and diffuse away. At such conditions after time $t>>1/k_{red}$ the equilibrium between diffusion decaying and formation will be achieved. The spatial probability distribution for radical cation state at equilibrium conditions can be described by eq. (S24)

$$R^+_{SPD}(r) = \int_{t=0}^{\infty} \int_{r=0}^{\infty} \frac{e^{\left(-\frac{r^2}{4 \cdot D} - kred \cdot t^2\right)}}{(4 \cdot \pi \cdot D \cdot t)^{3/2}} \cdot dt \cdot dr \tag{S24}$$

In real experiments the radical cations are formed in excitation profile. If saturation effects and diffusion are negligible, the spatial distribution of probability's for radical cation will follow

exact the excitation profile. Under conditions where the diffusion need to be considered the spatial distribution of probability's for radical cation can be calculated by convolution eq. (S25) of eq. (S24) with excitation profile (eq. (S6) in our experiments).

$$R^{+}_{\mathrm{Prof}}(r) = I(r_{xy}', z) * R^{+}_{SPD}(r) \tag{S25}$$

To calculate $R^{+}_{SPD}(r)$ in our experiments we approximated eq. (S24) numerically by eq.(S26) with spatial discretization *i* and time discretization *n* within the limits $t_0 \rightarrow t$ and $r_0 \rightarrow r$(where $t >> 1/k_{red}$, $r >> FWHM_{ex}$; full width at half maximum of excitation profile), then computed the excitation profile $I_{num}(r)$ by eq. (S6) using the same numerical parameter.

$$R^{+}_{SPD\_num}(r) \approx \sum_{t=0}^{t} \sum_{r=0}^{r} \frac{e^{\left(-\frac{r}{4\cdot D} - kred\cdot t^2\right)}}{\left(4\cdot\pi\cdot D\cdot t\right)^{3/2}} \cdot \Delta t \cdot \Delta r \tag{S26}$$

$$r = \sqrt{x^2 + y^2 + z^2}; x \rightarrow x_i, y \rightarrow y_j \; z \rightarrow z_k; \Delta x = \Delta y = \Delta z = 0.1\mu m; \; x_0 = y_0 = z_0 = 0;$$

$$x_i = 0 + i\cdot\Delta x, y_j = x_0 + j\cdot\Delta x, y_j = y_0 + j\cdot\Delta y, \; z_k = z_0 + k\cdot\Delta z;$$

$$x_{\max}, y_{\max} = 8\mu m, z_{\max} = 48\mu m;$$

$$t \rightarrow t_n; \quad t_n = t_0 + n\cdot\Delta t; \; t_{\max} = 20ms$$

Afterwards we computed convolution (eq. (S27)) between numerically calculated excitation profile $I_{num}(r)$ and eq. (S26):

$$R^{+}_{\mathrm{Prof\_num}}(r) = I_{num}(r) * R^{+}_{SPD\_num}(r) \tag{S27}$$

For our data analysis we calculated the relative average probability distribution for radical cation state in the observation volume $\eta_{D(t_R)}$ according to eq. (S29). For FCS data, where the squared dependence of correlation function from emitter brightness need to be considered the average probability distribution $\eta_{D(t_R)FCS}$ is calculated according to eq. (S30).

Note: we normalized $R^{+}_{\mathrm{Prof\_num}}(r)$ before calculating $\eta_{D(t_R)}$ or $\eta_{D(t_R)FCS}$ using the maxima of area normalized probability distribution $R^{+}_{\mathrm{Prof\_num}}(r)$ (eq. (S28)).

$$R^{+}_{\text{Prof(norm)}}(r) = \frac{R^{+}_{\text{Prof\_num}}(r)}{\text{maximum}\left(\frac{R^{+}_{\text{Prof\_num}}(r)}{\sum R^{+}_{\text{Prof\_num}}(r)}\right)} \tag{S28}$$

$$\eta_{D(t_R)} = \left(R^{+}_{\text{Prof\_num}}(r) \frac{\sum \left(MDE(r_{xy}', z) \cdot R^{+}_{\text{Prof(norm)}}(r) \right)}{\sum MDE(r_{xy}', z)} \right)^{-1} \tag{S29}$$

$$\eta_{D(t_R)FCS} = \left(R^{+}_{\text{Prof\_num}}(r) \frac{\sum \left(MDE^2(r_{xy}', z) \cdot \left(R^{+}_{\text{Prof\_N}}(r) \right)^2 \right)}{\sum MDE^2(r_{xy}', z)} \right)^{-1} \tag{S30}$$

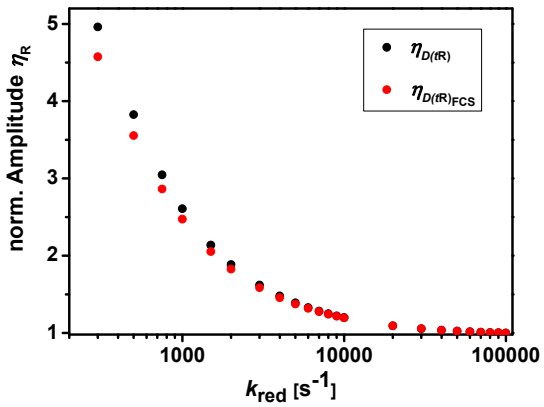

Figure S20. Relative average probability distribution for radical cation state in observation volume $\eta_{D(t_R)}$ (black dots) and $\eta_{D(t_R)FCS}$ (red dots) computed according to eq.(S29) and eq. (S30) respectively (see text above).

In our fitting models we used the average of probability distribution $\eta_{D(t_R)}$ and $\eta_{D(t_R)FCS}$ to calculate radical cation amplitude R_{eq} according to eq. (S31), where influence diffusion of molecules at detection profile need to be considered.

$$R_{eq(diff)} = \frac{k'_{oxtot}}{k'_{oxtot} + k'_{red}\eta_{D(t_R)}} \tag{S31}$$

S6. F_{cpm} fits without and with η_{bleach} for Cy5 air saturated buffer.

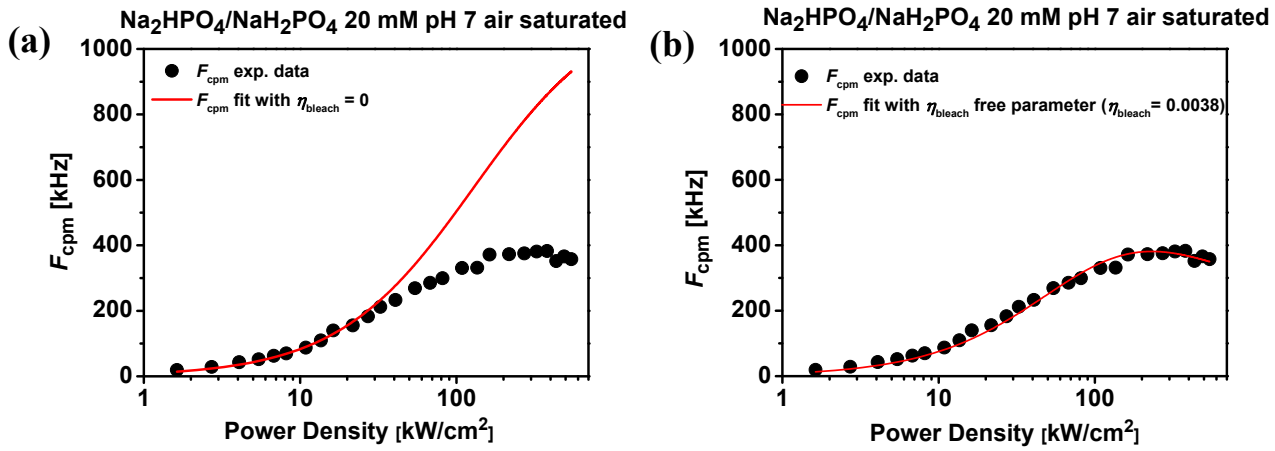

Figure S21. F_{cpm} (points, eq.(3.36)) for Cy5 in air saturated buffer with fits (red line) (a) Fit using eq.(3.9-3.26, 3.35, 3.39-3.40) with η_{bleach} value fixed to 0, (b) Fit using eq.(3.9-3.26, 3.35, 3.39-3.40) with η_{bleach} free parameter.

Clearly the usage of η_{bleach} factor is necessary in saturation curves to include bleaching effect in the fit.

Results and discussion

S7. *Lifetime fits*

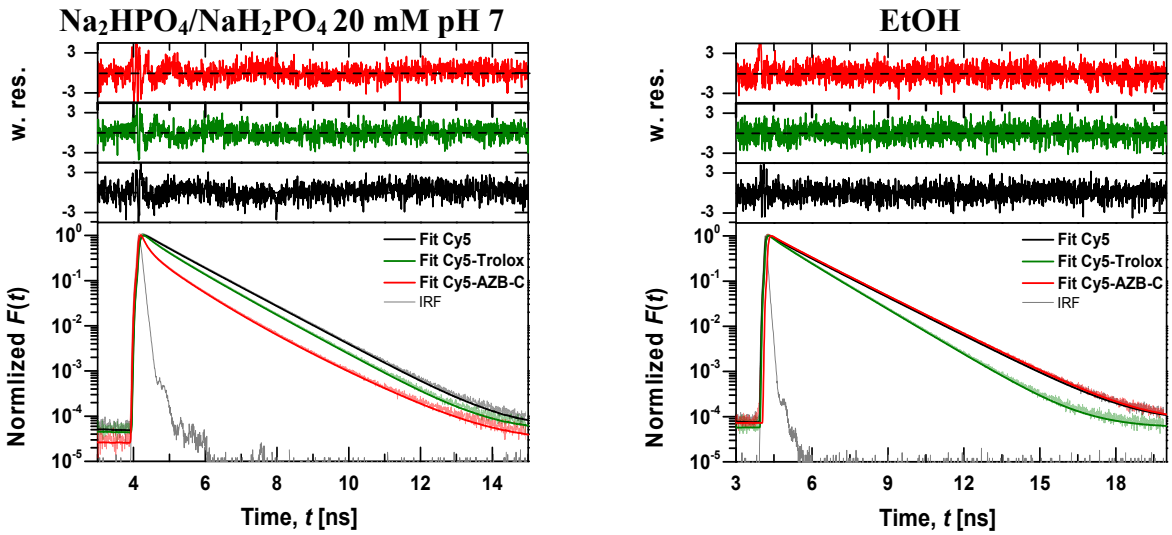

Figure S22. Lifetime fits in buffer and in EtOH for Cy5 and Cy5-conjugates with maximum counts of 50000 for each curve.

	Na_2HPO_4/NaH_2PO_4 20 mM pH 7						EtOH				
	τ_1 [ns] (x_1)	τ_2 [ns] (x_2)	τ_3 [ns] (x_3)	τ_4 [ns] (x_4)	$\langle\tau\rangle_x$	chi^2	τ_1 [ns] (x_1)	τ_2 [ns] (x_2)	τ_3 [ns] (x_3)	$\langle\tau\rangle_x$	chi^2
Cy5	1.042 (0.959)	0.599 (0.041)			**1.02**	1.2	1.538 (0.775)	0.717 (0.0767)	0.0892 (0.148)	**1.26**	1.1
Cy5-AZBC	0.207 (0.180)	0.712 (0.149)	1.196 (0.0426)	0.0458 (0.628)	**0.22**	1.2	1.555 (0.735)	0.0874 (0.183)	0.756 (0.0826)	**1.22**	1.2
Cy5-Trolox	0.168 (0.221)	0.584 (0.231)	1.0099 (0.547)		**0.73**	1.1	0.524 (0.107)	1.301 (0.721)	0.0927 (0.172)	**1.01**	1.1

Table S2. Fits results of lifetime measurements for Cy5, Cy5-AZB-C and Cy5-Trolox in buffer and in ethanol.

S8. *Absorption, excitation and emission spectra in buffer of Cy5 and Cy5-conjugates*

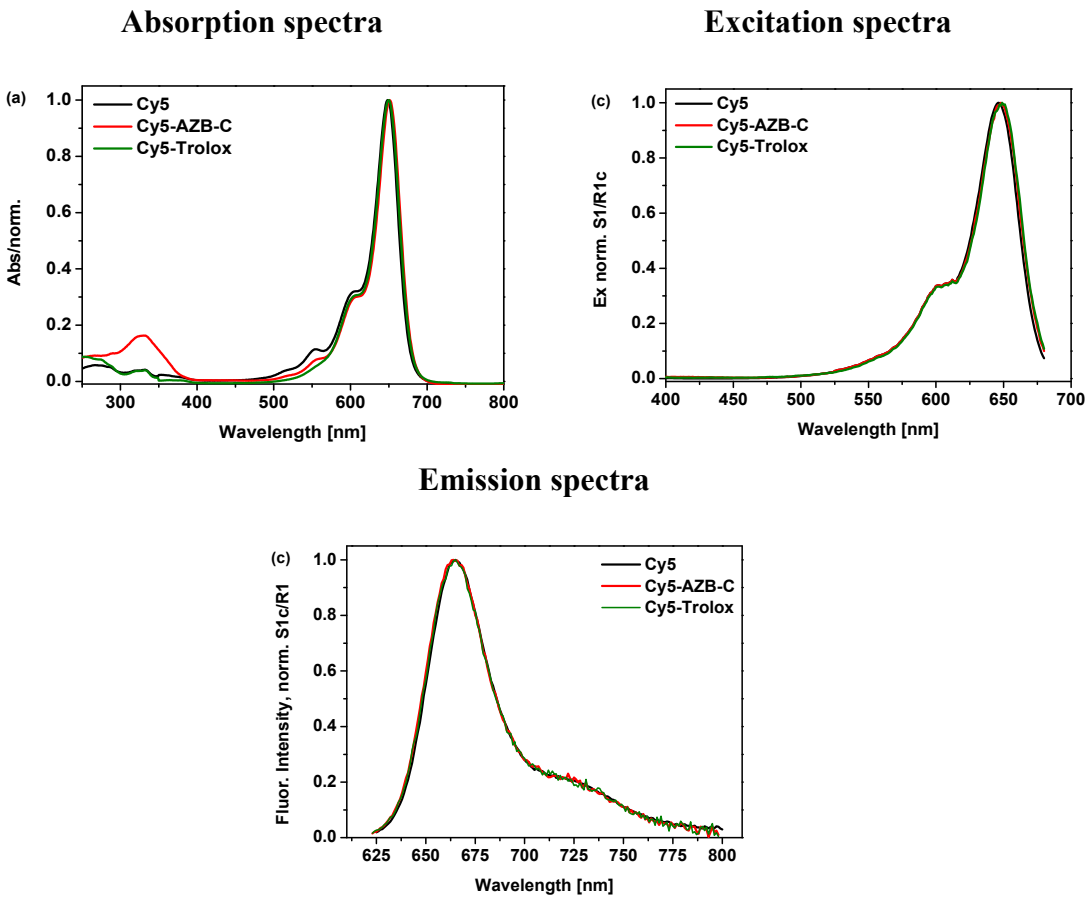

Figure S23. (a) Absorption spectra, (b) Excitation spectra, (c) Emission spectra, of Cy5 and Cy5-conjugates.

S9. *Results of global fits analysis for Cy5, Cy5-AZB-C and Cy5-Trolox in different conditions for the fast processes*

Probe	Solvent	Air / Argon	k_0 [10^9 s^{-1}]	σ [10^{-16} cm^2]	σ_{BISO} [10^{-16} cm^2]	k_{ISO} [10^6 s^{-1}]	k_{ISC} [10^6 s^{-1}]	k_T [10^6 s^{-1}]	C [mM]
Cy5	Buffer	Air	0.98 (fixed)	7.46 (fixed)	0.13	15.7	1.10	0.43	-
Cy5	Buffer	Argon	0.98 (fixed)	7.46 (fixed)	0.12	16.5	0.15	0.0064	-
Cy5	EtOH	Air	0.79 (fixed)	5.31 (fixed)	0.10	12.9	1.90	0.71	-
Cy5	EtOH	Argon	0.79 (fixed)	5.31 (fixed)	0.10	13.0	0.33	0.072	-
Cy5-AZB-C	Buffer	Air	4.54 (fixed)	7.46 (fixed)	0.089	33.6	1.10 (fixed)	0.43 (fixed)	14600
Cy5-AZB-C	Buffer	Argon	4.54 (fixed)	7.46 (fixed)	0.023	6.68	0.15 (fixed)	0.0064 (fixed)	8170
Cy5-AZB-C	EtOH	Air	0.82 (fixed)	5.31 (fixed)	0.079	10.7	1.90 (fixed)	0.71 (fixed)	0.60
Cy5-AZB-C	EtOH	Argon	0.82 (fixed)	5.31 (fixed)	0.052	7.50	0.33 (fixed)	0.072 (fixed)	0.93
Cy5-Trolox	Buffer	Air	1.37 (fixed)	7.46 (fixed)	0.14	27.8	1.10 (fixed)	0.43 (fixed)	9400
Cy5-Trolox	Buffer	Argon	1.37 (fixed)	7.46 (fixed)	0.10	16.2	0.15 (fixed)	0.0064 (fixed)	3460
Cy5-Trolox	EtOH	Air	0.99 (fixed)	5.31 (fixed)	0.10	17.3	1.90 (fixed)	0.71 (fixed)	0.98
Cy5-Trolox	EtOH	Argon	0.99 (fixed)	5.31 (fixed)	0.090	17.0	0.33 (fixed)	0.072 (fixed)	0.43

Table S3. Photophysical parameters of Cy5 and Cy5-conjugates under different conditions obtained from global fit analysis of FCS curves measured at different excitations powers using eq.(3.8-3.19).

In the first step, global fit analysis of FCS curves at different power irradiances for Cy5 free dye in different experimental conditions was done. For each condition was fixed k_0 and σ values. In the second step the photophysical parameters were determined for Cy5-cojugates. For Cy5-conjugates is possible to calculate the apparent concentration (C) by using $k'_T = k_T + k_{qT}[C]$ applied for triplet state where k_{qT} and k_T are fixed to Cy5 free dye values.

S10. *Diffusion times for Cy5 in different conditions and radical time for buffer/air*

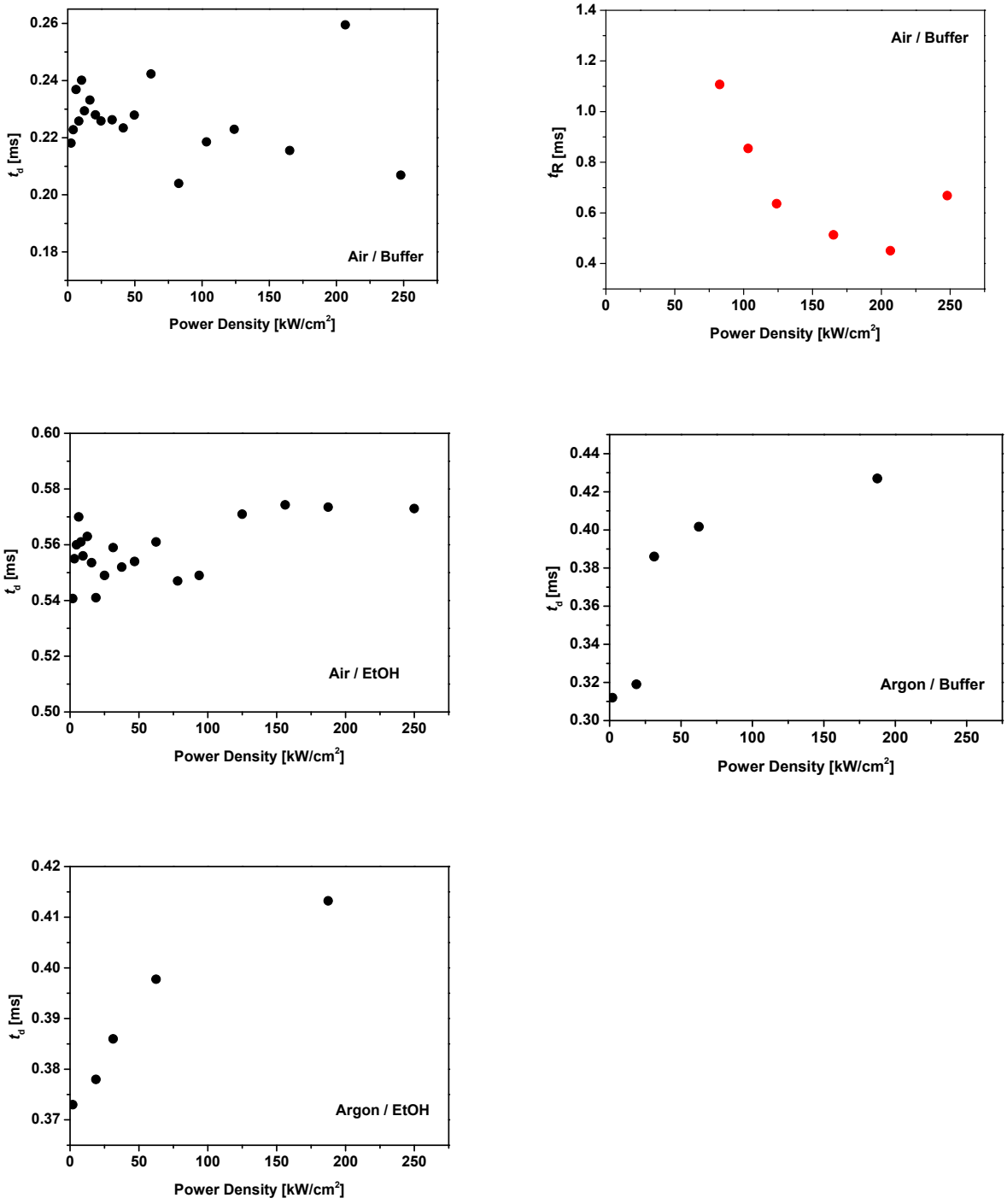

Figure S24. Diffusion times in different experimental conditions for Cy5. Radical term is present only in air/buffer environments. In the other experimental conditions no radical term is present due to the fact that ethanol is not able to stabilized charge and in argon no photo-oxidation occurs.

S11. *FCS curves of Cy5-conjugates compounds at different powers in air saturated buffer and EtOH*

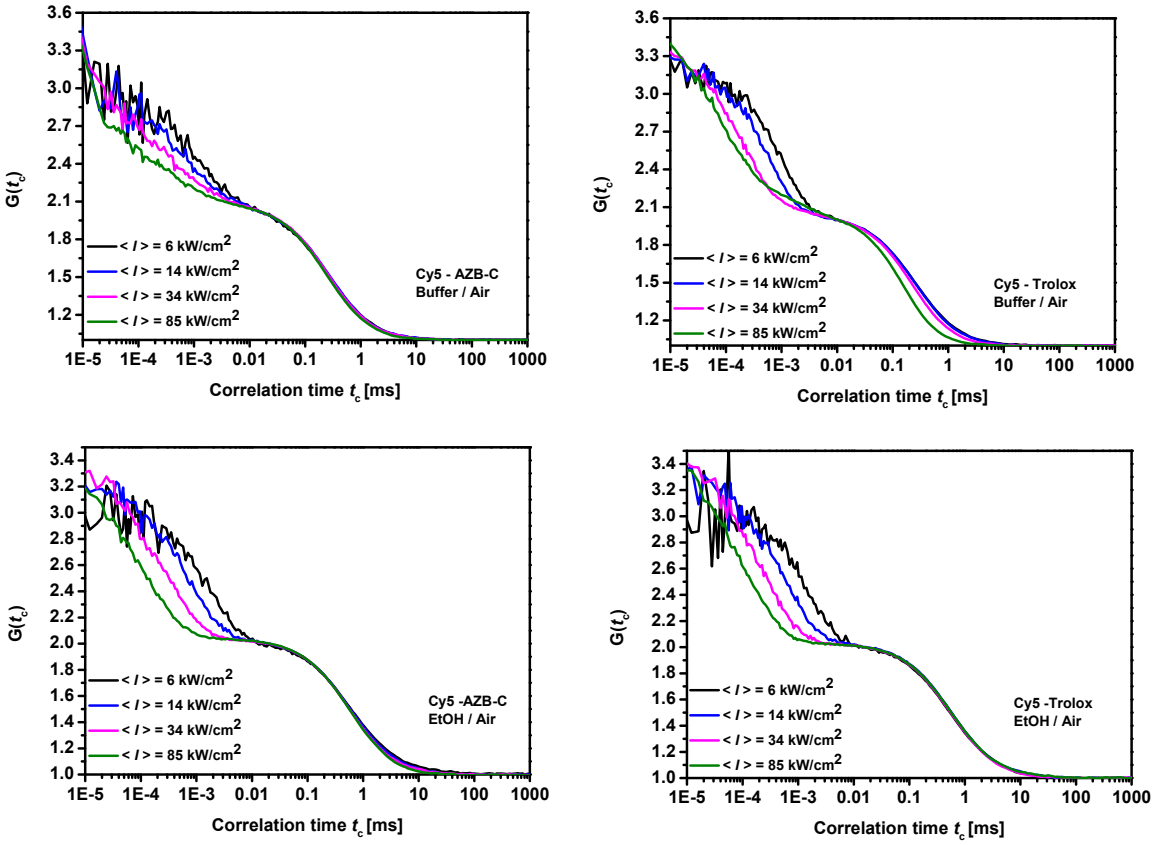

Figure S25. FCS in air saturated buffer and ethanol for Cy5-conjugates compounds. In buffer Cy5-Trolox does not have effect in the radical state, in ethanol $R^{\bullet+}$ is no present.

S12. *Oxygen effect*

	$[O_2]$ [μM]	k_{qISC} [10^9 $M^{-1}s^{-1}$]
Buffer	284	2.81
Ethanol	1940[182]	0.754

Table S4. Results of global fits analysis of buffer in air/argon and in ethanol air/argon of FCS curves with different excitation powers using eq.: $k'_{ISC} = k_{ISC} + k_{q_{ISC}} \cdot [O_2]$.

Chapter 4 Conclusions

In Chapter 2 it has been shown consistent results for long time diffusion coefficients of dextran molecules moving in solution and in a polyacrylamide gel matrix determined on different length scales by using multiparameter fluorescence image spectroscopy (MFIS), macroscopic transmission imaging (MTI) and nuclear magnetic resonance (NMR).

In addition, although the experimental results could be described by Ogston model, a more realistic flexible model of the gel matrix was applied to describe the data and to estimate the average pore size in the gel (nm scale).

Moreover, in MFIS, the x-y scanning of the gel and the long integration time per pixel (30 min) permit multiparameter fluorescence detection at defined locations for half an hour at each position. This optimal experimental condition used in the measurements allows identification of (i) a significant interaction between hydrogel and macromolecules and (ii) heterogeneities at different locations in the hydrogel.

Regarding the first point, the usage of uncharged dyes or charged dyes with the addition of a sufficiently high salt concentration is recommended for future investigations. In this way, the interaction between gel and matrix can be dramatically reduced or in the best scenario totally suppressed.

The heterogeneity inside a single hydrogel sample was probed on a length scale of 10μm in anisotropy experiments by comparing different pixels and hence different positions in the hydrogel. Therefore, combining experiments with BD-simulations enabled to achieve a better understanding of the factors determining the diffusion of molecules in the gel network.

In Chapter 3 the photostability of Cy5 in different solvents and environments has been tested by using quenchers as additives or covalently linked to Cy5 compounds to optimize the fluorophore photophysics. Indeed, in the ideal scenario, cycles between a first singlet excited state (S_1) and the ground state (S_0) resulting in a regular photon emission are generated. Unfortunately, the involvement of dark states in combination with electron and energy transfer may destroy the typically fluorescence emission. FCS and bleaching experiments show the best conditions required to achieve the maximum fluorescence signal obtainable by reducing the dark states amplitudes.

Using additives, AZB-C shows triplet quenching properties and reduces the radical state partially, whereas Trolox slightly influences only the triplet state. Photo-oxidation has been observed only in air saturated buffer where the production of radical cation state is stabilized by H_2O. In such case, AZB-C is needed to contrast the formation of radical state and especially Cy5-AZB-C is able to suppress the $R^{\bullet+}$ state totally. Indeed in buffer, the formal high local concentration of AZB-C in the conjugated compound dramatically decreases the amplitudes of dark states. Nevertheless, under buffer conditions, the additives are still the best way to improve to fluorescence signal of Cy5 due to the lower fluorescence quantum yield of the new compounds. Moreover, in argon solution where the triplet kinetic results at least 10 times slower, AZB-C and its conjugate show strong quenching effect on the triplet state. Indeed, oxygen is responsible for the photo-oxidation of the dye producing $R^{\bullet+}$ state and at the same time, is also good triplet quencher. Therefore, a good strategy provides the removal of oxygen in combination with the addition of triplet quencher like AZB-C.

In conclusion, these studies give recommendations regarding the best conditions for getting an ideal fluorophore in term of solvent, presence of oxygen and quenchers. Therefore, the model developed is able to predict and improve the fluorescence signal.

Acknowledgements

I want to express my gratitude to many people, without their support this Thesis would not have been possible. I gratefully acknowledge:

Prof. Dr. Claus Seidel who gave the opportunity to conduct my doctoral studies in his group. The enthusiasm that he puts in the scientific research it is unique and he transmits such quality to all his collaborators.

Dr. Denis Dörr for the great help and immense patience that he offered to me from the very first day that I came in this group. His big support was really much appreciated, for having been a strict (but not *evil*) teacher.

Dr. Ralf Kühnemuth for his continuous help during my PhD studies, ranging from support in using set-up, making measurements, writing manuscript, to give useful advice and productive scientific discussions.

Dr. Suren Felekyan for giving me a great help especially regarding gel data analysis, for improving all the time the imagine software that I used and for his helpful advice.

Prof. Dr. Thomas J. J. Müller for giving me the possibility to perform organic synthesis in his laboratories.

Dr. Bernhard Mayer for giving help and useful advice during organic synthesis and for his extremely positive mood making the lab work more efficient.

Dr. Stefanie Weidtkamp-Peters for her support during my PhD studies and for the nice conversations that we had in the train.

Olga for being the best colleague ever. For having done single molecule measurements (almost only) internally for us. I really want to thank her for her support especially in the hardest moments, for no scientific discussions during lunch, for being always positive and for having discovered a new friend.

Qijun for being amazing officemate, for producing for me always fresh orange juice and for sharing her positive mood.

Peter for keeping my “diet” schedule with junk food, for discussions about liquid pizza and for the special treatment reserved for his *ladies*.

Mykola for proofreading Chapter 3 and for being always available for any kind of help.

Aiswaria for proofreading Chapter 1 and for sharing her smiles to everybody.

Christian for his kindness in giving to me (for at least 20 times) information about Thesis submission.

Hayk for helping me with German documents and for his support.

Anne for proofreading Chapter 1 and for translating the summary in German in a short time.

The whole Seidel group always available in scientific support.

Thanks, to my Italian friend Mauro, for being in my same situation in the same time like in all our academic education. The mutual support has been fundamental.

I want to thanks my parents and my brother for their endless love and encouragement that they were able to send to me every day over 1000 km distance.

Thanks a lot to my life partner Paolo for being always patient and positive during my PhD studies. His support and his continuous belief in my capacities make him really special. I´m extremely lucky to have him in my life: Grazie di tutto Amore!

References

1. S. Weiss, *Science*, 1999, **283**, 1676-1683.
2. C. Joo, H. Balci, Y. Ishitsuka, C. Buranachai and T. Ha, *Annu. Rev. Biochem.*, 2008, **77**, 51-76.
3. C. Eggeling, J. R. Fries, L. Brand, R. Günther and C. A. M. Seidel, *Proc. Natl. Acad. Sci. USA*, 1998, **95**, 1556-1561.
4. J. R. Fries, L. Brand, C. Eggeling, M. Köllner and C. A. M. Seidel, *J. Phys. Chem. A*, 1998, **102**, 6601-6613.
5. R. Kühnemuth and C. A. M. Seidel, *Single Mol.*, 2001, **2**, 251-254.
6. F. Chen, P. Tillberg and E. Boyden, *Science*, 2015, **347**, 543-548.
7. D. Wöll, *RSC Adv*, 2014, **4**, 2447-2465.
8. S. T. Balke, A. E. Hamielec, B. P. LeClair and S. L. Pearce, *Ind. Eng. Chem. Prod. Res. Dev.*, 1969, **8**, 54-57.
9. V. E. Barsky, A. M. Kolchinsky, Y. P. Lysov and A. D. Mirzabekov, *Mol. Biol.*, 2002, **36**, 437-455.
10. T.-O. Peulen and K. J. Wilkinson, *Environ. Sci. Technol.*, 2011, **45**, 3367-3373.
11. S. Brahim, D. Narinesingh and A. Guiseppi-Elie, *Biomacromolecules*, 2003, **4**, 1224-1231.
12. N. Murthy, Y. X. Thng, S. Schuck, M. C. Xu and J. M. J. Fréchet, *J. Am. Chem. Soc.*, 2002, **124**, 12398-12399.
13. P. Gupta, K. Vermani and S. Garg, *Drug Discov. Today*, 2002, **7**, 569-579.
14. R. Morita, R. Honda and Y. Takahashi, *J. Controlled Release*, 2000, **68**, 115-120.
15. S. Sershen and J. West, *Adv. Drug Delivery Rev.*, 2002, **54**, 1225-1235.
16. D. T. Eddington and D. J. Beebe, *Adv. Drug Delivery Rev.*, 2004, **56**, 199-210.
17. O. Wichterle and D. Lim, *Nature*, 1960, **185**, 117-118.
18. H.-W. Kang, Y. Tabata and Y. Ikada, *Biomaterials*, 1999, **20**, 1339-1344.
19. A. S. Hoffman, *Adv. Drug Delivery Rev.*, 2002, **54**, 3-12.
20. A. Z. Abidin, T. Puspasari and W. A. Nugroho, *Procedia Chem.*, 2012, **4**, 11-16.
21. R. Zolfaghari, A. A. Katbab, J. Nabavizadeh, R. Y. Tabasi and M. H. Nejad, *J. Appl. Polym. Sci.*, 2006, **100**, 2096-2103.
22. M. Orrit, *Photochem. Photobiol. Sci.*, 2010, **9**, 637-642.
23. M. Levitus and S. Ranjit, *Q. Rev. Biophys.*, 2011, **44**, 123-151.
24. T. Ha and P. Tinnefeld, *Annu.Rev.Phys.Chem.*, 2012, **63**, 595-617.
25. C. Eggeling, J. Widengren, L. Brand, J. Schaffer, S. Felekyan and C. A. M. Seidel, *J. Phys. Chem. A*, 2006, **110**, 2979-2995.
26. J. Vogelsang, R. Kasper, C. Steinhauer, B. Person, M. Heilemann, M. Sauer and P. Tinnefeld, *Angew. Chem. Int. Ed.*, 2008, **47**, 5465-5469.
27. T. Cordes, A. Maiser, C. Steinhauer, L. Schermelleh and P. Tinnefeld, *Phys. Chem. Chem. Phys.*, 2011, **13**, 6699-6709.
28. Q. Zheng, S. Jockusch, Z. Zhou and S. C. Blanchard, *Photochem. Photobiol.*, 2014, **90**, 448-454.
29. R. B. Altman, D. S. Terry, Z. Zhou, Q. Zheng, P. Geggier, R. A. Kolster, Y. Zhao, J. A. Javitch, J. D. Warren and S. C. Blanchard, *Nat. Meth.*, 2012, **9**, 68-71.

30. Q. Zheng, S. Jockusch, Z. Zhou, R. B. Altman, J. D. Warren, N. J. Turro and S. C. Blanchard, *J. Phys. Chem. Lett.*, 2012, **3**, 2200-2203.
31. Q. Zheng, M. F. Juette, S. Jockusch, M. R. Wasserman, Z. Zhou, R. B. Altman and S. C. Blanchard, *Chem. Soc. Rev.*, 2014, **43**, 1044-1056.
32. J. H. M. van der Velde, J. Oelerich, J. Huang, J. H. Smit, A. Aminian Jazi, S. Galiani, K. Kolmakov, G. Guoridis, C. Eggeling, A. Herrmann, G. Roelfes and T. Cordes, *Nat. Commun.*, 2016, **7**.
33. J. Widengren, V. Kudryavtsev, M. Antonik, S. Berger, M. Gerken and C. A. M. Seidel, *Anal. Chem.*, 2006, **78**, 2039-2050.
34. S. Weidtkamp-Peters, S. Felekyan, A. Bleckmann, R. Simon, W. Becker, R. Kühnemuth and C. A. M. Seidel, *Photochem. Photobiol. Sci.*, 2009, **8**, 470-480.
35. J. Widengren and P. Schwille, *J. Phys. Chem. A*, 2000, **104**, 6416-6428.
36. K. Bacia, S. A. Kim and P. Schwille, *Nat. Meth.*, 2006, **3**, 83-89.
37. P. Kask, K. Palo, D. Ullmann and K. Gall, *Proceedings of the National Academy of Sciences*, 1999, **96**, 13756-13761.
38. D. Magde, E. Elson and W. W. Webb, *Phys. Rev. Lett.*, 1972, **29**, 705-708.
39. O. Krichevsky and G. Bonnet, *Rep. Prog. Phys.*, 2002, **65**, 251.
40. E. Haustein and P. Schwille, *Annu. Rev. Biophys. Biomol. Struct.*, 2007, **36**, 151-169.
41. A. Vagias, R. Raccis, K. Koynov, U. Jonas, H.-J. Butt, G. Fytas, P. Košovan, O. Lenz and C. Holm, *Phys. Rev. Lett.*, 2013, **111**, 088301.
42. L. Haggerty, J. H. Sugarman and R. K. Prud'homme, *Polymer*, 1988, **29**, 1058-1063.
43. D. L. Holmes and N. C. Stellwagen, *Electrophoresis*, 1991, **12**, 253-263.
44. M. Kremer, E. Pothmann, T. Rössler, J. Baker, A. Yee, H. Blanch and J. M. Prausnitz, *Macromolecules*, 1994, **27**, 2965-2973.
45. J. Tong and J. L. Anderson, *Biophys. J.*, 1996, **70**, 1505-1513.
46. S. M. Russell and G. Carta, *Ind. Eng. Chem. Res.*, 2005, **44**, 8213-8217.
47. A. Stellwagen and N. C. Stellwagen, *Biopolymers*, 1990, **30**, 309-324.
48. D. L. Holmes and N. C. Stellwagen, *Electrophoresis*, 1991, **12**, 612-619.
49. J. S. Fawcett and C. J. O. R. Morris, *Sep. Sci.*, 1966, **1**, 9-26.
50. M. P. Tombs, *Anal. Biochem.*, 1965, **13**, 121-132.
51. N. C. Stellwagen, *Biochemistry*, 1983, **22**, 6186-6193.
52. R. Rüchel and M. D. Brager, *Anal. Biochem.*, 1975, **68**, 415-428.
53. L. M. Lira, K. A. Martins and S. I. C. d. Torresi, *Eur. Polym. J.*, 2009, **45**, 1232-1238.
54. Z. Blank and A. C. Reimschuessel, *J. Mater. Sci.*, 1974, **9**, 1815-1822.
55. D. Pfiffi, dissertation, Heinrich-Heine-Universität: Düsseldorf, 2010.
56. J. Widengren, A. Chmyrov, C. Eggeling, P.-Å. Löfdahl and C. A. M. Seidel, *J. Phys. Chem. A*, 2007, **111**, 429-440.
57. A. Meller, *J. Phys. Condens. Matter*, 2003, **15**, R581.
58. A. Milchev, *J. Phys. Condens. Matter*, 2011, **23**, 103101.
59. R. Metzler and J. Klafter, *Phys. Rep.*, 2000, **339**, 1-77.
60. F. Höfling and T. Franosch, *Rep. Prog. Phys.*, 2013, **76**, 046602.
61. K. Mecke, *Acta Phys. Pol. B*, 1997, **28**, 1747-1782.
62. A. G. Ogston, B. N. Preston and J. D. Wells, *Proc. R. Soc. London Ser. A-Math. Phys. Eng. Sci.*, 1973, **333**, 297-316.
63. S. Schneider and P. Linse, *Macromolecules*, 2004, **37**, 3850-3856.
64. S. Edgecombe, S. Schneider and P. Linse, *Macromolecules*, 2004, **37**, 10089-10100.

65. S. Schneider and P. Linse, *J. Phys. Chem. B*, 2003, **107**, 8030-8040.
66. S. Schneider and P. Linse, *Eur. Phys. J. E*, 2002, **8**, 457-460.
67. B. A. F. Mann, K. Kremer, O. Lenz and C. Holm, *Macromol. Theory Simul.*, 2011, **20**, 721-734.
68. B. A. Mann, C. Holm and K. Kremer, *J. Chem. Phys*, 2005, **122**, 154903.
69. B. A. Mann, R. Everaers, C. Holm and K. Kremer, *EPL*, 2004, **67**, 786.
70. P. A. Netz and T. Dorfmüller, *J. Chem. Phys*, 1997, **107**, 9221-9233.
71. H. Pei, S. Allison, B. M. H. Haynes and D. Augustin, *J. Phys. Chem. B*, 2009, **113**, 2564-2571.
72. L. Johansson and J. E. Löfroth, *J. Chem. Phys*, 1993, **98**, 7471-7479.
73. P. Licinio and A. V. Teixeira, *Phys. Rev. E*, 1997, **56**, 631-634.
74. H. Zhou and S. B. Chen, *Phys. Rev. E*, 2009, **79**, 021801.
75. K. Kremer, *Comput. Mater. Sci.*, 1998, **10**, 168-174.
76. R. Messing, N. Frickel, L. Belkoura, R. Strey, H. Rahn, S. Odenbach and A. M. Schmidt, *Macromolecules*, 2011, **44**, 2990-2999.
77. D. A. Carr and N. A. Peppas, *Macromol. Biosci.*, 2009, **9**, 497-505.
78. F. Ganji, S. Vasheghani-Farahani and E. Vasheghani-Farahani, *Iran Polym. J.*, 2010, **19**, 375-398.
79. H. Durchschlag and P. Zipper, in *Ultracentrifugation*, ed. M. D. Lechner, Steinkopff, 1994, vol. 94, ch. 3, pp. 20-39.
80. J. Jovanovic and B. Adnadjevic, *Polym. Bull.*, 2007, **58**, 243-252.
81. M. K. Krušić, M. Ilić and J. Filipović, *Polym. Bull.*, 2009, **63**, 197-211.
82. A. M. Lowman and N. A. Peppas, *Macromolecules*, 1997, **30**, 4959-4965.
83. A. Thakur, *Chem. Biochem. Eng. Q.*, 2011, **25**, 181.
84. Y. Stahl, S. Grabowski, A. Bleckmann, R. Kühnemuth, S. Weidtkamp-Peters, K. G. Pinto, G. K. Kirschner, J. B. Schmid, R. H. Wink, A. Hülsewede, S. Felekyan, C. A. M. Seidel and R. Simon, *Curr. Biol.*, 2013, **23**, 362-371.
85. D. Wagner, M. Börgardts, C. Grünzweig, E. Lehmann, T. J. J. Müller, S. U. Egelhaaf and H. E. Hermes, *Rev. Sci. Instrum.*, 2015, **86**, 093706.
86. M. Holz, S. R. Heil and A. Sacco, *Phys. Chem. Chem. Phys.*, 2000, **2**, 4740-4742.
87. A. L. Van Geet, *Anal. Chem.*, 1970, **42**, 679-680.
88. D. H. Wu, A. D. Chen and C. S. Johnson, *J. Magn. Reson., Ser A*, 1995, **115**, 260-264.
89. G. Wider, V. Dötsch and K. Wüthrich, *J. Magn. Reson., Ser A*, 1994, **108**, 255-258.
90. V. Sklenar, M. Piotto, R. Leppik and V. Saudek, *J. Magn. Reson., Ser A*, 1993, **102**, 241-245.
91. M. Piotto, V. Saudek and V. Sklenář, *J. Biomol. NMR*, 1992, **2**, 661-665.
92. P. Sengupta, K. Garai, J. Balaji, N. Periasamy and S. Maiti, *Biophys. J.*, 2003, **84**, 1977-1984.
93. P. O. Gendron, F. Avaltroni and K. J. Wilkinson, *J. Fluoresc.*, 2008, **18**, 1093-1101.
94. J. Enderlein, I. Gregor, D. Patra, T. Dertinger and U. B. Kaupp, *ChemPhysChem*, 2005, **6**, 2324-2336.
95. J. Enderlein, I. Gregor, D. Patra and J. Fitter, *Curr. Pharm. Biotechnol.*, 2004, **5**, 155-161.
96. M. Koshioka, K. Sasaki and H. Masuhara, *Appl. Spectrosc.*, 1995, **49**, 224-228.
97. N. B. Vicente, J. E. Diaz Zamboni, J. F. Adur, E. V. Paravani and V. H. Casco, *J. Phys. Conf. Ser.*, 2007, **90**, 012068.

98. L. Hodgson, P. Nalbant, F. Shen and K. Hahn, *Methods Enzymol.*, 2006, **406**, 140-156.
99. D. Wagner, J. Burbach, C. Grünzweig, E. Lehmann, S. U. Egelhaaf and H. E. Hermes, unpublished work.
100. W. S. Price, *Concepts Magn. Reson.*, 1997, **9**, 299-336.
101. C. S. Johnson Jr., *Prog. Nucl. Magn. Reson. Spectrosc.*, 1999, **34**, 203-256.
102. F. J. Millero, R. Dexter and E. Hoff, *J. Chem. Eng. Data*, 1971, **16**, 85-87.
103. P. G. Bolhuis, A. A. Louis, J. P. Hansen and E. J. Meijer, *J. Chem. Phys*, 2001, **114**, 4296-4311.
104. A. A. Louis, P. G. Bolhuis, E. J. Meijer and J. P. Hansen, *J. Chem. Phys*, 2002, **117**, 1893-1907.
105. J. Dzubiella, A. Jusufi, C. N. Likos, C. von Ferber, H. Löwen, J. Stellbrink, J. Allgaier, D. Richter, A. B. Schofield, P. A. Smith, W. C. K. Poon and P. N. Pusey, *Phys. Rev. E*, 2001, **64**, 010401.
106. M. P. Allen and D. J. Tildesley, *Computer Simulation of Liquids (Oxford Science Publications)*, Oxford University Press, 1989.
107. B. J. Alder, D. M. Gass and T. E. Wainwright, *J. Chem. Phys*, 1970, **53**, 3813-3826.
108. M. Y. Kizilay and O. Okay, *Macromolecules*, 2003, **36**, 6856-6862.
109. A. M. Hecht, R. Duplessix and E. Geissler, *Macromolecules*, 1985, **18**, 2167-2173.
110. P. Debye and E. Hückel, *Phys. Z.*, 1923, **24**, 185-206.
111. F. Hofmeister, *Arch. Exp. Pathol. Pharmakol.(Leipzig)*, 1888, **24**, 247-260.
112. K. D. Collins and M. W. Washabaugh, *Q. Rev. Biophys.*, 1985, **18**, 323-422.
113. C. Eggeling, dissertation, Georg-August-Universität zu Göttingen, 1999.
114. J. Stejskal and J. Horská, *Makromol. Chem.*, 1982, **183**, 2527-2535.
115. D. Toptygin, *J. Fluoresc.*, 2003, **13**, 201-219.
116. Z. Zhang, E. Nadezhina and K. J. Wilkinson, *Antimicrob. Agents Chemother.*, 2011, **55**, 1075-1081.
117. A. W. Moore Jr. and J. W. Jorgenson, *Anal. Chem.*, 1993, **65**, 3550-3560.
118. Z. Petrášek and P. Schwille, *Biophys. J.*, 2008, **94**, 1437-1448.
119. E. P. Petrov, T. Ohrt, R. G. Winkler and P. Schwille, *Phys. Rev. Lett.*, 2006, **97**.
120. J. Crank, *The Mathematics of Diffusion*, Clarendon Press, Oxford, 2nd edn., 1975.
121. T. Kihara, J. Ito and J. Miyake, *PLoS One*, 2013, **8**, e82382.
122. S. Lehmann, S. Seiffert and W. Richtering, *J. Am. Chem. Soc.*, 2012, **134**, 15963-15969.
123. B. Amsden, *Macromolecules*, 1998, **31**, 8382-8395.
124. L. Masaro and X. X. Zhu, *Prog. Polym. Sci.*, 1999, **24**, 731-775.
125. B. A. Westrin, A. Axelsson and G. Zacchi, *J. Controlled Release*, 1994, **30**, 189-199.
126. D. Magde, R. Wong and P. G. Seybold, *Photochem. Photobiol.*, 2002, **75**, 327-334.
127. X.-F. Zhang, Y. Zhang and L. Liu, *J. Lumin.*, 2014, **145**, 448-453.
128. N. L. Thompson, in *Topics in Fluorescence Spectroscopy*, ed. J. R. Lakowicz, Plenum Press, New York, 1991, vol. 1, pp. 337-378.
129. *Release on the Refractive Index of Ordinary Water Substance as a Function of Wavelength, Temperature and Pressure*, The International Association for the Properties of Water and Steam, Erlangen, Germany, 1997.
130. E. Banachowicz, A. Patkowski, G. Meier, K. Klamecka and J. Gapinski, *Langmuir*, 2014, **30**, 8945-8955.
131. M. A. Masuelli, *J. Polym. Biopolym. Phys. Chem.*, 2013, **1**, 13-21.
132. C. Eggeling, A. Volkmer and C. A. M. Seidel, *ChemPhysChem*, 2005, **6**, 791-804.

133. J. Widengren and R. Rigler, *Bioimaging*, 1996, **4**, 149-157.
134. P. Chen, J. Li, Z. Qian, D. Zheng, T. Okasaki and M. Hayami, *Dyes Pigm.*, 1998, **37**, 213-222.
135. G. W. Byers, S. Gross and P. M. Henrichs, *Photochem. Photobiol.*, 1976, **23**, 37-43.
136. J. Vogelsang, C. Steinhauer, C. Forthmann, I. H. Stein, B. Person-Skegro, T. Cordes and P. Tinnefeld, *ChemPhysChem*, 2010, **11**, 2475-2490.
137. T. Cordes, J. Vogelsang and P. Tinnefeld, *J. Am. Chem. Soc.*, 2009, **131**, 5018-5019.
138. I. Rasnik, S. A. McKinney and T. Ha, *Nat. Meth.*, 2006, **3**, 891-893.
139. I. H. Stein, S. Capone, J. H. Smit, F. Baumann, T. Cordes and P. Tinnefeld, *ChemPhysChem*, 2012, **13**, 931-937.
140. J. H. M. van der Velde, E. Ploetz, M. Hiermaier, J. Oelerich, J. W. de Vries, G. Roelfes and T. Cordes, *ChemPhysChem*, 2013, **14**, 4084-4093.
141. J. H. M. van der Velde, J. Oelerich, J. Huang, J. H. Smit, M. Hiermaier, E. Ploetz, A. Herrmann, G. Roelfes and T. Cordes, *J. Phys. Chem. Lett.*, 2014, **5**, 3792-3798.
142. F. D. Jochum and P. Theato, *Polymer*, 2009, **50**, 3079-3085.
143. P. Schattling, F. D. Jochum and P. Theato, *Chem.Commun.*, 2011, **47**, 8859-8861.
144. L. Wang, J. Fan, X. Qiao, X. Peng, B. Dai, B. Wang, S. Sun, L. Zhang and Y. Zhang, *J. Photochem. Photobiol., A*, 2010, **210**, 168-172.
145. D. Oushiki, H. Kojima, T. Terai, M. Arita, K. Hanaoka, Y. Urano and T. Nagano, *J. Am. Chem. Soc.*, 2010, **132**, 2795-2801.
146. J. R. Lakowicz, *Principles of Fluorescence Spectroscopy*, Kluwer Academic/Plenum Publishers, New York, 1999.
147. J. Arden-Jacob, Universität-Gesamthochschule, 1992.
148. D. Rehm and A. Weller, *Isr. J. Chem.*, 1970, **8**, 259-271.
149. D. Rehm and A. Weller, *Z. Phys. Chem.*, 1970, **69**, 183-200.
150. I. Baraldi, A. Carnevali, F. Momicchioli and G. Ponterini, *Spectrochim. Acta, Part A*, 1993, **49**, 471-495.
151. W. West, S. Pearce and F. Grum, *J. Phys. Chem.*, 1967, **71**, 1316-1326.
152. D. N. Dempster, T. Morrow, R. Rankin and G. F. Thompson, *J. Chem. Soc., Faraday Trans. 2*, 1972, **68**, 1479-1496.
153. R. E. Di Paolo, L. B. Scaffardi, R. Duchowicz and G. M. Bilmes, *J. Phys. Chem.*, 1995, **99**, 13796-13799.
154. R. Duchowicz, L. Scaffardi and J. O. Tocho, *Chem. Phys. Lett.*, 1990, **170**, 497-501.
155. V. Sundstroem and T. Gillbro, *J. Phys. Chem.*, 1982, **86**, 1788-1794.
156. D. H. Waldeck and G. R. Fleming, *J. Phys. Chem.*, 1981, **85**, 2614-2617.
157. H. J. Gruber, C. D. Hahn, G. Kada, C. K. Riener, G. S. Harms, W. Ahrer, T. G. Dax and H.-G. Knaus, *Bioconjug. Chem.*, 2000, **11**, 696-704.
158. B. J. Harvey, C. Perez and M. Levitus, *Photochem. Photobiol. Sci.*, 2009, **8**, 1105-1110.
159. R. Dave, D. S. Terry, J. B. Munro and S. C. Blanchard, *Biophys. J.*, 2009, **96**, 2371-2381.
160. C. Eggeling, J. Widengren, R. Rigler and C. A. M. Seidel, *Anal. Chem.*, 1998, **70**, 2651-2659.
161. A. Chmyrov, T. Sandén and J. Widengren, *J. Phys. Chem. B*, 2010, **114**, 11282-11291.
162. I. Gregor, D. Patra and J. Enderlein, *ChemPhysChem*, 2005, **6**, 164-170.
163. C. Eggeling, J. Widengren, R. Rigler and C. A. M. Seidel, in *Applied Fluorescence in Chemistry, Biology and Medicine*, Springer Berlin Heidelberg, 1999, ch. 10, pp. 193-240.
164. E. v. Lippert, *Z. Elektrochem.*, 1957, **61**, 962-975.

165. N. Mataga, Y. Kaifu and M. Koizumi, *Bull. Chem. Soc. Jpn.*, 1956, **29**, 465-470.
166. S. A. Soper, H. L. Nutter, R. A. Keller, L. M. Davis and E. B. Shera, *Photochem. Photobiol.*, 1993, **57**, 972-977.
167. S. P. Velsko, D. H. Waldeck and G. R. Fleming, *J. Chem. Phys*, 1983, **78**, 249-258.
168. P. F. Aramendia, R. M. Negri and E. S. Roman, *J. Phys. Chem.*, 1994, **98**, 3165-3173.
169. S. P. Velsko and G. R. Fleming, *Chem. Phys.*, 1982, **65**, 59-70.
170. G. Ponterini and F. Momicchioli, *Chem. Phys.*, 1991, **151**, 111-126.
171. J. Rodríguez, D. Scherlis, D. Estrin, P. F. Aramendía and R. M. Negri, *J. Phys. Chem. A*, 1997, **101**, 6998-7006.
172. V. Ramamurthy, N. J. Turro and J. C. Scaiano, *Modern Molecular Photochemistry of Organic Molecules*, University Science Publishers: New York, 2010.
173. P. M. Wood, *FEBS Lett.*, 1974, **44**, 22-24.
174. Z. Huang, D. Ji, A. Xia, F. Koberling, M. Patting and R. Erdmann, *J. Am. Chem. Soc.*, 2005, **127**, 8064-8066.
175. C. A. M. Seidel, A. Schulz and M. H. M. Sauer, *J. Phys. Chem.*, 1996, **100**, 5541-5553.
176. M. Antonik, S. Felekyan, A. Gaiduk and C. A. M. Seidel, *J. Phys. Chem. B*, 2006, **110**, 6970-6978.
177. S. Kalinin, T. Peulen, S. Sindbert, P. J. Rothwell, S. Berger, T. Restle, R. S. Goody, H. Gohlke and C. A. M. Seidel, *Nat. Meth.*, 2012, **9**, 1218-1225.
178. R. A. Marcus, *Annu.Rev.Phys.Chem.*, 1964, **15**, 155-196.
179. L. Eberson, in *Adv. Phys. Org. Chem.*, eds. V. Gold and D. Bethell, Academic Press, 1982, vol. Volume 18, pp. 79-185.
180. G. J. Kavarnos and N. J. Turro, *Chem. Rev.*, 1986, **86**, 401-449.
181. R. Rigler, Ü. Mets, J. Widengren and P. Kask, *Eur. Biophys. J.*, 1993, **22**, 169-175.
182. C. Franco and J. Olmsted, *Talanta*, 1990, **37**, 905-909.

Hiermit erkläre ich, dass ich die Promotion mit dem Thema

“Analysis of molecular diffusion and photochemistry by quantitative fluorescence correlation spectroscopy”

am Institut für Physikalische Chemie II der Heinrich-Heine-Universität Düsseldorf unter der Leitung von Prof. Dr. Claus A.M. Seidel eigenständig und ohne unerlaubte Hilfe angefertigt und in der vorgelegten oder in ähnlicher Form noch bei keiner anderen Institution eingereicht habe.

Es existieren keine vorherigen Promotionsversuche.

Düsseldorf, den 06.04.2017

Deborah Sandrin